

**TIME DOMAIN ANALYSIS OF THE IMPACT OF  
GEOMAGNETICALLY INDUCED CURRENT ON POWER  
SYSTEM**

A Dissertation  
Presented to  
The Academic Faculty

by

Jiahao Xie

In Partial Fulfillment  
of the Requirements for the Degree  
Doctor of Philosophy in the  
School of Electrical and Computer Engineering

Georgia Institute of Technology  
May 2020

**COPYRIGHT © 2020 BY JIAHAO XIE**

**TIME DOMAIN ANALYSIS OF THE IMPACT OF  
GEOMAGNETICALLY INDUCED CURRENT ON POWER  
SYSTEM**

Approved by:

Dr. A. P. Sakis Meliopoulos, Advisor  
School of Electrical and Computer  
Engineering  
*Georgia Institute of Technology*

Dr. Lukas Graber  
School of Electrical and Computer  
Engineering  
*Georgia Institute of Technology*

Dr. Santiago Carlos Grijalva  
School of Electrical and Computer  
Engineering  
*Georgia Institute of Technology*

Dr. Sung Ha Kang  
School of Mathematics  
*Georgia Institute of Technology*

Dr. Daniel Molzahn  
School of Electrical and Computer  
Engineering  
*Georgia Institute of Technology*

Date Approved: [April 17, 2020]

To my parents, Qiangzhen and Ping,

with all my love.

## ACKNOWLEDGEMENTS

My journey to pursue a Ph.D. degree at Georgia Tech is an amazing experience. During the past five years, I met friends from the world and received enormous support from them. I would like to express my appreciation to all of my friends.

First, I would like to express my sincere gratitude to my advisor, Dr. A. P. Sakis Meliopoulos. His motivation and support enable me to start my research and finish my study. I have learned how to conduct research work in the power system area from the countless discussion with Dr. Meliopoulos. His insightful comments help me to spot problems, solve problems, and present the solution. Dr. Meliopoulos is a role model of enthusiasm for the work. I always hope that I could be as enthusiastic, and energetic as Dr. Meliopoulos.

I also would like to give my thanks to Dr. George Cokkinides. He provides tremendous help with software development related to power system studies. A large portion of my research work starts with his well-organized software library and his advice on coding is always perfectly understandable.

I also owe special thanks to Dr. Santiago Carlos Grijalva, Dr. Daniel Molzahn, Dr. Lukas Graber, and Dr. Sung Ha Kang for serving as my dissertation committee. They offer great comments on my dissertation. I would like to express my gratitude to Dr. Maryam Saeedifard, who served as my Ph.D. proposal committee and provided valuable suggestions on my research work.

My sincere thanks also go to my fellow labmates in the Power Systems Control and Automation Laboratory. During my early stage as a Ph.D. student, the discussion with Dr. Liangyi Sun, Dr. Yu Liu and Dr. Bai Cui shed light on the nature of power systems for me. During the completion of research projects, I got a huge amount of advice from Dr. Chiyang Zhong, Boqi Xie, Kaiyu Liu, Maad AlOwaifeer and Gad Monga Ilunga. I would also like to thank Dr. Yuan Kong, Dr. Zhengkai Wu, Dr. Abdullah Alamri, Orestis Vasios, Emeka Obikwelu. Besides, I also would like to thank other friends in Georgia Tech including Hang Shao, Jia Wei, Chunmeng Xu, Jingfan Sun and Zhaocheng Liu for their friendship and support since the bond of people is the true power.

Finally, I would like to thank my parents, Qiangzhen Xie and Ping Li, for their selfless love. I know I always have my family with me when times are rough, and I could not complete this long journey without their emotional support.

# TABLE OF CONTENTS

<b>ACKNOWLEDGEMENTS</b>	<b>iv</b>
<b>LIST OF TABLES</b>	<b>viii</b>
<b>LIST OF FIGURES</b>	<b>ix</b>
<b>SUMMARY</b>	<b>xii</b>
<b>CHAPTER 1. Introduction</b>	<b>1</b>
<b>1.1 Problem Statement</b>	<b>1</b>
<b>1.2 Research Objectives</b>	<b>2</b>
<b>1.3 Thesis Outline</b>	<b>3</b>
<b>CHAPTER 2. Literature Review</b>	<b>6</b>
<b>2.1 Geomagnetically Induced Current</b>	<b>6</b>
<b>2.2 Frequency-Dependent Transmission Line Models</b>	<b>8</b>
<b>2.3 Transformer Models</b>	<b>11</b>
<b>2.4 Instrumentation Channel Error during GMD</b>	<b>12</b>
<b>2.5 Protective Relays Performance during GMD</b>	<b>13</b>
<b>2.6 Modeling Methods for the Impact of GMD</b>	<b>13</b>
<b>2.7 Summary</b>	<b>15</b>
<b>CHAPTER 3. Research Overview</b>	<b>16</b>
<b>3.1 Method Overview</b>	<b>16</b>
<b>3.2 Summary</b>	<b>18</b>
<b>CHAPTER 4. Low-Frequency Broadband Transmission Line Model</b>	<b>19</b>
<b>4.1 Model Derivation</b>	<b>19</b>
4.1.1 Motivation	19
4.1.2 Multi-layer Conductor Model	21
4.1.3 Multi-layer Soil Model	24
<b>4.2 Model Validation</b>	<b>26</b>
4.2.1 Validation of Self-impedance	27
4.2.2 Validation of Mutual Impedance	31
<b>4.3 Transmission Line Model with Geoelectric Field</b>	<b>32</b>
4.3.1 Geoelectric Field Modelling	32
4.3.2 Transmission Line Modelling	33
<b>4.4 Time Domain Simulation Results</b>	<b>35</b>
<b>4.5 Conclusions</b>	<b>38</b>
<b>CHAPTER 5. Transformer Models with Detailed Magnetic Circuits</b>	<b>39</b>

<b>5.1</b>	<b>Time Domain Modeling of Transformers</b>	<b>41</b>
5.1.1	Parameter Calculation	46
<b>5.2</b>	<b>Numerical Results</b>	<b>47</b>
5.2.1	Test Case Description	47
5.2.2	Performance during Normal Operation	48
5.2.3	Performance during GMD events	51
<b>5.3</b>	<b>A Mitigation Method</b>	<b>58</b>
<b>5.4</b>	<b>Conclusions</b>	<b>60</b>
<b>CHAPTER 6.</b>	<b>GIC Transients in Power Grids</b>	<b>61</b>
<b>6.1</b>	<b>Directional Sensitivity in GIC Transients</b>	<b>61</b>
6.1.1	Test Case Overview	62
6.1.2	Numerical Results	65
<b>6.2</b>	<b>GMD Field Estimation</b>	<b>72</b>
6.2.1	Estimation Model Formulation	73
6.2.2	Numerical Results	75
<b>6.3</b>	<b>Conclusions</b>	<b>82</b>
<b>CHAPTER 7.</b>	<b>Harmonic Analysis during GMD</b>	<b>83</b>
<b>7.1</b>	<b>Test Case Overview</b>	<b>86</b>
<b>7.2</b>	<b>Numerical Results</b>	<b>87</b>
<b>7.3</b>	<b>Conclusions</b>	<b>94</b>
<b>CHAPTER 8.</b>	<b>Protection System Performance during GMD</b>	<b>95</b>
<b>8.1</b>	<b>Dynamic State Estimation-Based Protection</b>	<b>97</b>
8.1.1	Quadratized Dynamic Model for Protection Zone	97
8.1.2	Unconstraint Optimization Method for Dynamic State estimation	99
<b>8.2</b>	<b>Instrumentation Channel Error Correction</b>	<b>100</b>
8.2.1	Current Instrumentation Channel Measurement Models	101
8.2.2	Voltage Instrumentation Channel Measurement Models	105
<b>8.3</b>	<b>Protected Device Modeling</b>	<b>108</b>
<b>8.4</b>	<b>Validation of Error Correction Results</b>	<b>109</b>
<b>8.5</b>	<b>Comparison against Conventional Protection</b>	<b>120</b>
8.5.1	Transformer Protection	122
8.5.2	Capacitor Bank Protection	125
<b>8.6</b>	<b>Conclusions</b>	<b>127</b>
<b>CHAPTER 9.</b>	<b>Conclusions and Future Work</b>	<b>129</b>
<b>9.1</b>	<b>Conclusions</b>	<b>129</b>
<b>9.2</b>	<b>Future Work</b>	<b>130</b>
<b>REFERENCES</b>		<b>132</b>
<b>VITA</b>		<b>140</b>

## LIST OF TABLES

Table 2.1 Classification of Frequency-Dependent Models in terms of Topologies .....	10
Table 4.1 Test Transmission Line Parameters .....	28
Table 4.2 Parameters for GIC Event Test .....	36
Table 5.1 Symbols Used in Magnetic Circuit .....	42
Table 5.2 Test Case Parameters .....	48
Table 6.1 Devices in Test Case Substations .....	64
Table 6.2 Coordinates of Buses .....	79
Table 6.3 Parameters for Test Case 2 .....	80
Table 7.1 Example System Parameters .....	86
Table 8.1 Instrumentation Channels Parameters .....	110
Table 8.2 Test Faults for Transformer .....	122
Table 8.3 Test Faults for Capacitor Bank .....	125



## LIST OF FIGURES

Figure 2.1 The Chain from Solar to Earth[3].....	6
Figure 3.1 Overview of the Research .....	16
Figure 4.1 Illustrative Example of Skin Effect .....	20
Figure 4.2 Multi-layer Conductor Model.....	22
Figure 4.3 Pi Model for Multilayer-conductor Example .....	24
Figure 4.4 Multi-layer Soil Model .....	25
Figure 4.5 Pi model for Broadband Transmission Line Model Example .....	26
Figure 4.6 Equivalent Resistance Compared with Theoretical Value .....	28
Figure 4.7 Equivalent Inductance Compared with Theoretical Value.....	29
Figure 4.8 Equivalent Resistance Compared with Carson's Equation .....	30
Figure 4.9 Equivalent Inductance Compared with Carson's Equation.....	30
Figure 4.10 Comparison of Mutual Resistance.....	31
Figure 4.11 Comparison of Mutual Inductance .....	31
Figure 4.12 Pi Equivalent Model for Transmission Line during GMD.....	34
Figure 4.13 Broadband Transmission Test Case .....	36
Figure 4.14 Overall Simulation Results.....	37
Figure 4.15 Zoomed-In View at the Beginning of GMD Event (at 0.1s) .....	37
Figure 4.16 Zoomed-In View at the Ending of GMD Event (at 1.9s) .....	38
Figure 5.1 Two Winding Y-Y Transformer Electric Circuit Model.....	41
Figure 5.2 Iron Core Structure of a Three Winding Core Form Transformer .....	43
Figure 5.3 Magnetic Circuit for Three-Phase Core Form Transformer.....	43
Figure 5.4 (a) Piece-wise linear B-H curve (b) Nonlinear Reluctance Model.....	45
Figure 5.5 Single-Phase Transformer Model.....	46
Figure 5.6 Three Winding Single-Phase Transformer Electric Circuit .....	46
Figure 5.7 Test Case Overview.....	48
Figure 5.8 Comparison of Primary Current with Zero Load .....	49
Figure 5.9 Flux Path for Phase A.....	50
Figure 5.10 Third Order Harmonic in Tertiary Winding Current.....	51

Figure 5.11 Primary Winding Phase A Current before the GMD .....	52
Figure 5.12 Phase A Current after the Onset of the GMD.....	52
Figure 5.13 Primary Winding Phase A Current during the GMD .....	53
Figure 5.14 RMS Value and Maximum Value of Primary Winding Phase A Current ....	53
Figure 5.15 Path for DC Flux in Shared Core .....	54
Figure 5.16 DC Component of Flux in Air and Tank Path.....	55
Figure 5.17 Active Power and Reactive Power Consumption for Fundamental .....	55
Figure 5.18 DC Component in Flux and Induced Voltage .....	57
Figure 5.19 DC Component in Phase and Neutral Current .....	57
Figure 5.20 Normalized Harmonics Components in Primary winding Phase Current.....	58
Figure 5.21 Tertiary Winding Connection for Mitigation Method.....	59
Figure 5.22 Examination of Mitigation Method .....	60
Figure 6.1 Test System Substations Overview .....	62
Figure 6.2 Substation RMT Configuration .....	63
Figure 6.3 Neutral Currents at Substation RMT .....	65
Figure 6.4 Neutral Current at Substation Groundings during GIC events, Part 1 .....	68
Figure 6.5 Neutral Current at Substation Groundings during GIC events, Part 2 .....	69
Figure 6.6 Neutral Current at Substation Groundings during GIC events, Part 3 .....	70
Figure 6.7 Neutral Current at Substation Groundings during GIC events, Part 4 .....	71
Figure 6.8 Illustrative case 1: System Overview .....	77
Figure 6.9 Illustrative case 1: Measurements of Transmission Line 1 .....	77
Figure 6.10 Illustrative case 1: Measurements of Transmission Line 2 .....	78
Figure 6.11 Illustrative case 1: Results of Geoelectric Field Estimation.....	78
Figure 6.12 Illustrative case 2: System Overview .....	79
Figure 6.13 Illustrative case 2: Results of Geoelectric Field Estimation, Case 1 .....	81
Figure 6.14 Illustrative case 2: Results of Geoelectric Field Estimation, Case 2 .....	81
Figure 7.1 GMD Testing System Overview .....	85
Figure 7.2 GMD Study Area.....	86
Figure 7.3 DC Current at Neutral of Transformers.....	88
Figure 7.4 Harmonic Analysis of Transformer 3 Phase Current .....	88
Figure 7.5 Harmonic Analysis of Transformer 4 Phase Currents.....	89

Figure 7.6 Harmonic Analysis of Transformer 3 Neutral Current.....	89
Figure 7.7 Harmonic Analysis of Transformer 4 Neutral Current.....	90
Figure 7.8 Symmetric Component of Harmonics in Transformer 3 .....	90
Figure 7.9 Symmetric Component of Harmonics in Transformer 4 .....	90
Figure 7.10 Harmonic Analysis of Generator 1 Phase Current .....	92
Figure 7.11 Harmonic Analysis of Generator 2 Phase Current .....	92
Figure 7.12 Base Frequency Reactive Power Production of Generators.....	93
Figure 7.13 Harmonics Reactive Power Production of Generators .....	93
Figure 8.1 Overview of the Estimation Based Protection.....	97
Figure 8.2 Equivalent Circuit of CT's Primary Current Estimation .....	101
Figure 8.3 Equivalent Circuit of PT's Primary Voltage Estimation .....	105
Figure 8.4 Capacitor Bank Modeling.....	109
Figure 8.5 Test System for EBP with Error Correction.....	110
Figure 8.6 Exact Measurements in Protection Zone 1: Event A-1 .....	113
Figure 8.7 Exact Measurements in Protection Zone 1: Event A-2 .....	113
Figure 8.8 Exact Measurements in Protection Zone 1: Event A-3 .....	114
Figure 8.9 Validation of Error Correction: EBP Results Comparison, Event A-1 .....	115
Figure 8.10 Comparison of Currents in Event A-1 .....	115
Figure 8.11 Comparison of Voltages in Event A-1 .....	116
Figure 8.12 Validation of Error Correction: EBP Results Comparison, Event A-2 .....	117
Figure 8.13 Comparison of Currents in Event A-2.....	117
Figure 8.14 Comparison of Voltages in Event A-2 .....	118
Figure 8.15 Validation of Error Correction: EBP Results Comparison, Event A-3 .....	119
Figure 8.16 Comparison of Currents in Event A-3.....	119
Figure 8.17 Comparison of Voltages in Event A-3 .....	120
Figure 8.18 PT Channel Error Correction Result .....	122
Figure 8.19 Differential Protection Performance for the Transformer .....	124
Figure 8.20 EBP Performance for Transformer Protection .....	125
Figure 8.21 Neutral Current Relay Performance for Capacitor Bank .....	126
Figure 8.22 EBP Performance for Capacitor Bank Protection .....	127

## SUMMARY

Geomagnetic disturbances (GMD) occur when solar activity increases and solar wind interacts with the earth's magnetic field. This interaction affects power systems in the form of geomagnetically induced current (GIC), which refers to a quasi-DC current flowing through transmission lines and transformer windings. Although different electronic devices in the system are affected, the bulk transmission system is more vulnerable to disturbance due to usually large geographical distances. A longer distance means a higher potential difference between grounds, introducing larger GIC into the system. When geomagnetic disturbances occur, the quasi-DC current may flow in the transformer windings leading to severe half-cycle saturation. This saturation leads to distorted magnetizing current and accompanying harmonics flowing into the transmission lines. The DC component and harmonics generated by GIC threaten the normal operation of the power grid. Past solar events have resulted in overheating and structure damages in transformers, mis-operation in protective relays, and even blackout of the grid. Experimental results have validated the observed response of power systems to GIC.

To understand the GIC impact and protect transformers and other power system equipment, a time domain simulation based analysis is presented in this dissertation. This analysis starts with developing the device models in time domain considering the effect of GIC, such as transformers saturation and harmonics flowing through transmission lines. A set of physically based models are developed in this dissertation including a low-frequency broadband model and transformer models with detailed magnetic circuits. The

union of these models provides an accurate computation of quasi-DC current flow and harmonics during a GIC event in the time domain.

The results of the time domain simulation are utilized towards a further analysis of the impacts of GIC. The directional sensitivity of power grids to GMD and the transients of GIC are investigated. The performance of the protection scheme and instrumentation channel error during GMD are examined. The results demonstrate the advantage of the time domain based GIC analysis, which captures all the relevant transients, while conventional GIC analysis ignores detailed transients occurring during GMD activities, including the rise of GIC at the beginning of GMD, the variation of the flux in different transformer configurations, the increase of instrumentation channel errors, and the mis-operations of legacy protective relays.

# CHAPTER 1. INTRODUCTION

## 1.1 Problem Statement

Geomagnetic disturbances (GMD) occur when solar activity increases, resulting in an increased influence on the earth's magnetic field by charged particles released from the Sun. According to Faraday's law of induction, the variation of magnetic field density through a specific area results in an induced electromotive force (EMF). Although different electronic devices in the system are affected, the bulk transmission system is more vulnerable to this disturbance due to usually large geographical distances. A longer distance means a higher potential difference along the transmission line. This phenomenon affects power systems in the form of geomagnetically induced current (GIC), which refers to the induced current flowing through transmission lines and transformer windings. In practice, the frequency relevant to GIC is in the range from 0.0001 Hz to 1 Hz, which is a quasi-DC component. During GMD events, the quasi-DC current may be injected into the neutral of transformers, reactors, etc. The iron core will suffer half-cycle saturation, and the equivalent magnetic reluctance drastically increases. As a result, the magnetizing currents significantly increase. Besides, the waveforms are severely distorted and rich in harmonics. These harmonics and related overheating may destroy the transformers (melt the windings) as it has happened at the Salem nuclear plant in NJ during the GMD in 1989 [1]. In addition, if protective relays are not designed to tackle this situation, mis-operation will occur due to the unexpected harmonics, which led to a blackout of the Hydro-Québec power system in 1989[2].

Models that accurately represent the effects of GMD on the power system are important for a realistic assessment of GICs. While individual components have been extensively studied under GICs, similar comprehensive models for system-wide studies are not as well developed. Many approaches use a DC network model to compute the flow of the DC component into the system and then project the effect of DC on the system. Although these simplifications reduce the computation burden, only a rough estimation of the GIC impact is generated and the accuracy of the simulation is compromised. The detailed magnetization characteristics of iron core devices and high order harmonic components are discarded. These approaches cannot capture the interaction of DC, fundamental and harmonics on a network-wide basis. The lack of this valuable information prevents a thorough investigation of GIC. For instance, the equivalent magnetizing inductances of transformers vary during GMD due to saturation, which in turn affects the distribution of GIC. In addition, without the system-level harmonic analysis, the propagation of the harmonics throughout the system and performance analysis of multiple protective relays may not be trustworthy. Instead, the time domain based analysis method can fully capture the system dynamics during GMD events. Such a method should model the study system in the time domain and consider the harmonics generated by GIC.

## **1.2 Research Objectives**

The objective of the proposed research is to develop a time domain analysis scheme for GIC analysis. Compared with existing methods that are based on simplified power flow, the time domain method is able to capture the transients during the onset and retreat of GMD. It is also capable of precisely analyzing the harmonic component resulting from

the saturation of iron cores in transformers and reactors. One major issue in the time domain analysis is the accuracy of the device models. During GMD, the DC components and harmonics flow through the grid. Therefore, a set of high-fidelity power device models is required to conduct an accurate analysis. For instance, the impedance of the transmission lines depends on the frequency of the current flowing through them. A constant impedance line model will introduce substantial errors during the GMD study. In this study, a detailed time domain analysis scheme is developed, which consists of frequency-dependent circuit models, magnetic circuit models with nonlinear reluctance for iron core devices. This scheme is utilized to study several fundamental aspects during GMD events, including the harmonic spectrum of transformer current, the increase of reactive power consumption, and the instrumentation channel error due to DC offset.

### **1.3 Thesis Outline**

The dissertation is organized as follows.

Chapter 2 presents the literature related to the background of GMD and GIC. The related devices modeling such as transmission lines and transformers are discussed. In addition, the modeling of GIC and the impact of GIC on power systems are reviewed.

Chapter 3 contains an overview of the proposed time domain analysis method for GIC related studies, which includes a set of time domain devices with accurate responses to GMD.

Chapter 4 describes the low-frequency broadband transmission line. This line model is capable of reproducing the frequency characteristics from 0.0001Hz to 1200Hz,



which covers the important frequency range for GIC analysis. The accuracy of the proposed model is examined via numerical simulations.

Chapter 5 develops the transient model for transformers with magnetic circuits. During a GIC event, the saturation of transformers is the major source of abnormality, and the configurations of transformers also determine the vulnerability of the transmission system. Multiple transformer models with different winding configurations and iron core structures are compared.

Chapter 6 presents a combination of the time domain models developed in previous chapters and constructs the grid-level test cases. These test cases enable the investigation of the transients of GIC during GMD events through time domain simulation, at different locations in the grid. Besides, the voltage/current measurements at the terminals of transmission lines can be utilized to estimate the magnitude of GMD.

Chapter 7 presents the modeling approach and provides results of the levels of harmonics generated by GIC as well as the propagation of the harmonics throughout the system. Comparisons of the proposed model to other methods reported in the literature are provided. These comparisons indicate that the level of harmonics can be miscalculated if simpler models are used.

Chapter 8 investigates the performance of protective relays during GMD. The performance of a state estimation based protection scheme (EBP) is examined and compared with conventional relays. In addition, instrumentation channel error during GMD is studied and an error correction method is implemented, which further improves the performance of EBP and is especially applicable when GMD occurs.

Chapter 9 summarizes the research work and outlines the results and contributions of this dissertation. In addition, several possible future work directions are discussed.

## CHAPTER 2. LITERATURE REVIEW

In this chapter, we present a literature review in the study of GIC. The background knowledge for geomagnetically induced current (GIC) and geomagnetic disturbance (GMD) is introduced in section 2.1. Next, section 2.2 to section 2.5 investigate the power equipment related to GIC, including transmission lines, transformers, instrumentation channels, and protective relays. GIC analysis methods for power systems are studied in section 2.6. Finally, section 2.7 summarizes the literature review.

### 2.1 Geomagnetically Induced Current

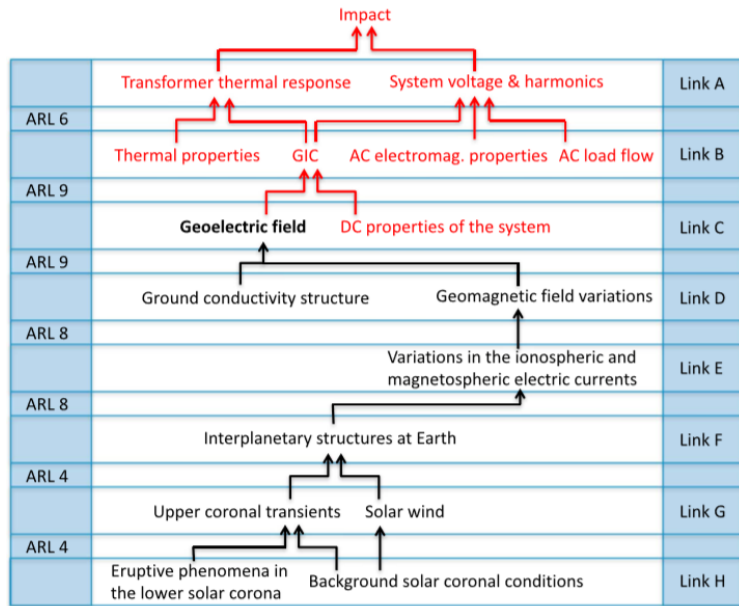


**Figure 2.1 The Chain from Solar to Earth[3]**

Geomagnetic disturbances (GMD) refer to the terrestrial geomagnetic field variations resulting from the outflow of solar atmospheric charged particles when solar

activity increases[3]. This interaction affects power systems in the form of geomagnetic induced current (GIC), which refers to the induced current flowing through transmission lines and transformer windings. The occurrence of GMD follows a specific 11-year cycle related to solar activities [4], and peaks in storminess occur every 11 years. In addition, the sunspots align in a reversed direction in the adjacent cycle, so the odd-numbered cycle is more impactful when sunspot and the earth's magnetic field are anti-parallel. The detailed reasoning of GIC is complicated, but aurora substorms, geomagnetic pulsations and sudden geomagnetic commencements are the major reasons[5] of the occurrence of GIC. During the same GMD event, regions at high geomagnetic latitudes are more vulnerable to GIC, such as North America and Scandinavia[1]. The earth structure[6] also decides the severity of GIC. In general, regions with high earth conductivity are more vulnerable to GIC [7], [8]. There exist several indices[9]–[11] for large-area geomagnetic disturbance, such as Kp index, Ap index. These indices are derived from measurements at global geomagnetic observatory sites. These indices indicate worldwide geomagnetic activities and provide information for GIC related studies. However, due to their large sample intervals (usually one or three hours), it is difficult to relate them with the magnitude of GIC. In addition, some researchers[11] believe that Kp and Ap indexes are not appropriate for predict GIC since these indexes become saturated during large storm events. Instead of indices, they use comparisons of storm morphology to achieve a better understanding of GIC. Figure 4.1 presents the chain from solar activities to the impact of GIC on the power system, and this proposal is related to link A to link C.

Although different electronic devices on earth are affected during GMD events, the bulk transmission system is more vulnerable to disturbance due to its growing geographical distance. A longer distance means a higher potential difference between grounds, introducing larger GIC currents to the system. The frequency of GIC is relatively low, ranging from  $10^{-4}$ Hz to 1Hz. Therefore, it is usually treated as a quasi-

DC component[12]. There are many reports of geomagnetic effects on the power system in the last century, especially during the 22<sup>nd</sup> cycle. For example, the Hydro-Quebec power system collapsed during magnetic storms in 1989[2], [13], after several static Var compensators were tripped due to harmonics generated by saturated transformers. 6 million residents were affected for over 9 hours, and total economic impact was \$13.2 million, including \$6.5 million from repair and replacement of transformers, thyristors and surge arresters. The same year in the U.S., a GSU transformer in Salem Nuclear Plant[1], [14] needed replacement due to the thermal damage during large intensity but short duration GIC event. The stray flux during transformer saturation heated hotspots in external core structures. The replacement energy cost was \$400,000 per day. In October 2003[5], a GIC event led to a large scale blackout in the southern region in Sweden. During this one-hour blackout, about 50,000 customers were affected.

## **2.2 Frequency-Dependent Transmission Line Models**

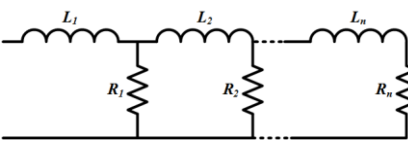
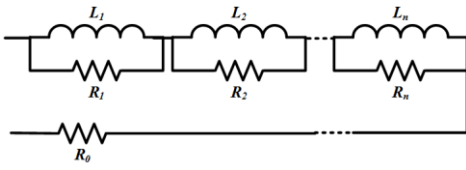
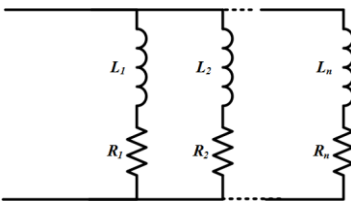
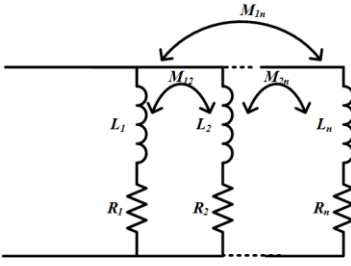
During the GIC event, the harmonics in circuits become complicated. GIC itself introduces DC current, and half-cycle saturation distorts magnetizing current in transformers. Paper [15]–[17] shows that harmonics range from 2<sup>nd</sup> order to 20<sup>th</sup> order during the GIC event. Therefore, a frequency-dependent transmission line model is needed to simulate the evolution of the system accurately. Conventionally, basic transmission line models serve the fundamental frequency (60Hz in the U.S.). However, due to skin effect, the equivalent impedance of a conductor is not constant as frequency varies. One approach to consider the frequency dependence of transmission line parameters is to perform the analysis in the frequency domain and transform the responses back to the time domain using inverse Fourier transformation [18], [19]. This approach is accurate in theory and has been integrated into some power system transient solvers. However, this approach is laced with a heavy computational burden because they require the computation of convolution integrals in each time step. Reference [20]

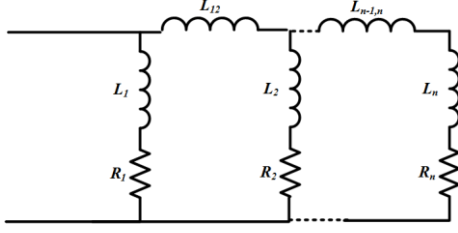
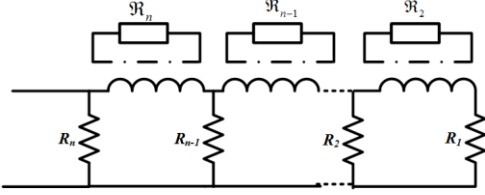
discusses the integration of frequency-dependent grounding impedances into a frequency-dependent power line model, and inverse Fourier transforms were used for impulse response in time domain.

Meanwhile, there are many attempts to reproduce this frequency property directly in the time domain, which reduces the computational burden. Many of them use a fictional impedance network, such as the R-L ladder, Cauer or Foster network, to represent the frequency-dependent conductor. Usually, researchers divide the conductors into many filaments or layers, and the elements in the network are associated with resistance and inductance of layers. There exist multiple ways to divide the conductors. Based on the differential equation derived from the physics of skin effect, Yen et al. [21] propose a method to divide conductor into rings. The thickness of the rings is chosen to achieve a constant resistance ratio between rings. Although the authors report a good agreement of the model with the experiment in a wide frequency range, the calculation of inductance lacks clear physical meaning in their model. Kim et al. [22] modify Yen's method by introducing a ratio between inductance. However, in order to make sure the equivalent inductance consistent with exact value, a complex polynomial is solved for the inductances, and it becomes restrictive as the number of layers grows. Sen et al. [23] work on an even larger frequency range (up to a few GHz). They directly give a list of recommended resistance and inductance for the innermost branch, and the other branches are formulated by multiplying an empirical value. The computation burden is largely reduced, but the resulting network has low accuracy and insufficient physical meaning. Paper [24] considers the mutual inductance between layers, calculating from magnetic energy, but only the adjacent layers are considered. Paper [25] introduces a dual Cauer circuit, using a magnetic circuit to represent the inductance of layers. Meanwhile, other authors prefer modeling rectangular conductors. In [26], [27], authors divide the section into a large number small rectangular sections, and [27] also proposes a method to reduce

the dimension of the equivalent network to achieve a balance between accuracy and computation burden. However, conductors used in transmission lines possess the geometric shape closer to circles. Also, the process is much more complicated than the division into rings mentioned earlier. In addition to these approaches, other researchers do not depend on physical explanation [28], [29], they try to reproduce the frequency property using optimization or fitting method. In Table 2.1, the impedance networks used in aforementioned literature are classified according to their topology. A detailed classification of Cauer Foster network is available in [30] .

**Table 2.1 Classification of Frequency-Dependent Models in terms of Topologies**

Type	Topology	Reference
Physical Cauer		[21], [22], [28]
Series Foster		[29]
Parallel Foster		[23], [31]
Parallel Foster with mutual inductance		[26], [27]

Parallel Foster with mutual inductance for adjacent layers		[24]
Dual Cauer circuit		[25]

### 2.3 Transformer Models

During a GIC event, transformers are usually the source of abnormality[7], and the configurations of transformers [32] also determine the vulnerability of the transmission system. When geomagnetic disturbances occur, a DC excitation will be applied to the transformer, leading to severe half-cycle saturation[14]. The resulting DC component in flux usually brings transformers working under abnormal states. Possible outcomes include: reactive power consumption increase[15], [33]; magnetizing current growth and distortion[34]. These changes will challenge transformer cooling and protection[10]. Literature reports the temperature rise in tie plates[35], tank walls [1], and windings[36]. Researchers in [37] claim that the temperature rise itself will not affect the operation of the transformer. Instead, the occurrence of overheating and winding damage is a result of system instability experienced during or after the GIC event. However, other researches [38] claim that, due to flux distortion, GIC events have a severe thermal impact on transformers, even at areas considered to have low GIC risk. In [39], the authors point out the GSU transformers in GIC vulnerable areas are more likely to fail than those in other areas. After investigating the annual failure of large transformer in



Greece and the solar activity pattern, reference [40] concludes these transformers got a “considerable” influence from solar activity.

To alleviate the GIC impact and protect transformers, many researchers have conducted experiments on transformers with GIC. Change on real power transference, impedance, losses, and temperature are observed in a scaled-down transformer under GIC[41]. Test results on small-scale transformer models with different iron core structures are reported in [42]. They found that single-phase three-legged cores were most susceptible among different configurations. Reference [43] tests a 30kVA distribution transformer, reports the magnitude of the excitation current rises to 30 times the normal value. Some researchers consider voltage control and harmonics effect in an experiment of two 463 MVA system transformer under GIC. In [15], researchers estimate and validate harmonic currents and reactive power of transformers, with their nameplate and core design information. FEM method is used in [44] to assess the susceptibility of transformers with different transformer core designs, while [34] uses magnetic circuits to analyze different core structures. Paper [17] claims that during saturation, the tank is a major path for flux, and a magnetic model with the tank is needed. Authors in [45] find the existence of air path inductance in the five-leg transformer model will affect the result significantly.

## **2.4 Instrumentation Channel Error during GMD**

During a GMD event, the DC offset in voltage and current will challenge the operation of instrumentation transformers. References [46] points out that the error in current transformer (CT) secondary current will increase when the GIC presents, and the magnitude of error can be reduced by choosing CT with a higher ratio and burden with lower impedance. In addition, the authors pointed out that the transient performance of CT degrades. The time-to-saturation decreases if pre-fault GIC flow exists and the flow is

in the same direction as the fault offset. Another similar research is reported in reference [47]. Simulation results show that the CT error introduced by GIC in the steady state is not obvious. Meanwhile, very small dc currents introduce significant error during the first half cycle of a fault. Though the authors believe these errors will not threaten the protective relay operation.

## **2.5 Protective Relays Performance during GMD**

Paper [48] presents a detailed discussion about protective relay under GIC. For capacitor bank unbalance protection, the high amplitude of neutral current during GMD imposes thermal stress on CT burden resistor. CTs with higher continuous current factors should be adopted to prevent CT failure. During GMD events, saturated transformers will generate harmonics in current, and harmonically restrained differential protection for transformers will be blocked. Therefore, the protection scheme may fail to operate during faults. In October 2003[5], the GIC event leads to a large scale blackout in the southern region in Sweden. The major reason was the loss of a 130kV transmission line, which was tripped by an overcurrent relay. Investigation showed that the relay had higher sensitivity at third-order harmonic than the fundamental frequency current. In this case, the relay characteristic value for third harmonics was much lower than the fundamental frequency. After the accident, the involved relay was replaced by a relay that is less sensitive at 150 Hz than at 50 Hz.

## **2.6 Modeling Methods for the Impact of GMD**

Reference [49] discusses two different approaches to model the GIC as equivalent sources in power system: placing voltage sources in the transmission lines or at system ground points. The authors propose that for uniform fields, these two methods are identical; however, sources at the system ground point cannot represent the non-uniform

field because the integration of the non-conservative field is path-dependent. In contrast, placing voltage sources in the transmission lines is able to model the non-uniform fields. In reference [50], [51], authors present methods to simulate the impact of GIC on the power flow of large scale power systems. The simulation is conducted using the DC network, and the network consists of resistance components such as transmission line resistance, substation grounding resistance and transformer winding resistance. Applying the GMD equivalent source to the network yields the GIC flowing into the system. Meanwhile, the reactive power consumption of transformers is calculated using a linear model, which is in terms of the magnitude of voltage and GIC. Researchers in [52] follow a two-step method to assess the GIC. First, the induced geoelectric fields are calculated from magnetometer measurements. Second, the GIC is computed by a DC network with equivalent geoelectric sources. Some researchers investigate the relationship between the level of GIC and the different characteristics of power systems [53]. The authors point out that the resistance of transmission lines, the types of transformers, the grounding resistance and the topology of the system are important factors in determining the magnitude of GIC. The authors also find the capacitors installed at the neutrals of transformers may not be a perfect solution to mitigate GIC, because it only reduces GIC locally, but the GIC at neighbor locations becomes larger. In reference [54], the authors develop a 100-year extreme GMD test case based on actual observed storm events, considering ground conductivity structures and geomagnetic latitudes. Their artificial 100-year extreme scenarios show that at high-latitude areas, the extreme geoelectric field achieves 5 V/km for well-conducting ground areas, and up to 20 V/km, for poorly conducting areas. Meanwhile, in low-latitude areas, the geoelectric field amplitudes range from 0.5V/km to 2V/km depending on the resistance of the earth structure. The boundary locates at about 50° of geomagnetic latitude.

## 2.7 Summary

In this chapter, literature related to GMD and the impact of GIC on the power system is reviewed. Transformers play a significant role in the dynamics of the power system during GMD events because they become generators of harmonics which amplify the effects of GIC on power systems. The harmonics generated by iron core saturation challenge the normal operation of the system. The arising problems include increasing reactive power consumption, instrumentation channel error, protective relay misoperation, etc. The accuracy of the existing DC network simulation methods is limited since the harmonics are not modeled directly. Therefore, a time domain simulation method considering the DC component and harmonics is introduced in this proposal. This method also enables the study of the dynamic interaction of harmonics with other parts of the system, including the performance of transformers, instrumentation channels and protection relays. These devices are designed to work well under nominal frequency (60 Hz). Therefore, the unexpected status of these devices with harmonics penetration can be revealed by the proposed method.

## CHAPTER 3. RESEARCH OVERVIEW

The objective of the research in this dissertation is to develop a comprehensive time domain simulation scheme considering the DC and harmonic components introduced by GIC and use the time domain results to conduct GIC related analysis. This chapter describes an overview of the proposed research.

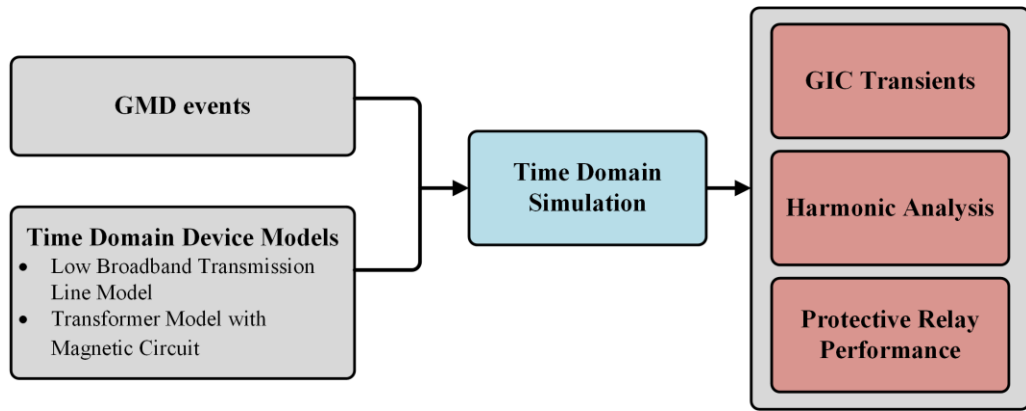


**Figure 3.1 Overview of the Research**

### 3.1 Method Overview

Figure 3.1 presents an overview of the proposed approach. The approach starts with time domain models developed for GIC related study, i.e. device models with accurate frequency characteristics within GIC related frequency range. These models include the low broadband transmission line model and the transformer model with magnetic circuits: The transmission line model considers the frequency-dependent parameters of overhead conductors and soils. The targeted frequency range is zero to 1.2 kHz which is sufficient for geomagnetically induced current analysis in transmission circuits. The accuracy of the line model in this frequency range is documented by

comparing it to Carson's equations. At the same time, transformers are saturated during GIC, which is determined by the nonlinear relationship between magnetic flux and magnetizing current. When there is a DC flow in transformer winding, the transformer is forced to work in the nonlinear region for part of a half cycle, resulting in distortion in magnetizing currents, which is represented by a detailed magnetic circuit in the proposed model. In summary, these proposed time domain models achieve high accuracy with a minimal computational burden. The use of the models is illustrated with the GIC test case analysis.

After the device-level model is developed, the power grid can be represented by a combination of devices. Given a specific GMD time series, the response of the system in the time domain is available immediately. This scheme facilitates further study such as the transients of GIC, harmonic analysis, and protective relay performance analysis.

When a specific GMD occurs, the corresponding induced current, i.e. GIC appears. The conventional GIC analysis methods mainly focus on the steady state value of the induced current. The transients of GIC are ignored due to the simplification of the method, which models the network as a purely resistive network. Nevertheless, the proposed time domain simulation results enable complete modeling of the network with resistance and inductance, even nonlinear inductance inside transformers. Therefore, much more information can be obtained from the resulting transients of GIC. In addition, the time domain results are transformed into the frequency domain, and the harmonics generated by GIC are also available. The pattern of harmonics and the impact on the operation of the grid are investigated. Another application of the time domain method is the protective relay performance. Due to the GIC and corresponding harmonics, the

measurements observed by relays are distorted. Therefore, mis-operations could occur and the reliability of relays is also worth investigating. The performance of several conventional protective relays and an estimation based protection scheme are studied. In the meantime, the instrumentation error introduced by GIC is also investigated as it may drastically impact the inputs of relays.

### **3.2 Summary**

An overview of the proposed time domain analysis method for GIC is provided in this chapter. The main advantages of the research proposed are given as follows. This time domain method consists of device models with accurate characteristics during GIC. Therefore, the simulation results can capture the impact of GIC better. In addition, this time domain method yields results with much more details, compared with the simplified DC approach. These details enable the related analysis, such as the transients of GIC, the harmonics analysis, and the protective relay performance analysis.

## **CHAPTER 4.    LOW-FREQUENCY BROADBAND TRANSMISSION LINE MODEL**

Transmission circuits play an important role in the penetration of GIC into the power system. Under steady state without any fault or GIC, the current in transmission lines is mainly composed of the fundamental frequency. While during a GIC event, DC components are arising from GIC and harmonics due to the saturation of transformers. The constant impedance transmission line model used for steady state analysis is only valid for fundamental frequency, which may introduce large errors during GIC events, so a broadband transmission line model with the accurate response over a wider range of frequencies is needed to accurately perform parametric studies. This section proposes a low-frequency broadband transmission line model based on the physical properties of transmission line conductors. It captures the frequency dependence of both line conductors and the soil in the time domain. The proposed method consists of a multilayer conductor model and a multilayer soil model. This method is easy to implement and yields accurate results in the frequency range of interest for the GIC analysis, which is 0.0001Hz to 1200Hz.

### **4.1    Model Derivation**

#### *4.1.1    Motivation*

The skin effect leads to higher AC current densities near the surface of a conductor. By solving Maxwell equations for a cylindrical conductor, the exact current distribution over the cross-section of the conductor can be obtained. The current density



at radius  $r$  is given in terms of modified Bessel functions [55]. Figure 4.1 (a) depicts the normalized magnitude of current density in the cross-section of a large cylindrical conductor at 60Hz.

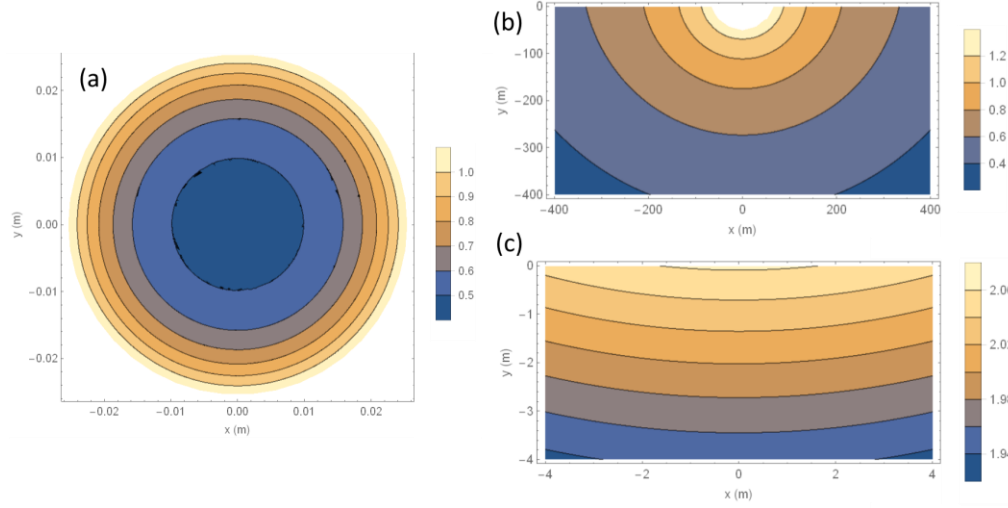


**Figure 4.1 Illustrative Example of Skin Effect**

**((a) current density in conductor (b) electric field in soil (c) soil zoom in view)**

In order to mimic the uneven distribution of current, we propose a multi-layer conductor model by dividing the conductor along the radius into several layers, and assuming the current density is uniformly distributed in each layer. Since the change of current density is more dramatic near the surface, the thickness of layers is decreased correspondingly. In specific, exponentially decreasing thicknesses of the layers are implemented in our model. By calculating the resistances and inductances of each layer and the mutual inductances between layers, a circuit network is formulated. Since each element in the network is derived directly from a physical entity, the network should reproduce the frequency characteristics of the original conductor to some extent.

In practice, overhead transmission lines are grounded, making the earth an additional path. Therefore, the soil also contributes substantially to the frequency response of transmission lines. The AC current tends to concentrate near the surface of the soil, increasing the equivalent resistance of the soil. Carson proposed a solution [56] of transmission line impedance above the earth. Equation (1) gives the electric field in the earth at the location  $(x,y)$  when  $y \leq 0$ , which is induced by the current  $I$  in an overhead conductor with the height of  $h_{ii}$ .  $\sigma_e$  is the conductivity of the soil, which is assumed to be constant. Notice that the electric field depends on  $(x,y)$ , and the equal potential lines in the soil are not perfect half circles. Figure 4.1 (b) and (c) give an example of electric field distribution in the soil at 60Hz. The half-circle assumption only appears accurate on a macroscopic level. Following the assumption of the multi-layer model for conductors, we model soil with multiple layers as well. The parameters of the soil layers are modified to minimize the discrepancy between the layered model and Carson's equations.

$$E_z(x, y) = -jI \frac{\mu_0 \omega}{2\pi} \int_0^\infty \frac{\exp(h_{ii}u + y\sqrt{u^2 + j\omega\mu_0\sigma_e})}{u + \sqrt{u^2 + j\omega\mu_0\sigma_e}} \cos(xu) du \quad (1)$$

#### 4.1.2 Multi-layer Conductor Model

We implemented a multi-layer conductor model to mimic the frequency-dependent parameters of a real conductor. Specifically, the conductor is divided into several layers, and the current density in each layer is assumed to be constant. Its cross-section is depicted in Figure 4.2. At a specific frequency, outer areas have a higher current density than inner ones. Then, each layer can be viewed as a fictional conductor,

and resistance and inductance (including self-inductance and mutual inductance) are calculated separately for each layer.

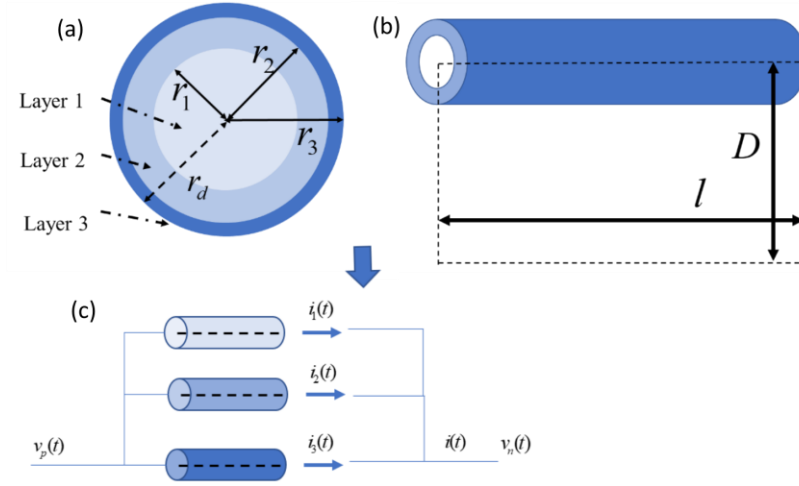


**Figure 4.2 Multi-layer Conductor Model**

**((a)Conductor Cross Section, (b) Conductor Side view (c) Symbolic Circuit Representation)**

Figure 4.2 presents the cross-section of a cylindrical conductor with a radius of  $r_d$ , which is divided into 3 layers. First, the self-inductance of layer 2 is calculated as an example. When the current  $i$  is uniformly distributed, the magnetic field intensity follows equation (2). The magnetic flux linkage in a loop with length  $l$  and width  $D$  is calculated via the integration of the magnetic flux linkage of infinitesimal strips, resulting in (3), and the inductance per unit length is the ratio of flux and current in equation (4).

$$H(r) = \begin{cases} 0 & r \leq r_1 \\ \frac{i}{2\pi r} \frac{r^2 - r_1^2}{r_2^2 - r_1^2} & r_1 \leq r \leq r_2 \\ \frac{i}{2\pi r} & r_2 \leq r \end{cases} \quad (2)$$

$$\lambda = \int_0^D d\lambda(r) = \frac{\mu_0 i l}{2\pi} (C_1(r_1, r_2) / 4 + \ln \frac{D}{r_2}) \quad (3)$$

where

$$d\lambda(r) = \begin{cases} 0 & r \leq r_1 \\ \mu_0 \cdot l \cdot H(r) \frac{r^2 - r_1^2}{r_2^2 - r_1^2} dr & r_1 \leq r \leq r_2 \\ \mu_0 \cdot l \cdot H(r) dr & r_2 \leq r \end{cases}$$

$$C_1(r_1, r_2) = \begin{cases} \frac{(r_2^4 - r_1^4) - 4r_1^2(r_2^2 - r_1^2) + 4r_1^4 \ln(r_2 / r_1)}{(r_2^2 - r_1^2)^2} & , r_1 \neq 0 \\ 1 & , r_1 = 0 \end{cases}$$

$$L_{22} = \frac{\lambda}{i} = \frac{\mu_0}{2\pi} \ln \frac{D}{r_2 e^{-C_1(r_1, r_2)/4}} \quad (4)$$

Next, we can calculate the mutual inductance between layers. The mutual inductance between layer 2 and layer 3 is given in equation (5). A similar procedure applies to other layers.

$$L_{23} = L_{32} = \frac{\mu_0}{2\pi} (C_2(r_2, r_3) + \ln \frac{D}{r_3})$$

$$C_2(r_2, r_3) = \frac{(r_3^2 - r_2^2) / 2 - r_2^2 \ln(r_3 / r_2)}{r_3^2 - r_2^2} \quad (5)$$

Assuming the overhead transmission line is placed over the soil with perfect conductivity ( $\sigma_e = \infty$ ), then  $D = 2h_i$ ,  $h_i$  is the height of the conductor. In addition, the mutual inductance is determined by the outer layer, i.e.  $L_{13} = L_{31} = L_{23} = L_{32}$ . In general, an  $n$ -layer impedance network for a conductor is represented by the following equation (6),

$$v_k(t) - v_{k+1}(t) = \mathbf{R} \cdot \mathbf{i}(t) + \mathbf{L} \frac{d\mathbf{i}(t)}{dt} \quad (6)$$

where

$$\mathbf{R} = \begin{bmatrix} R_1 & & & & \\ & R_2 & & & \\ & & R_3 & & \\ & & & \dots & \\ & & & & R_n \end{bmatrix}, \mathbf{L} = \begin{bmatrix} L_{11} & L_{21} & L_{32} & \dots & L_{nm} \\ L_{21} & L_{22} & L_{32} & \dots & L_{nm} \\ L_{32} & L_{32} & L_{33} & \dots & L_{nm} \\ \dots & \dots & \dots & \dots & L_{nm} \\ L_{nm} & L_{nm} & L_{nm} & L_{nm} & L_{nm} \end{bmatrix}, m = n - 1$$

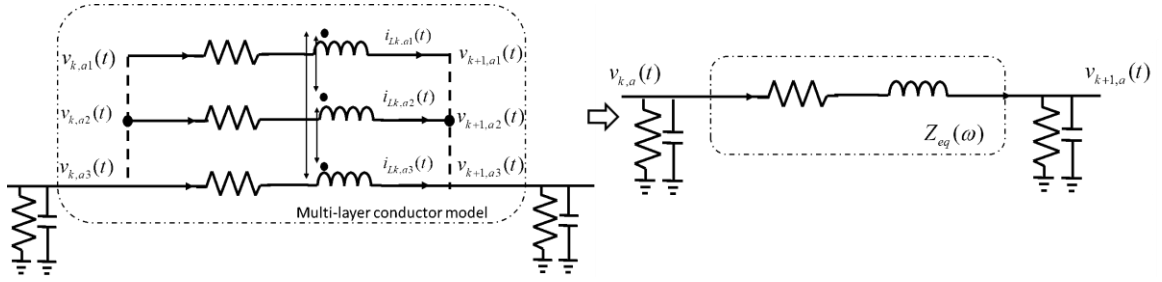


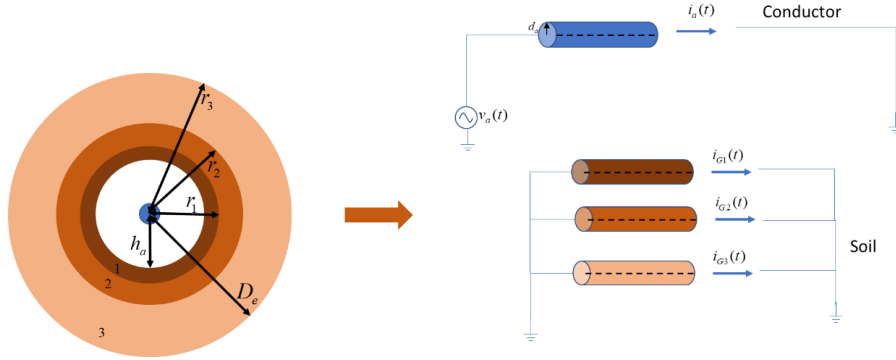
**Figure 4.3 Pi Model for Multilayer-conductor Example**

The resistance matrix  $\mathbf{R}$  is composed of the resistance of each layer.  $\mathbf{i}(t)$  is the vector of currents through each layer. The capacitance and conductance of the transmission line introduce shunt elements connected only to the outer layer of a conductor. To summarize, we represent a small length of a single-conductor transmission line with a  $\pi$  model as shown in Figure 4.3. The equivalent impedance at frequency  $\omega$  is denoted as  $Z_{eq}(\omega)$ . Using a similar approach, we can construct the model of an  $n$ -conductor transmission line.

#### 4.1.3 Multi-layer Soil Model

Next, we continue to consider the impact of soil. Carson [24] explains a way to calculate the impact of soil on overhead lines, which is widely used to model

transmission lines with soil as a return path. Carson's result accounts for different frequencies, i.e. it is a frequency-dependent model, and it is in the form of an infinite series. In order to develop a time domain model, the soil is also divided into several layers. For convenience, the geometric shape of the soil is approximated with rings as well. The equivalent circuit for the system is the following graph. The “inner rings” of soil represent the surface near the overhead transmission line, while the “outer rings” represent the soil in deeper areas.



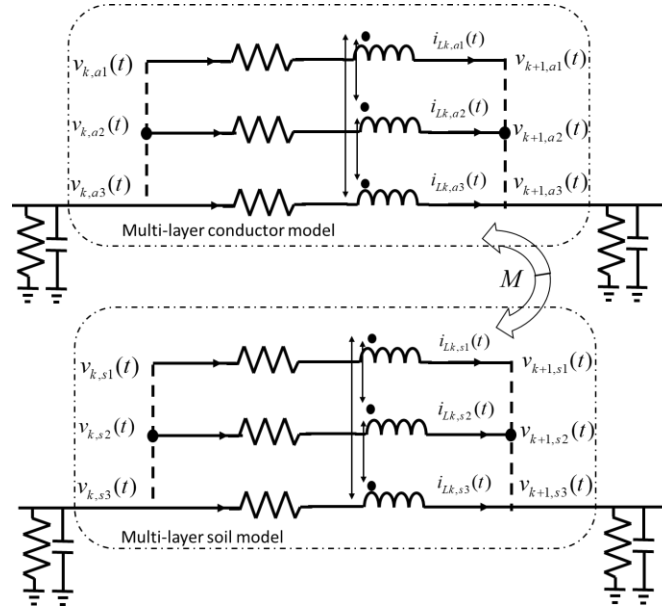
**Figure 4.4 Multi-layer Soil Model**

Figure 4.4 shows an example of a single conductor in the soil ring.  $D_e$  is the equivalent thickness of the soil. When the frequency of the current in the overhead conductor is very low, the magnetic field in the soil spreads over an extremely large area. For practical reasons, we can choose  $D_e$  based on the frequency range we are interested in. In this approximate soil ring, the same calculation procedure for the inductance of conductor layers is applicable. This approximation is less reliable near the surface of the soil. We propose additional modifications to better represent the effect of the soil. Specifically, we replace  $\mathbf{R}$  in equation (6) with  $\alpha\mathbf{R}$ . The scaling matrix  $\alpha$  can transform the resistance of the soil rings to better fit the real characteristics of the soil. The

following empirical formula (7) used in this report yields satisfactory results. To further improve the fitting, an optimization procedure may help determine  $\alpha$ .

$$\alpha_{ii} = 2.5(n-i+1)/(n-1)+1; \quad \alpha_{ij} = 0, \forall i \neq j \quad (7)$$

The low broadband transmission line model is constructed after calculating the self-inductance of each soil layer, the mutual inductance between soil layers, and the mutual inductance  $M$  between soil and conductor layers. Figure 4.5 shows the transmission line model with the multi-layer conductor and multi-layer soil.



**Figure 4.5 Pi model for Broadband Transmission Line Model Example**

## 4.2 Model Validation

In this section, the accuracy of the proposed transmission line model is validated via numerical simulation. The analytical solutions (theoretical value) are presented as benchmarks.

#### 4.2.1 Validation of Self-impedance

An analytical solution of internal impedance exists for cylindrical conductors; the solution is expressed in terms of Bessel functions. Assuming current through a conductor is uniformly distributed in cross-section, then its resistance is  $r_{dc}$  and its internal flux linkage is  $\lambda_i$ . This uniform condition is accurate for DC current ( $f = 0$ ). When AC current flows, the following equation gives modification on  $r_{dc}$  and  $\lambda_i$  to get equivalent resistance  $r_{ac}$  and internal flux linkage  $\lambda_i'$ .

$$x_s = \frac{r_{ac}}{r_{dc}} = \frac{ka}{2} \frac{M_0(ka)}{M_1(ka)} \sin \left[ \theta_1(ka) - \theta_0(ka) - \frac{\pi}{4} \right]$$

$$\xi = \frac{\lambda_i'}{\lambda_i} = \frac{4}{ka} \frac{M_0(ka)}{M_1(ka)} \sin \left[ \theta_0(ka) - \theta_1(ka) + \frac{3\pi}{4} \right]$$

In which,  $k = \sqrt{\omega\mu\sigma}$ ,  $a$  is the radius of the conductor,  $\omega$  is the angular frequency for the AC current,  $\mu$  is the permeability of conductor material,  $\sigma$  is the conductivity of the conductor material. And  $M_0, M_1, \theta_0, \theta_1$  come from modified Bessel functions. The equations for related functions are:

$$I_0(z) = 1 + \frac{(z/2)^2}{(1!)^2} + \frac{(z/2)^4}{(2!)^2} + \frac{(z/2)^6}{(3!)^2} + \dots$$

$$I_0(xj^{0.5}) = M_0(x)e^{j\theta_0(x)}$$

$$zI_1(z) = \int_0^z wI_0(w)dw$$

$$e^{j\pi/2}I_1(zj^{0.5}) = M_1(z)e^{j\theta_1(z)}$$

In general, the equation for the modified Bessel function of the first kind, the order of  $\nu$  is:



$$I_v(z) = \left(\frac{1}{2}z\right)^v \sum_{k=0}^{\infty} \frac{(z^2/4)^k}{k! \Gamma(v+k+1)}$$

**Table 4.1 Test Transmission Line Parameters**

<b>radius (m)</b>	0.0254 (1 inch)
<b>electrical resistivity <math>\rho(\Omega \cdot \text{m})</math></b>	$2.82 \cdot 10^{-8}$ (Aluminum)
<b>relative permeability</b>	1
<b>length(m)</b>	1
<b>soil resistivity <math>\rho(\Omega \cdot \text{m})</math></b>	100
<b>equivalent soil thickness(m)</b>	6500
<b>horizontal distance <math>\Delta x</math> (m)</b>	5
<b>height <math>y_1, y_2</math> (m)</b>	10

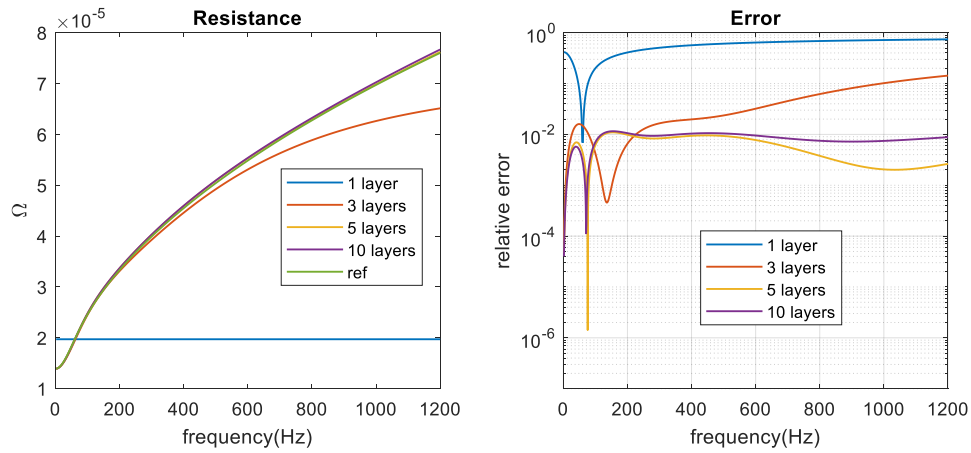


**Figure 4.6 Equivalent Resistance Compared with Theoretical Value**

Next, the equivalent impedance of the multi-layer conductor at different frequencies is compared with the theoretical value. In Figure 4.6 and Figure 4.7, “ref” comes from the theoretical value of impedance at a given frequency, and “3, 5, 10 layers” are the equivalent impedance of the proposed model with different layer numbers. “1 layer” is the constant impedance model determined at 60Hz. The parameters used for the comparison are available in Table 4.1. We can observe that with 5 or more layers,

excellent agreement is obtained between the multi-layer model and the exact analytical solution. The maximum relative error for resistance in the frequency range is about 1%. And for inductance, the relative error is lower than 0.1%.

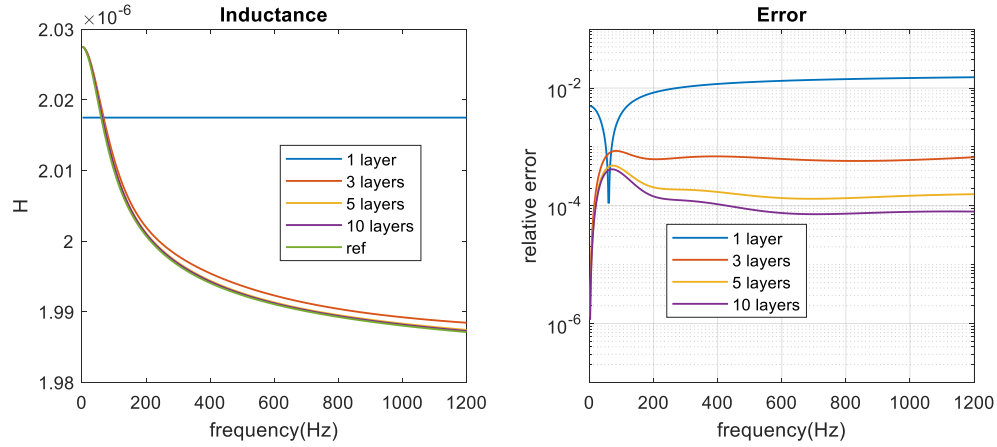
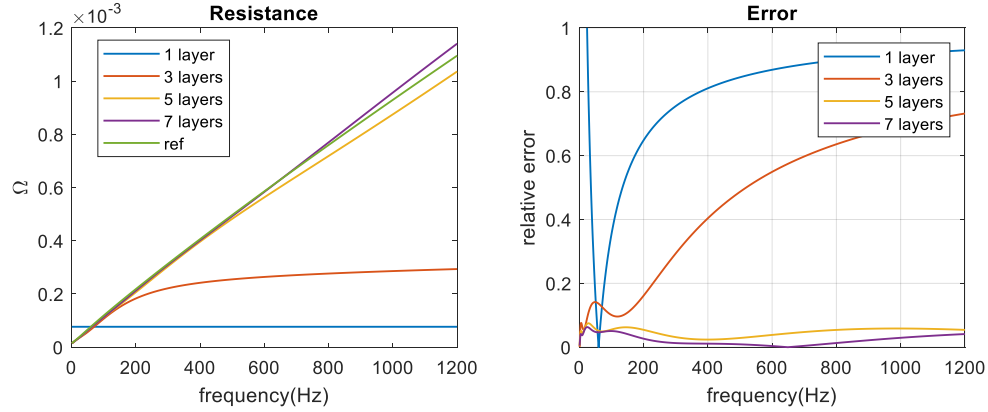


**Figure 4.7 Equivalent Inductance Compared with Theoretical Value**

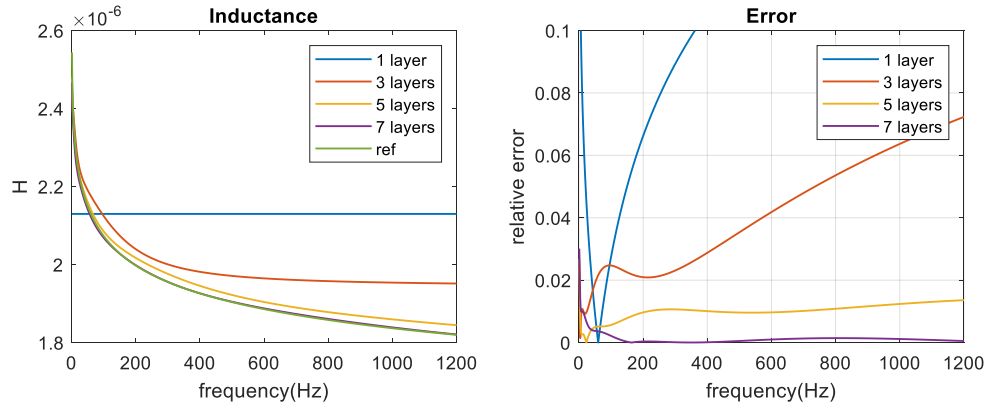
Next, we investigate the equivalent impedance of the conductor considering the soil's effect. The parameters used for the comparison are available in Table 4.1. From Carson's equation, we can calculate the self-impedance  $Z_{aa}$  of conductor  $a$  from:

$$Z_{aa} = \underbrace{r_a + j \frac{\omega\mu}{2\pi} \ln \frac{D_{aa'}}{d_a}}_{\text{ideal impedance with } \sigma_{\text{soil}} = \infty} + \underbrace{\frac{2\omega\mu}{2\pi} (P_{aa} + jQ_{aa})}_{\text{impact of soil}}$$

Where,  $P_{aa}, Q_{aa}$  is a series approximation of a specific integration proposed in Carson's model. Carson's result is utilized as a reference to validate the proposed model.



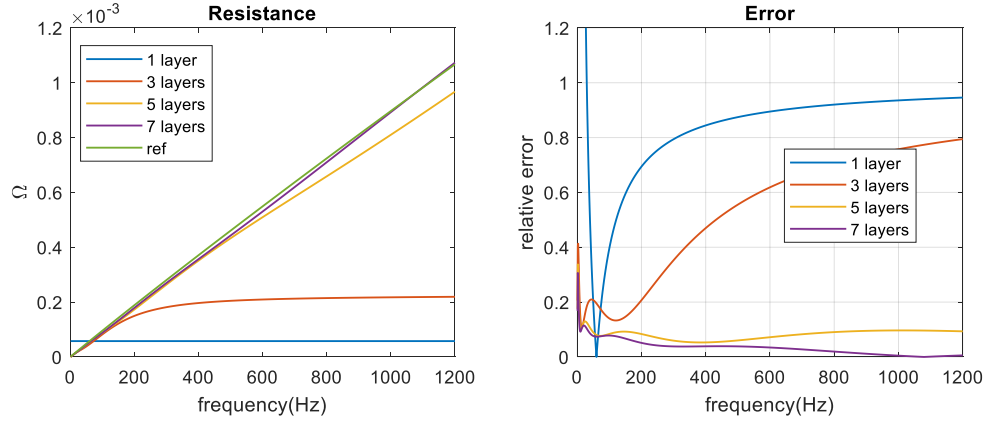
**Figure 4.8 Equivalent Resistance Compared with Carson’s Equation**



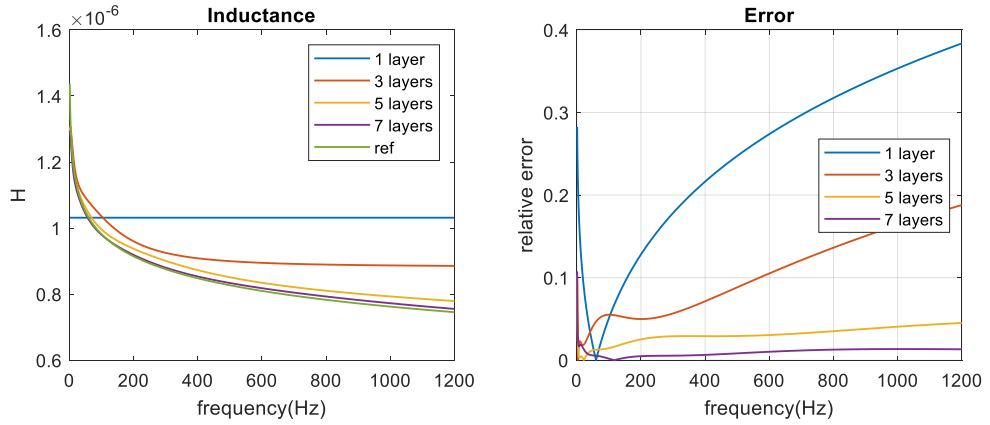
**Figure 4.9 Equivalent Inductance Compared with Carson’s Equation**

Figure 4.8 and Figure 4.9 provide the comparison result between the multi-layer model and Carson’s equations. “3, 5, 7 layers” are the equivalent impedance of the proposed soil model with different layer numbers. “1 layer” means Carson’s result at 60Hz. The overall trend of the proposed model is consistent with Carson’s reference model. For the 7-layer model, the relative error of resistance is about 5% and the relative error of inductance is about 0.1%. To further improve the accuracy, some optimization methods to adjust the elements in the model can be implemented, and this needs more following work. Meanwhile, the constant impedance model, denoted by “60Hz”, presents a large error. The resistance of the constant impedance model has a 100% deviation from

reference value near 0Hz and 1200Hz. From this point of view, the multi-layer model has much-improved accuracy.



**Figure 4.10 Comparison of Mutual Resistance**



**Figure 4.11 Comparison of Mutual Inductance**

#### 4.2.2 Validation of Mutual Impedance

The above sections concentrate on the self-impedance of conductors, but the mutual impedance is also an important part of transmission line models. When the soil is not an ideal conductor ( $\sigma_{soil} \neq \infty$ ), the soil introduces extra mutual inductance and “mutual resistance”. The mutual impedance proposed in Carson’s paper is calculated by:

$$Z_{ab} = j \frac{\omega\mu}{2\pi} \ln \frac{D_{ab'}}{D_{ab}} + \underbrace{\frac{2\omega\mu}{2\pi} (P_{ab} + jQ_{ab})}_{\text{impact of soil}}$$

In this section, the mutual impedance of the multi-layer soil model is compared with Carson's result. Table 4.1 provides parameters for the comparison, and we use 5 layers for the conductors. Results are available in Figure 4.10 to Figure 4.11, which have similar implications as the self-impedance results. The relative error for mutual impedance is lower than 1% in the investigated frequency range, which is at the same level as self-impedance.

### 4.3 Transmission Line Model with Geoelectric Field

#### 4.3.1 Geoelectric Field Modelling

During GMD events, the variation of the geomagnetic field leads to the geomagnetically induced current in transmission lines, which can cause saturation of transformers and mis-operation of relays. To investigate the specific impact of GMD on the power system, the geoelectric field induced by the geomagnetic field is of interest. Near the surface of the earth, the geoelectric field can be decomposed into two directions: eastward and northward, which is calculated by the following equations [12]:

$$\begin{aligned} E_E(\omega) &= Z(\omega)H_N(\omega) \\ E_N(\omega) &= -Z(\omega)H_E(\omega) \end{aligned} \quad (8)$$

In which,  $E_E$  and  $E_N$  are the amplitudes of Eastward geoelectric field and Northward geoelectric field (V/m) correspondingly;  $H_E$  and  $H_N$  are the amplitude of Eastward geomagnetic field and Northward geomagnetic field (A/m) correspondingly;  $\omega$

is the angular frequency of the field,  $Z$  is the earth field impedance ( $\Omega$ ), which is computed according to the earth conductivity model.

In [49], the authors discussed two different approaches to model the GIC equivalent source in power system: placing voltage sources in the transmission lines or at system ground points. The authors concluded that for uniform fields, these two methods are identical; however, only placing voltage sources in the transmission lines is able to model the non-uniform fields, while sources at system ground point cannot because of the integration of the non-conservative field is path-dependent. Therefore, the geoelectric field is modeled as voltage sources in the transmission line.

#### 4.3.2 *Transmission Line Modelling*

The  $\pi$  equivalent model for the transmission line used in this chapter is illustrated in Figure 4.12. For the sake of simplicity, only Phase A and Neutral line are depicted in the figure. This model also applies to the three-phase system. The ordinary differential equation (ODE) system for the model is shown in (9) ~ (11). Equations (9) and (10) describe the currents flowing through two terminals of the transmission line, and (11) describes the voltage difference between the terminals across the line. When the transmission line spans a long distance, the line can be divided into several sections to increase the accuracy of the model [57]–[59]. Therefore, the overall transmission line model consists of a series of single-section  $\pi$  equivalent models.  $D_E(t)$  and  $D_N(t)$  are the equivalent DC sources in each transmission line section, derived from the Eastward geoelectric field and Northward geoelectric field correspondingly. The magnitude of these sources is proportional to the projection of the transmission line, which is shown in

the equation (12), where  $l$  is the distance between the terminals of the transmission line,  $\theta$  is the angle difference between the transmission line and reference axis (eastward direction), and  $n_s$  is the number of sections in the transmission line model.

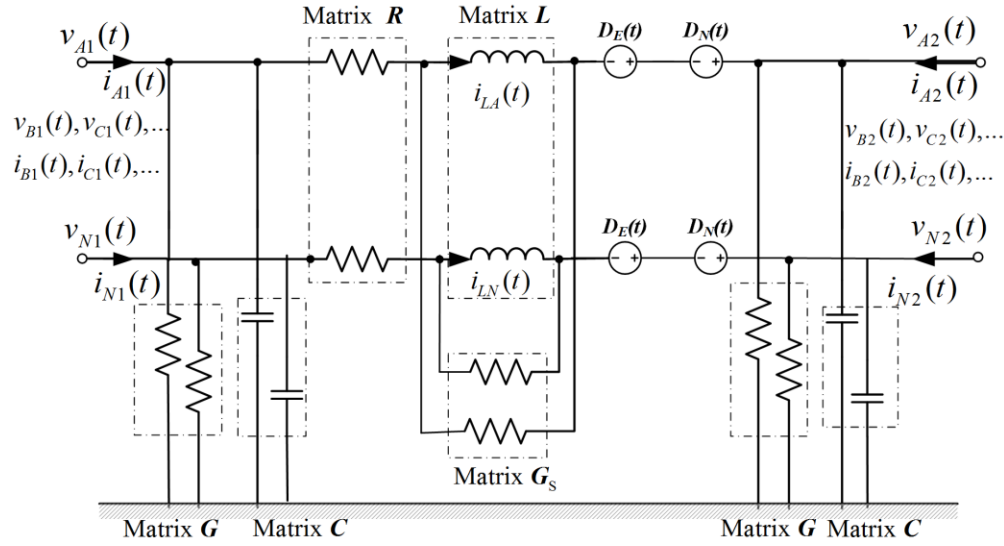


**Figure 4.12 Pi Equivalent Model for Transmission Line during GMD**

Other parameters in the model include:  $\mathbf{R}$  is the series resistance matrix,  $\mathbf{L}$  is the series inductance matrix,  $\mathbf{C}$  is the shunt capacitance matrix and  $\mathbf{G}$  is the shunt conductance matrix. The conductance matrix  $\mathbf{G}_s$  is included to increase numerical stability. These parameters are calculated based on the characteristics of the transmission line, such as the size of conductors and the structure of towers. During GMD events, the DC components and other harmonics such as second and third-order harmonic components increase. Due to the skin effect, the frequency response of the transmission line varies at different harmonics. Therefore, the constant-impedance model derived at the base frequency cannot accurately capture the dynamics during GMD events. The low-frequency broadband transmission line model [60] developed in previous sections is used, which uses an impedance network to reproduce the frequency characteristics of the line.

In summary, the states  $\mathbf{x}(t)$  of the transmission line model include:  $\mathbf{v}_1(t), \mathbf{v}_2(t)$ , the voltages at terminals,  $\mathbf{i}_L(t)$ , the current flowing through the inductors, and  $E_N(t), E_E(t)$ , the local geoelectric field in east direction and north direction.

$$\mathbf{i}_1(t) = \mathbf{G}\mathbf{v}_1(t) + \mathbf{C} \frac{d}{dt} \mathbf{v}_1(t) + \mathbf{i}_L(t) + \mathbf{G}_s \mathbf{L} \frac{d}{dt} \mathbf{i}_L(t) \quad (9)$$

$$\mathbf{i}_2(t) = \mathbf{G}\mathbf{v}_2(t) + \mathbf{C} \frac{d}{dt} \mathbf{v}_2(t) - \mathbf{i}_L(t) - \mathbf{G}_s \mathbf{L} \frac{d}{dt} \mathbf{i}_L(t) \quad (10)$$

$$0 = -\mathbf{v}_1(t) + \mathbf{v}_2(t) + \mathbf{R} \left( \mathbf{i}_L(t) + \mathbf{G}_s \mathbf{L} \frac{d}{dt} \mathbf{i}_L(t) \right) + \mathbf{L} \frac{d}{dt} \mathbf{i}_L(t) - \mathbf{I}_{4 \times 4} D_E(t) - \mathbf{I}_{4 \times 4} D_N(t) \quad (11)$$

where,

$$D_E = l \cos \theta E_E(t) / n_s, \quad D_N = l \sin \theta E_N(t) / n_s \quad (12)$$

$$\begin{aligned} \mathbf{i}_1(t) &= [i_{A1}(t) \quad i_{B1}(t) \quad i_{C1}(t) \quad i_{N1}(t)]^T \\ \mathbf{i}_2(t) &= [i_{A2}(t) \quad i_{B2}(t) \quad i_{C2}(t) \quad i_{N2}(t)]^T \end{aligned}$$

$$\begin{aligned} \mathbf{v}_1(t) &= [v_{A1}(t) \quad v_{B1}(t) \quad v_{C1}(t) \quad v_{N1}(t)]^T \\ \mathbf{v}_2(t) &= [v_{A2}(t) \quad v_{B2}(t) \quad v_{C2}(t) \quad v_{N2}(t)]^T \\ \mathbf{i}_L(t) &= [i_{LA}(t) \quad i_{LB}(t) \quad i_{LC}(t) \quad i_{LN}(t)]^T \end{aligned}$$

$$\mathbf{x}(t) = [\mathbf{v}_1(t)^T \quad \mathbf{v}_2(t)^T \quad \mathbf{i}_L(t)^T \quad E_E(t) \quad E_N(t)]^T$$

#### 4.4 Time Domain Simulation Results

The performance of the broadband transmission line model with GIC has been investigated. A transformer with magnetization characteristics connects a load and the transmission line. This transformer is highlighted in Figure 4.13. At 0.1s, the GMD is



initiated by closing the breaker. At 1.9s, the GMD is terminated. This scenario is selected to assess the time constants associated with GIC buildup. The neutral current of transformer 2 at bus MID2 (high voltage side) is investigated. As a reference, a similar system with constant impedance transmission line models is also simulated and the results are compared. The parameters of the example tests system are shown in Table 4.2.

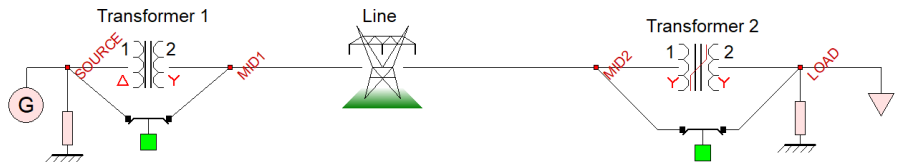


**Figure 4.13 Broadband Transmission Test Case**

**Table 4.2 Parameters for GIC Event Test**

<b>Length of transmission Line</b>	15km
<b>Simulation time step</b>	100 $\mu$ s
<b>Simulation time range</b>	0 ~ $T = 2000ms$ (120 cycles)
<b>GIC equivalent source</b>	120V (8V/km)
<b>Transformer 1</b>	13.8kV/115kV (bus SOURCE to bus MID1)
<b>Transformer 2</b>	115kV/13.8kV, modeled with a non-linear magnetizing inductor (bus MID2 to bus LOAD)
<b>Load</b>	10MW 6MVar (power factor 0.86)

Figure 4.14 to Figure 4.16 show the resulting waveforms at different time scales. In the graph, the three-phase current at the high voltage side for a transformer is presented. The neutral current and its DC component transformer 2 are also plotted. The waveform with “ref” denotes the corresponding data collected in the reference test system, i.e., the system with constant impedance transmission line.

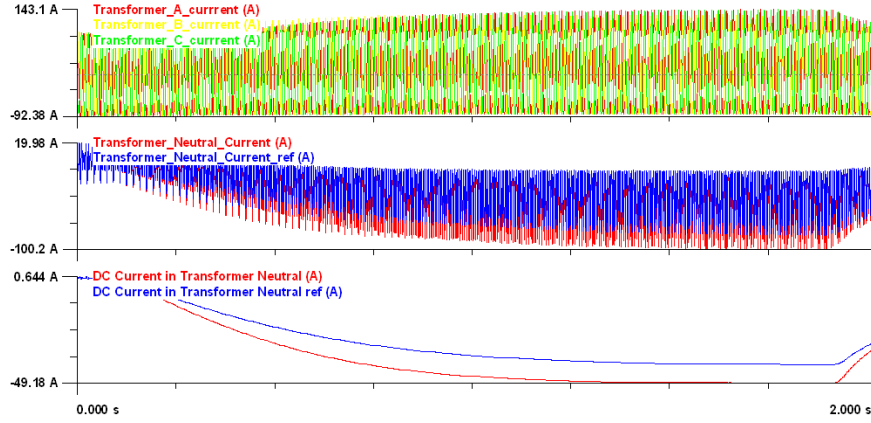


**Figure 4.14 Overall Simulation Results**

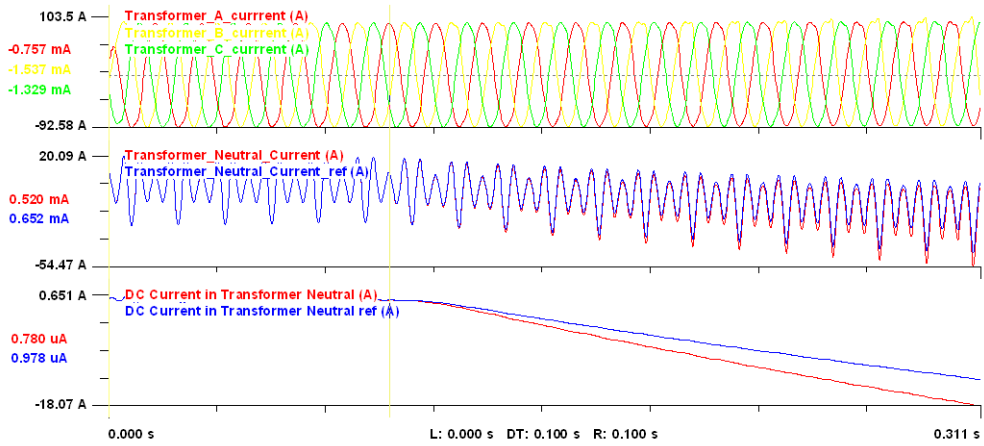


**Figure 4.15 Zoomed-In View at the Beginning of GMD Event (at 0.1s)**

From the results in figures, we can observe that the difference between conventional models and the broadband transmission line models is substantial. The impact of GIC is larger when the transmission line is modeled with the broadband model. The measurement corresponds to the value at the time of the left cursor. When considering the neutral current of transformer 2 at bus MID2 (high voltage side), the ratio between the test model and reference is  $49.18/40.60 \approx 1.21$ , so the relative difference is 20%. In other words, in a steady state, there is 20% more DC current flowing in the

neutral of the system if the frequency-dependent model replaces the constant impedance model. The constant impedance model underestimates the impact of GIC.

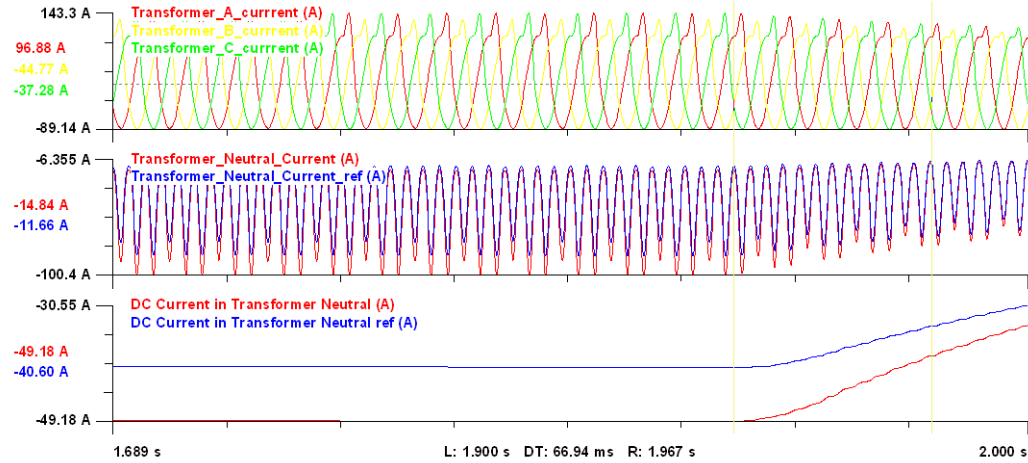


**Figure 4.16 Zoomed-In View at the Ending of GMD Event (at 1.9s)**

## 4.5 Conclusions

In this chapter, the impedance of the low-frequency broadband model is compared with the analytical result. The result shows that the difference between the proposed model and the accurate value is minimal in the investigated frequency range, which indicates the suitability to GIC related study. Numerical results compare the performance of the proposed model and the constant impedance model, showing that the constant impedance model may underestimate the value of GIC.

## **CHAPTER 5.     TRANSFORMER MODELS WITH DETAILED MAGNETIC CIRCUITS**

During a GMD event, the role of large transformers is more concerning among the high voltage affected equipment. Transformers are large investments and are critical components of the power system for generation, transmission, and distribution. In addition, transformers are usually the source of abnormality[7], and the configurations of transformers [32] also determine the vulnerability of the transmission system. When geomagnetic disturbances occur, a DC excitation will be applied to the transformer, leading to severe half-cycle saturation[14]. The resulting DC component in flux usually brings transformers working under abnormal states. Possible outcomes include reactive power consumption increase; magnetizing current growth and distortion; temperature rise in tie plates, tank walls, and windings [34]–[36], [61]. In [39], the authors point out the GSU transformers in GIC vulnerable areas are more likely to fail than those in other areas. To alleviate the GIC impact and protect transformers, many researchers have conducted experiments on transformers with GIC. Test results on small-scale transformer models with different iron core structures are reported in [42]. They found that single-phase three-legged cores were most susceptible among different configurations. Reference [43] tests a 30kVA distribution transformer, reports the magnitude of the excitation current rises to 30 times the normal value. FEM method is used in [44] to assess the susceptibility of transformers with different transformer core designs, while [34] uses magnetic circuits to analyze different core structures. Paper [17] claims that during saturation, the tank is a major path for flux, and a magnetic model with the tank is

needed. Authors in [45] find the existence of air path inductance in five-leg transformer model will affect the result significantly.

The objective of this chapter is to compare the performances of transformers with different configurations during GMD events, especially the transient dynamics. To achieve this, accurate time domain models capturing the electrical and magnetic characteristics for transformers are needed. In this chapter, we develop time domain models of transformers with two windings and three windings. In addition, two different types of magnetic cores are modeled with detailed magnetic circuit models, including three-phase core type transformer and transformer bank with three single-phase transformers. A series of comparisons is conducted to analyze the transients of these transformers during GMD events. This chapter is organized as follows. Section 1 introduces the time domain modeling method for transformers. Section 2 presents the simulation result and analysis. Conclusions are presented in Section 3.

## 5.1 Time Domain Modeling of Transformers

During GMD events, the iron core structure is essential for the exact modeling of the transformer. For instance, when three-phase windings are wound on the same magnetic core, three-phase fluxes interact with each other. During normal operation, the fluxes are practically balanced, and the magnitude of flux is below saturation levels under most circumstances. By contrast, magnetic fluxes are not perfectly balanced when there are DC voltages applied to the transformer, such as GMD disturbances. These zero sequence components may saturate the iron core. In this case, air paths from the core to the tank and the tank material may become part of the magnetic circuit. Therefore, a magnetic circuit model considering the flux path of three-phase winding, air and tank wall is needed for accurate simulation during GIC. To fully describe the magnetization characteristics, the detailed magnetic circuit models of the transformer iron cores are formulated. These magnetic circuit models achieve a good balance between accuracy and computation burden for time domain simulation.

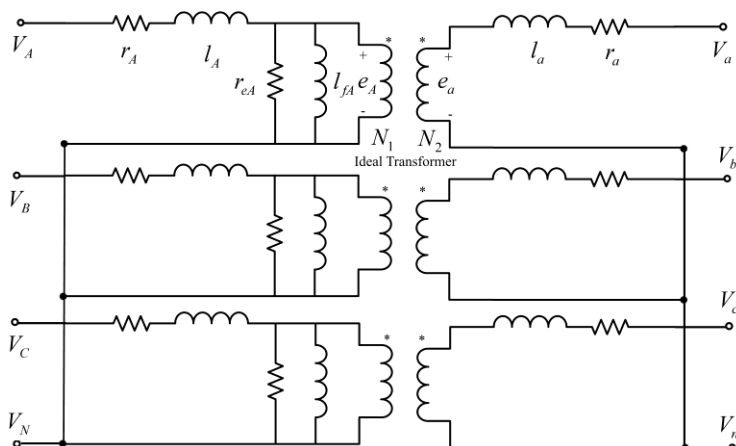


**Figure 5.1 Two Winding Y-Y Transformer Electric Circuit Model**

**Table 5.1 Symbols Used in Magnetic Circuit**

<i>Symbols</i>	<i>Explanation</i>
$\phi_A, \phi_B, \phi_C$	flux through phase limb
$\phi_{AB}, \phi_{CB}$	flux through yoke
$\phi_{OA}, \phi_{OB}, \phi_{OC}$	leakage flux in the air
$\phi_{TA}, \phi_{TB}, \phi_{TC}$	the flux between winding and tank
$\phi_T$	flux through tank
$R_{OA}, R_{OB}, R_{OC},$ $R_{TA}, R_{TB}, R_{TC}, R_T$	constant reluctance for air and tank
$R_{LA}, R_{LB}, R_{LC},$ $R_{LAI}, R_{LBI}, R_{LCI}, R_{AB}, R_{CB}$	nonlinear reluctance for limbs and yokes
$F_A, F_B, F_C$	the magnetomotive force produced by the current in phase windings
$F_T$	the magnetomotive force produced by the equivalent current in the tank

To fully describe the magnetization characteristics, the detailed magnetic circuit model of the transformer is formulated. Figure 5.1 shows the equivalent electrical circuit for a three-phase Y-Y connected transformer. It consists of three identical single-phase circuits. All the variables in phase B and phase C have similar names as phase A. For example,  $l_A, l_B, l_C$  are leakage inductance in the primary side winding.  $r_{eA}, r_{eB}, r_{eC}$  are the resistance of iron loss.  $l_{fA}, l_{fB}, l_{fC}$  are the nonlinear magnetizing inductances. The nonlinear inductances are described in terms of the relationship between magnetic flux, induced voltage  $e_A$ , and magnetizing current  $i_{fA}$ . Figure 5.2 depicts the iron core structure and the winding configuration of a three-phase core form transformer. The magnetic circuit model for the transformer is shown in Figure 5.3. The solid lines represent the flux path in the iron core, which has lower reluctance if not saturated; while the dotted lines represent the path in air and tank, which have much larger reluctance. Under normal

circumstances, magnetic flux is concentrated in the iron core, so the equivalent reluctance is relatively low. By contrast, during GMD events, the air and tank become major paths for the flux, and the reluctance increases dramatically. Table 5.1 defines the components of this model.

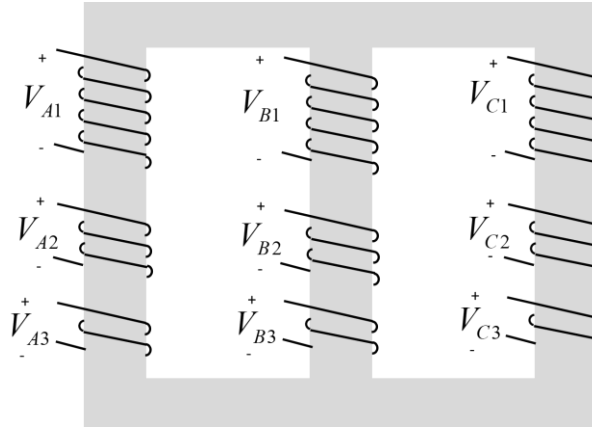


**Figure 5.2 Iron Core Structure of a Three Winding Core Form Transformer**

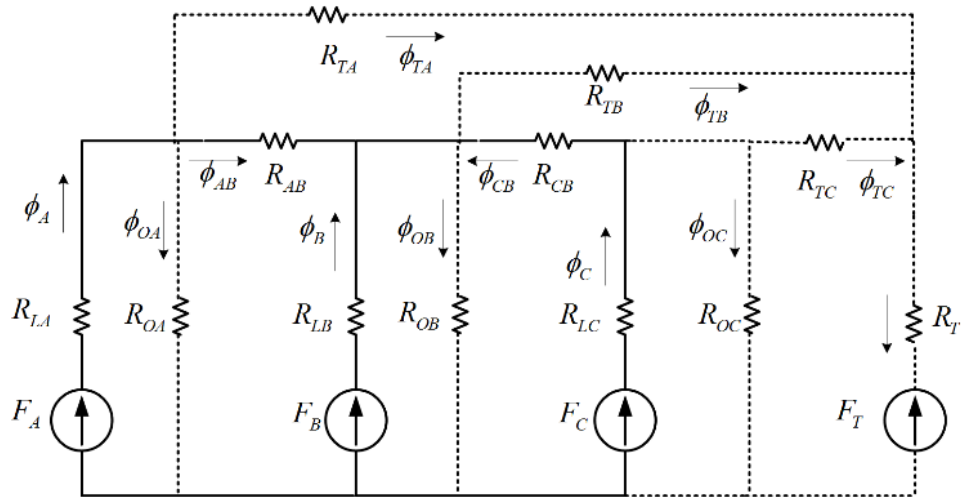


**Figure 5.3 Magnetic Circuit for Three-Phase Core Form Transformer**

Transformer abnormal performance during GIC is determined by the nonlinear relationship between magnetic flux and magnetizing current, or from a materials perspective, a nonlinear relationship between magnetic flux density (B) and magnetic



field strength (H) of the iron core. When there is a DC flow in the transformer winding, the magnetic flux in the transformer is offset from the sinusoidal characteristics. This offset forces the transformer to work in the nonlinear region for part of a half cycle, resulting in spikes in magnetizing current and distortion of the phase current. There are different ways to capture this nonlinear characteristic. A common practice is to use a piecewise linear function to describe the transformer magnetizing reluctance, dividing it into either unsaturated or saturated status. The B-H curve is depicted in Figure 5.4(a). Another property of iron core—hysteresis—can be added to this model but it is not discussed here. In this study, a polynomial function[62] of high-degree in Equation (13), is used to describe the inductance. Where  $\phi_x$  is the flux through a specific part in the iron core,  $\phi_0$  is the base value of flux.  $i_0$  is the base value of magnetizing current.  $R_x$  is the reluctance of the corresponding part.  $n$  is the degree of the function. The nonlinear relationship with specific parameters is depicted in Figure 5.4(b). For typical power transformer core material, the exponent  $n$  is in the order of 12. Compared with a piecewise linear function, a polynomial function is differentiable everywhere, which eases the computation.

$$R_x = \frac{i_0}{\phi_0} \left( \frac{\phi_x}{\phi_0} \right)^n \quad (13)$$

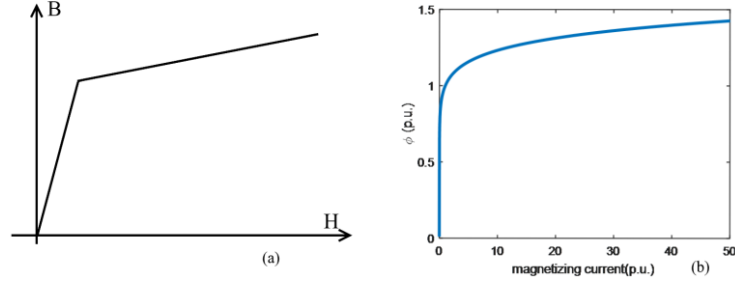


**Figure 5.4 (a) Piece-wise linear B-H curve (b) Nonlinear Reluctance Model**

To integrate the magnetic circuit and the electrical circuit, the following equations are used.  $k=A, B, C$ , representing phase A, phase B, and phase C, and  $r_T$  is the equivalent resistance for the tank.

$$\begin{aligned}
 0 &= e_k - N_1 \frac{d\phi_k}{dt} & 0 &= -e_T + \frac{d\phi_{TA}}{dt} + \frac{d\phi_{TB}}{dt} + \frac{d\phi_{TC}}{dt} \\
 0 &= N_1 i_{fk} - F_k & , 0 &= -e_T + r_T i_T \\
 & & 0 &= -F_T + i_T
 \end{aligned} \tag{14}$$

$\underbrace{\hspace{10em}}_{\text{iron core}}$ 
 $\underbrace{\hspace{10em}}_{\text{tank}}$

Similarly, magnetic circuit models are proposed for single-phase transformers banks. In this case, each single-phase transformer possesses an individual iron core, which is depicted in Figure 5.5. Three identical single-phase magnetic circuits form the three-phase model, while there is no interference between any two phases in the magnetic circuit. The symbols used in magnetic circuits are listed in Table 5.1.

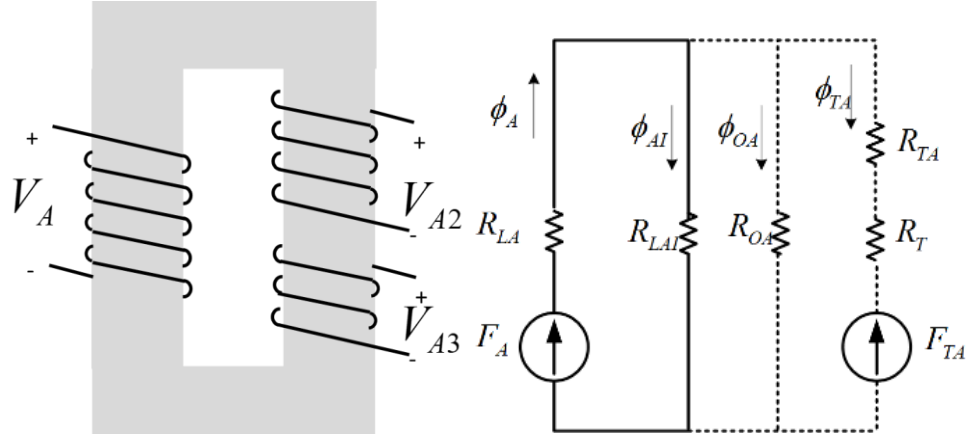


**Figure 5.5 Single-Phase Transformer Model**  
(left) Iron Core Structure; (right) Magnetic Circuit

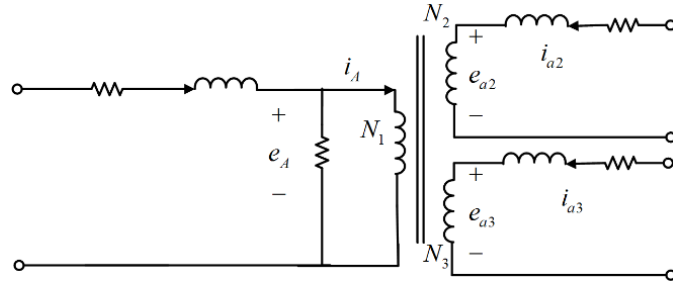


**Figure 5.6 Three Winding Single-Phase Transformer Electric Circuit**

The electrical circuit for transformer models remains the same regardless of core structures. A three winding single-phase transformer circuit is shown in Figure 5.6. To formulate a three-phase transformer circuit, we connect three identical replicas of single-phase circuits together. The bridge between the magnetic circuit and the electric circuit is the relationship between magnetizing current and flux, which is shown in (15).

$$F_A = N_1 i_A + N_2 i_{a2} + N_3 i_{a3}$$

$$e_A = \frac{d\phi_A}{dt} \quad (15)$$

### 5.1.1 Parameter Calculation

For each type of transformer, we determine a set of parameters to achieve similar performance under the normal operating condition with others. For instance, the power rating, the number of winding turns, and the per-unit electrical characteristics are the same for each model. Therefore, the leakage inductance, winding resistance and core conductance are the same for corresponding winding. For three winding transformers, the load connected to tertiary terminals is much less than that at the secondary terminal, so their performances are comparable to those of two winding transformers.

The parameters in the magnetic circuit are also identical for different models, such as air reluctance  $R_{OA}$  and tank reluctance  $R_T$ . The iron core reluctance is not constant: when flux increases, the iron core is saturated, and reluctance will significantly increase. We use the high order polynomial in (13) to describe the nonlinearity of iron core. For all iron core reluctance, the same  $\phi_0, i_0, n$  are used. In other word,  $x = LA, AB, \dots$

## 5.2 Numerical Results

In this section, the aforementioned transformer models are examined in numerical simulation of power system test cases and the performances are compared.

### 5.2.1 Test Case Description

We design an illustrative system with a generator, a step-up transformer, a transmission line and loads. Different types of transformer models are installed at the same location, one at a time. The overview of the system is shown in Figure 5.7. The transformer models under investigation are highlighted in the figure. Four different

transformers are considered, and their parameters are listed in Table 5.2. In practice, there are multiple three-phase shared iron core structures, but this study concentrates on the core form structure.

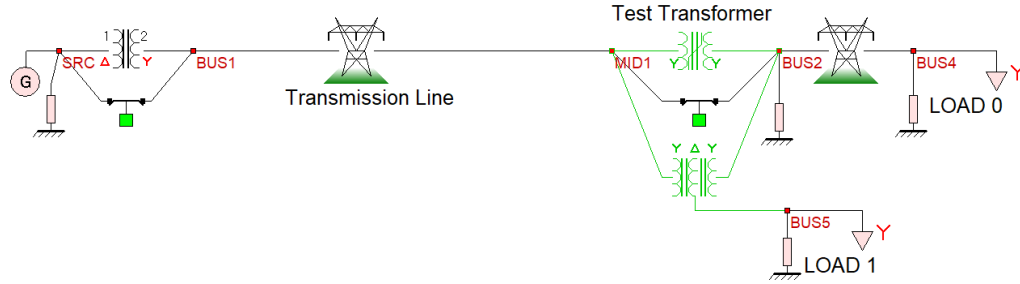


**Figure 5.7 Test Case Overview**

**Table 5.2 Test Case Parameters**

Transmission Line	Length :40km
Transformer 1	Two winding (core form, shared iron core): 115kV/ 25kV, Y-Y
Transformer 2	Two winding banks (individual iron cores): 115kV/ 25kV, Y-Y
Transformer 3	Three winding (core form, shared iron core): 115kV/ 25kV/13.8kV Y-Y-Δ
Transformer 4	Three winding banks (individual iron cores): 115kV/ 25kV/13.8kV, Y-Y-Δ
Load 0	10MW+5MVar
Load 1	1kW+0.5kVar
GMD Event	5V/km, from $t = 5s$ to $t = 40s$

### 5.2.2 Performance during Normal Operation

In this section, we compare the magnetizing current of the transformers. When secondary winding and tertiary winding are connected to zero loads, the primary winding

current is the magnetizing current to formulate the flux inside the iron core. Figure 5.8 shows three-phase currents in the primary winding with zero loads at other terminals. We can observe that, in shared core transformers, three-phase currents are not balanced, because the path for the flux of phase B is different from those of phase A and phase C. If the reluctances of iron core sections are the same constant, then the ratio of equivalent reluctances between phases is  $R_A:R_B:R_C = 2.5:2:2.5$ . Therefore, phase B needs less magnetizing current to generate flux.

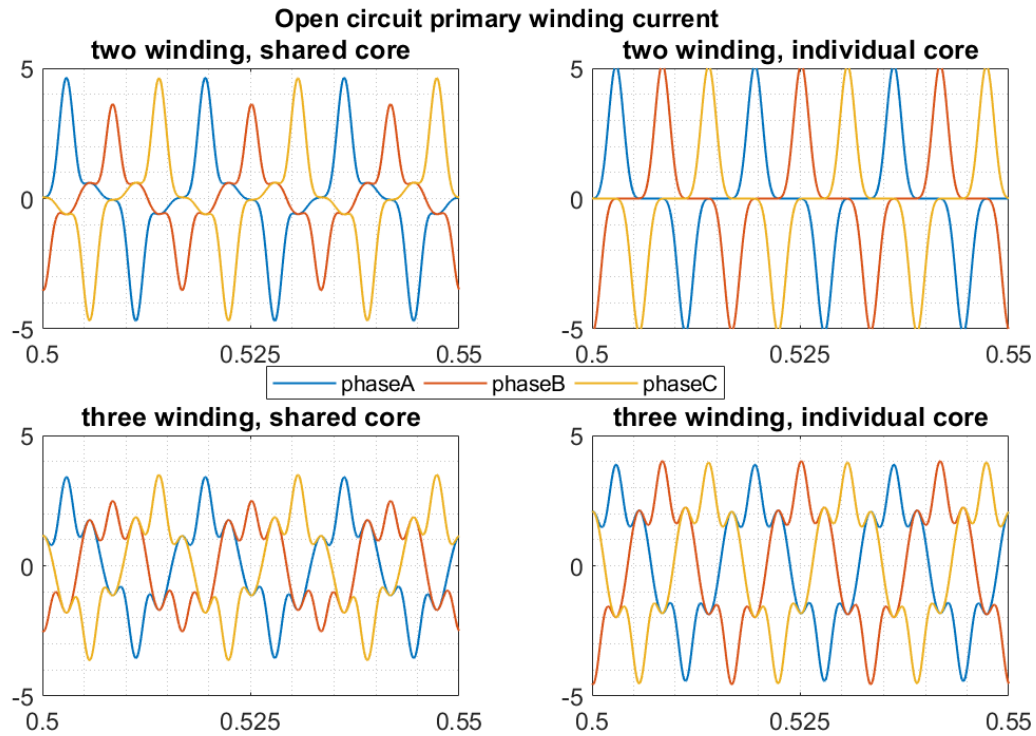


**Figure 5.8 Comparison of Primary Current with Zero Load**

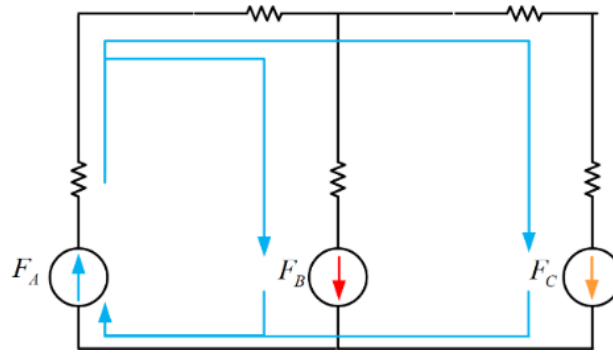


**Figure 5.9 Flux Path for Phase A**

In addition, the maximum values of phase current in shared core transformer are low than those in the corresponding individual core, due to the interaction between three-phase current in the shared core. For example, when phase A reaches the positive maximum, phase B and phase C are at saddle points in the negative direction. So the flux is formulated by the combination of magnetomotive force generated from all three phases current. An illustrative graph is depicted in Figure 5.9. Furthermore, the maximum value of current in three winding transformers is low than that in the corresponding two winding. This difference originates from the induced third-order harmonic current in the tertiary winding, which is shown in Figure 5.10. This current also contributes to the flux, and the peaks of tertiary winding current are aligned with the peaks in the primary winding current. The direction of tertiary current is the same with only one phase and is in the opposite of the remaining two phases. The flux in one phase is boosted while the flux in the other two phases is reduced. As a result, one phase current increases, while the other two decrease.

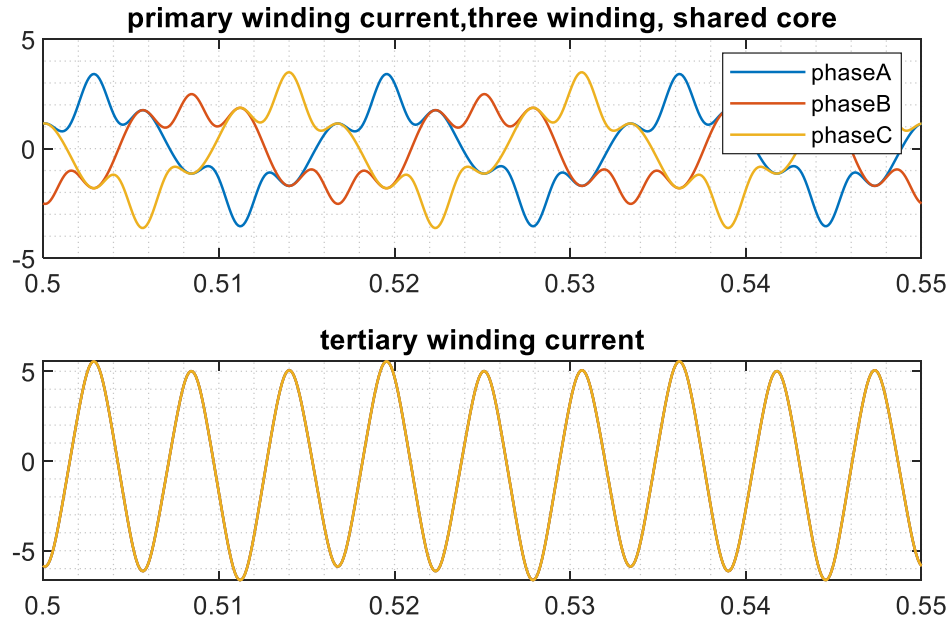


**Figure 5.10 Third Order Harmonic in Tertiary Winding Current**

### 5.2.3 Performance during GMD events

In this section, the performance of the transformers during GMD events is compared. The load is shown in Figure 5.7 0are connected to the transformer. The primary winding phase A current during normal operation is compared in Figure 5.11. The values from different transformers are approximately the same, which means transformers are operating at similar conditions. At  $t = 5s$ , the GMD event starts. Figure 5.12 0shows that the DC component in phase current starts to accumulate. The steady state during GMD events is shown in Figure 5.13. It is obvious that there are distortions in the waveforms, especially for the transformer banks. These distortions reflect the sensitivity of transformers to DC excitation during GMD events. In other words, transformer banks are more saturated than three-phase core form transformers.



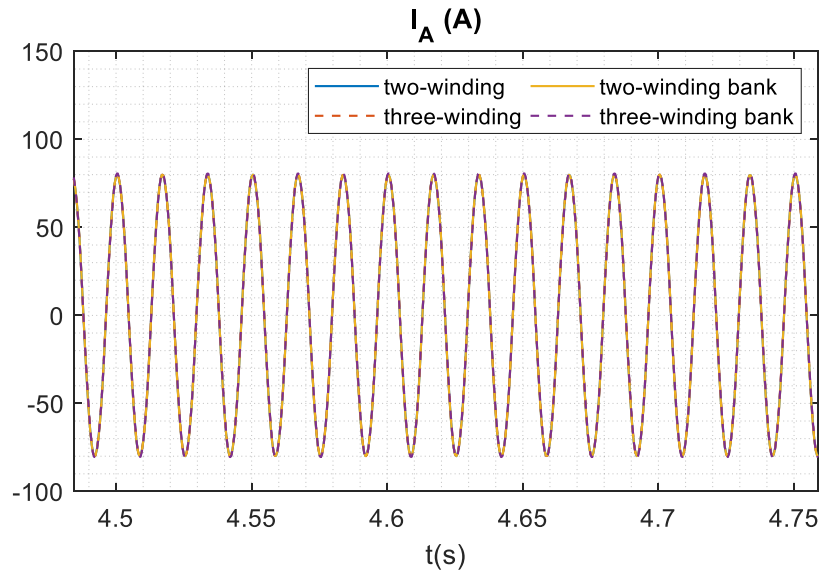


**Figure 5.11 Primary Winding Phase A Current before the GMD**

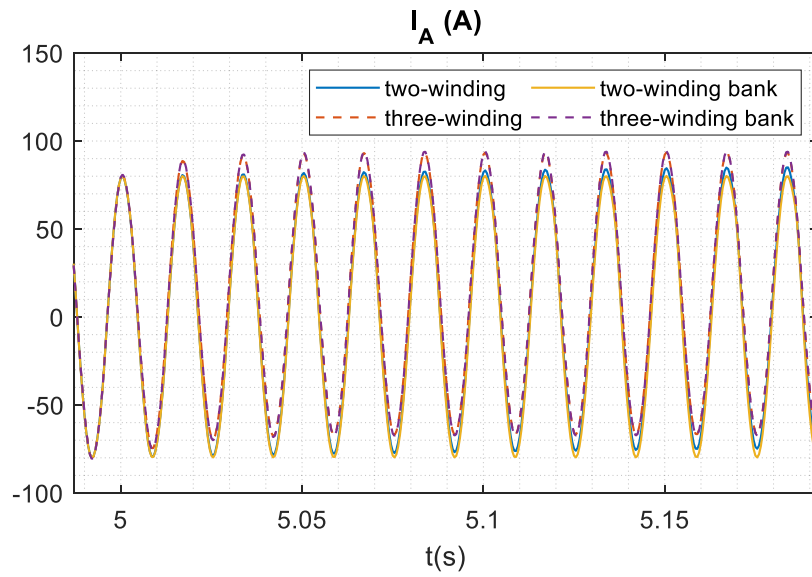


**Figure 5.12 Phase A Current after the Onset of the GMD**

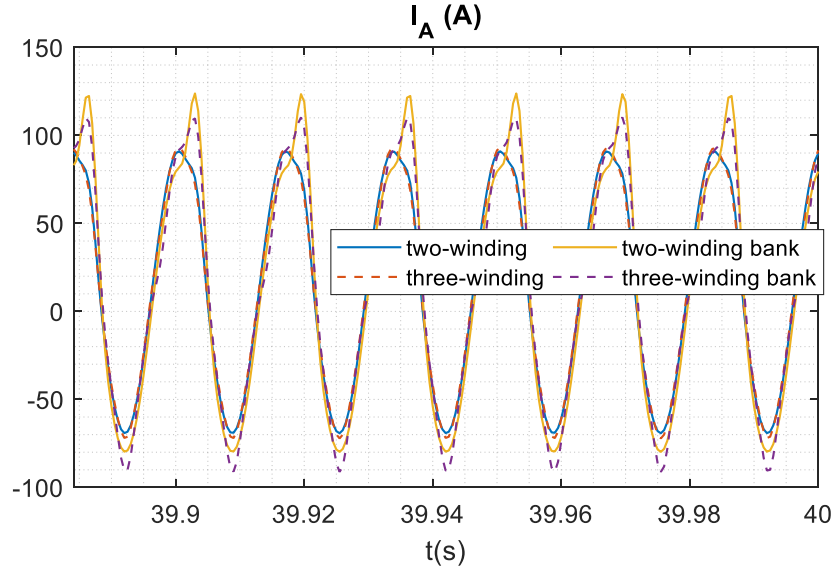


**Figure 5.13 Primary Winding Phase A Current during the GMD**

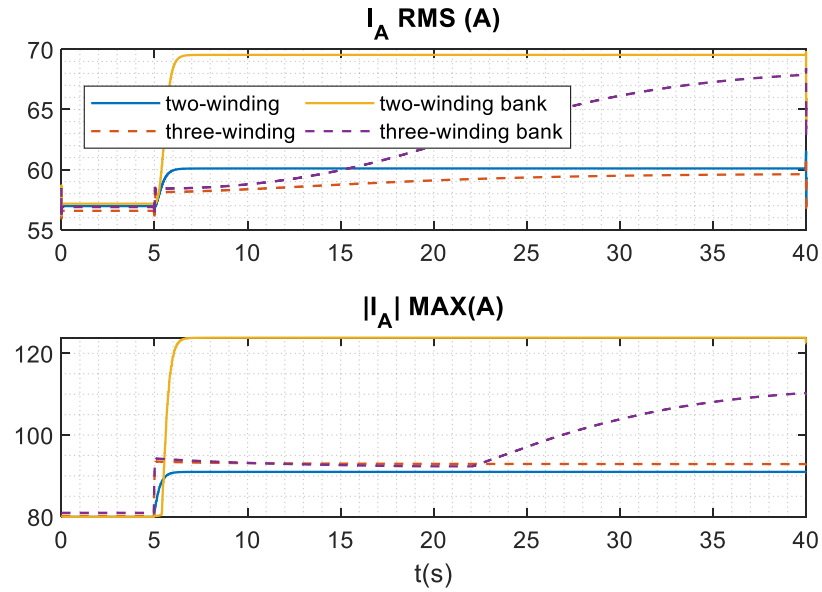


**Figure 5.14 RMS Value and Maximum Value of Primary Winding Phase A Current**

The RMS value and maximum value of phase A current are plotted in Figure 5.14. It is clear that the transformers with shared core have lower magnetizing current than the transformer bank with individual cores. When three-phase windings share the same 3-leg iron core, there is no path for DC flux in the iron core. As a result, DC flux

needs to go through air and tank, which significantly increases the equivalent reluctance. An illustrative figure showing the path for DC flux is shown in Figure 5.15. By contrast, for transformer with individual cores for each phase winding, a large portion of DC flux still flows through the iron core. Therefore, the equivalent DC magnetizing inductance is larger in the individual core transformer. So more DC flux will accumulate, and the iron core gets more saturated. The comparison of flux in air and tank path is shown in Figure 5.16. The increase in magnetizing current leads to a substantial increase in reactive power, which is depicted in Figure 5.17. The active power and reactive power of fundamentals are compared during the GMD. The rise in active power is minimal while the reactive power increases dramatically, especially for the transformers with individual cores. This observation is consistent with the transients of phase currents. Due to the significant increase in magnetizing current, the reactive power consumption increases by factor 7 in transformers banks.

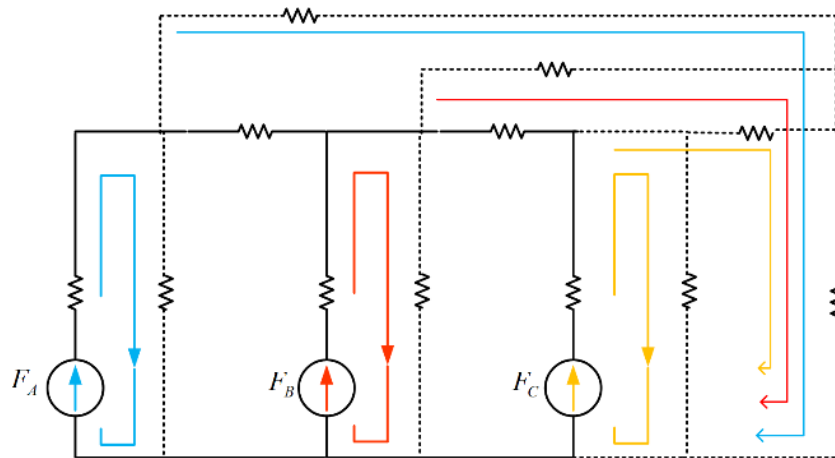


**Figure 5.15 Path for DC Flux in Shared Core**

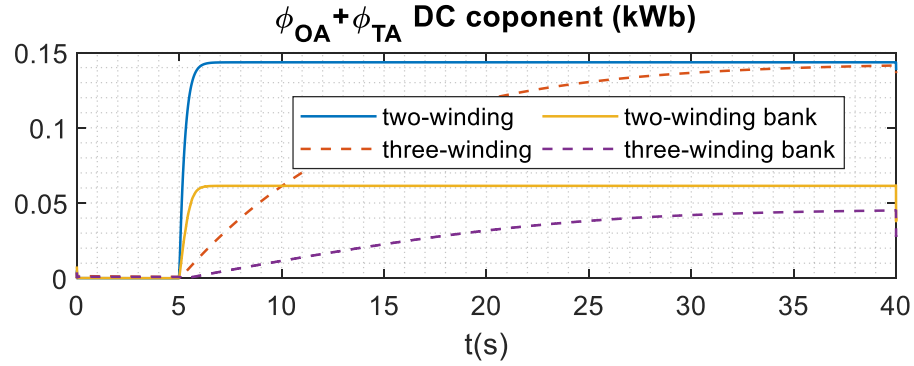


**Figure 5.16 DC Component of Flux in Air and Tank Path**

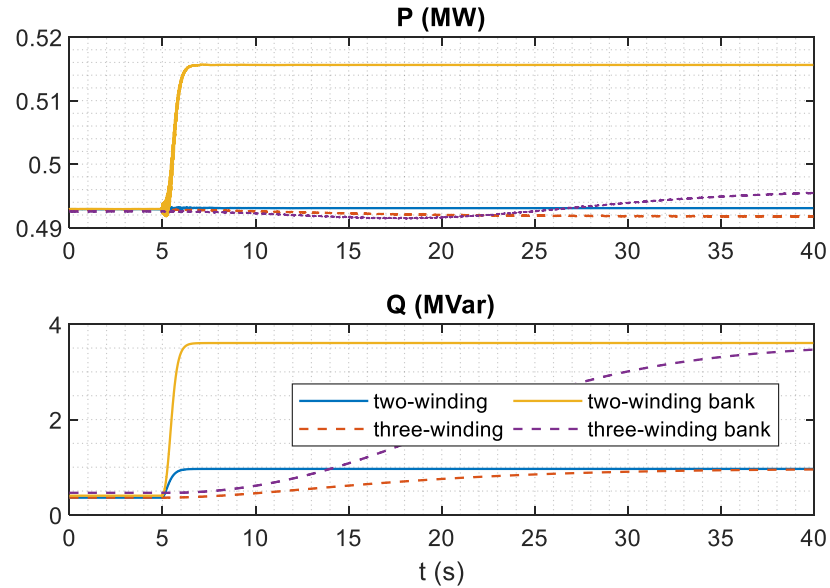


**Figure 5.17 Active Power and Reactive Power Consumption for Fundamental**

Another difference is that the time constants during the onset of GMD in three winding transformers are much longer than those of two winding transformers. In other words, the time needs to accumulate flux and the time for magnetizing current increasing to stable value is longer in three winding transformers. When the tertiary winding connected in delta, there is a path for DC current. Therefore, the tertiary winding acts as a damping winding for DC excitation. In this damping winding, a DC current is induced

after the onset of GMD. This current will work against the current in the primary winding. As a result, the increase of DC flux will slow down. However, the flux will finally increase to a similar level as no tertiary. The dc flux and induced voltages are shown in Figure 5.18. This observation can be utilized to develop a mitigation method to reduce saturation, which is described in the next section. Meanwhile, there is no substantial difference between the DC component in currents for these transformers. Figure 5.19 illustrates that during the GMD event, the steady state value of DC phase currents and DC neutral currents are almost the same.

The transients for harmonic components are also studied for these transformers. In Figure 5.20, the harmonics components in phase A current are normalized with respect to the fundamentals. The iron core saturation due to DC flux leads to the increase of these harmonics. Therefore, the harmonics transients are consistent with the rise of the DC flux in general, which is shown in Figure 5.18. Meanwhile, for transformers with tertiary windings, there is no obvious variation of the third-order harmonic in primary winding phase current during GMD events. This is because the tertiary winding is in delta connection, which is a path for third-order harmonic, which is illustrated in Figure 5.10.

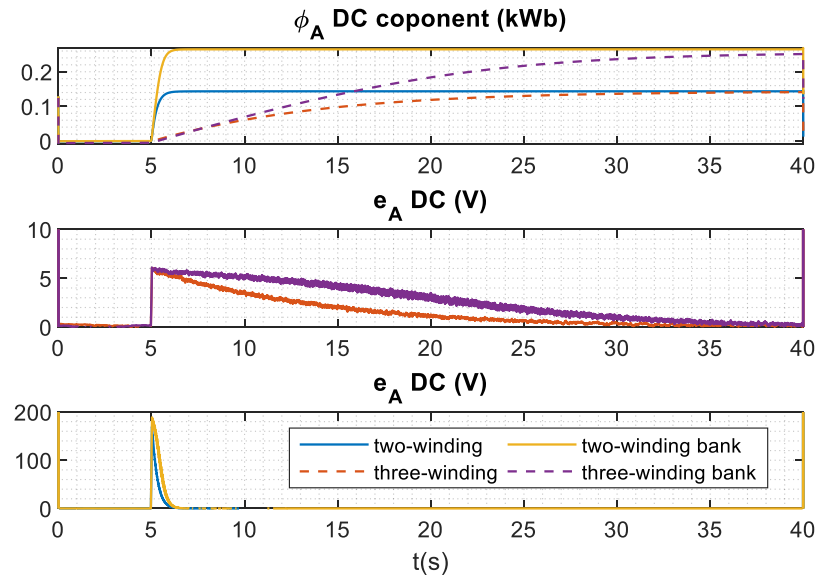


**Figure 5.18 DC Component in Flux and Induced Voltage**

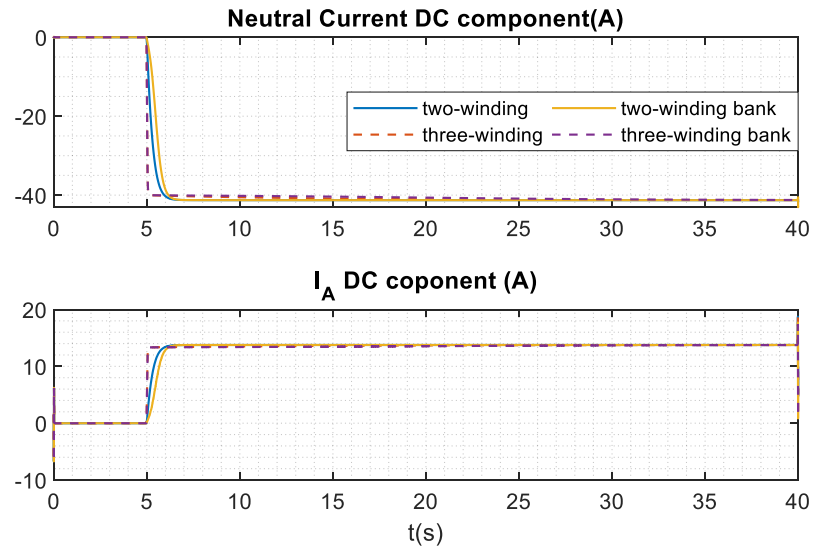


**Figure 5.19 DC Component in Phase and Neutral Current**

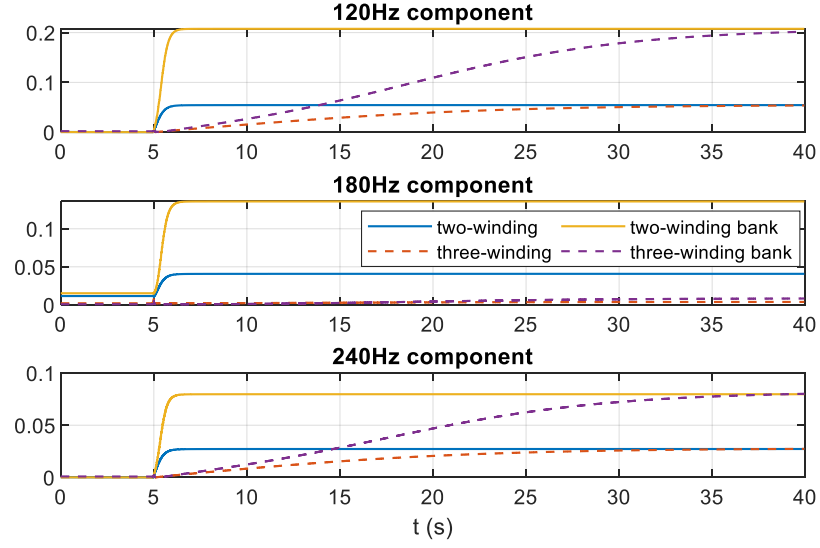


**Figure 5.20 Normalized Harmonics Components in Primary winding Phase Current**

### 5.3 A Mitigation Method

A mitigation method can be developed from the previous observation. The induced current in the tertiary winding slows down the accumulation of DC flux in the iron core. To preserve the induced current in the tertiary winding, we can manually provide such DC current. We can disconnect the tertiary winding at a terminal and create an opening in the delta connection. Then a DC current source is connected between the opening, which is shown in Figure 5.21. The magnitude of the current  $I_s$  is determined by the turn ratio of the primary winding and tertiary winding (16).

$$N_1 I_{1dc} = N_3 I_s \quad (16)$$

where  $I_{1dc}$  is the DC component in primary winding phase current,  $N_1$  and  $N_3$  is the number of turns for primary winding and tertiary winding correspondingly. As a result, the DC component in primary winding current still exists, but the iron core is not saturated, and we avoid the distortion in the magnetizing current. This method is

examined with the same three-winding transformer bank used in the previous section. The tertiary winding is disconnected from the load and a DC current source with the magnitude  $I_S$  is connected to the opening. The simulation result for the mitigation method is shown in Figure 5.22. Compared with the transformer without mitigation, the distortion of magnetizing current during GMD is substantially reduced and the RMS value of magnetizing current decreases.

In practice, the implementation of this mitigation method can be more flexible. Under normal operation, the delta connection remains closed, the auxiliary DC current source is bypassed, and the DC component in primary current is monitored. When GMD activity starts, the DC component in the primary current will rise. Then the auxiliary DC current source is switched on and the delta connection becomes open. Since both the dynamic of GIC is slow enough, we have time to detect and switch between two topologies – open/closed delta.

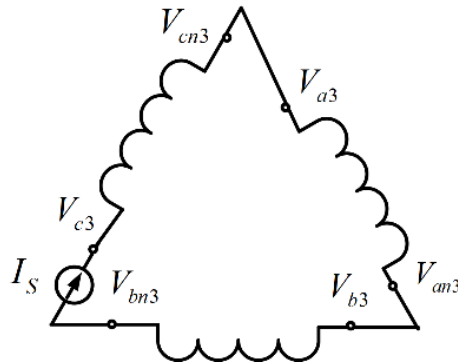


**Figure 5.21 Tertiary Winding Connection for Mitigation Method**



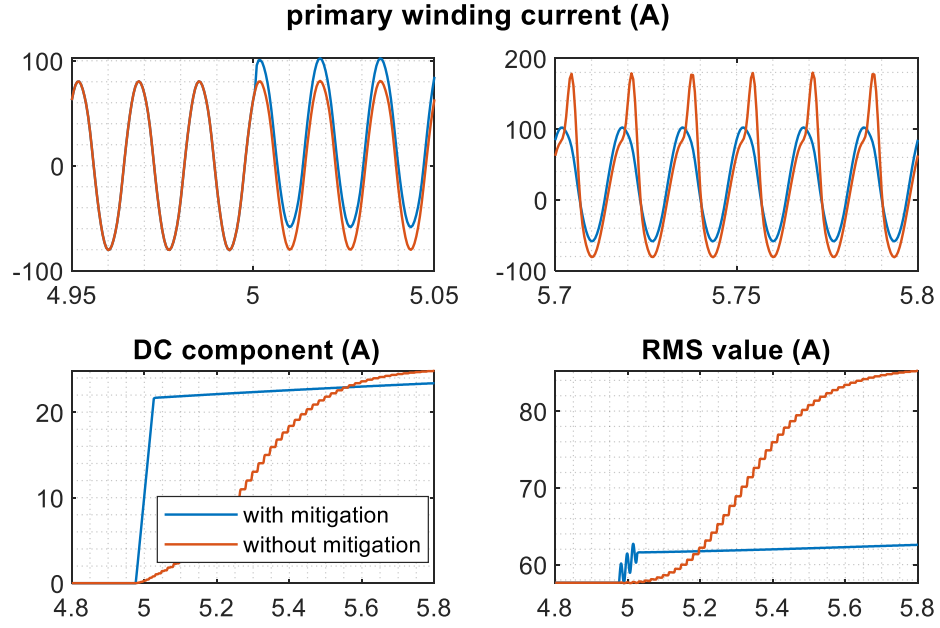


**Figure 5.22 Examination of Mitigation Method**

#### 5.4 Conclusions

To analyze the dynamics of transformers during GMD events, this chapter proposed time domain models for four different configurations of transformers. The magnetic characteristics of iron cores are described with detailed magnetic circuits. The transient performance of these transformers is analyzed and compared via numerical simulation. The results show that there exists a large difference between transformers during GMD events. Single-phase transformers banks with individual iron cores have a much larger distortion in magnetization current, compared with transformers with a three-phase shared core. A mitigation method to reduce saturation and harmonics is proposed and examined. The distortion of magnetizing current in transformers during GMD is substantially reduced, which enables more stable operation of the grid.

## **CHAPTER 6. GIC TRANSIENTS IN POWER GRIDS**

In this chapter, we combine the time domain models developed in previous chapters and construct the grid-level model and generate several test cases. All the transmission lines and transformers are modeled considering the impact of GIC. Unlike the conventional GIC analysis tools with DC simplification, these test cases enable the investigation of the transients of GIC during GMD events through time domain simulation. The interaction of DC components with power devices and the propagation of harmonics are revealed. In other words, the dynamics of DC currents at different locations in the grid are monitored during the simulation. In addition to the steady state value of GIC, the results will also reveal the accumulation of GIC in terms of time.

### **6.1 Directional Sensitivity in GIC Transients**

Due to the topology of the power grid, the direction of GMD will affect the magnitude of GIC observed at neutrals in substations. The directional sensitivity analysis reports the vulnerability of the grid at different GMD events. For instance, the GIC at a specific substation may reach maximum when the direction of the geoelectric field is 45 degrees. The conventional analysis utilizes a simplified DC network, which outputs results valid for the steady state analysis. However, due to the difference in time constants at different locations, the transients of GIC may vary significantly. This section conducts a set of experiments to investigate the directional sensitivity considering the transients of GIC.

### 6.1.1 Test Case Overview

A grid with 12 substations is used in this test case. Regarding the locations of the substations: the length of a degree of longitude is about 2.8 degrees (approximately 250 km from west to east); the length of a degree of longitude is about 5 degrees (approximately 550 km). Inside the substations, transformers are modeled with magnetic circuits. Between the substations, most of the transmission lines are operating at 500kV, and the remaining are operating at 230 kV or 115 kV. All these transmission lines are represented with a low broadband frequency-dependent line model. More details of the devices in each substation are available in Table 6.1. In Figure 6.2, circuits inside substation RMT are depicted as an example, including the load and transformer.

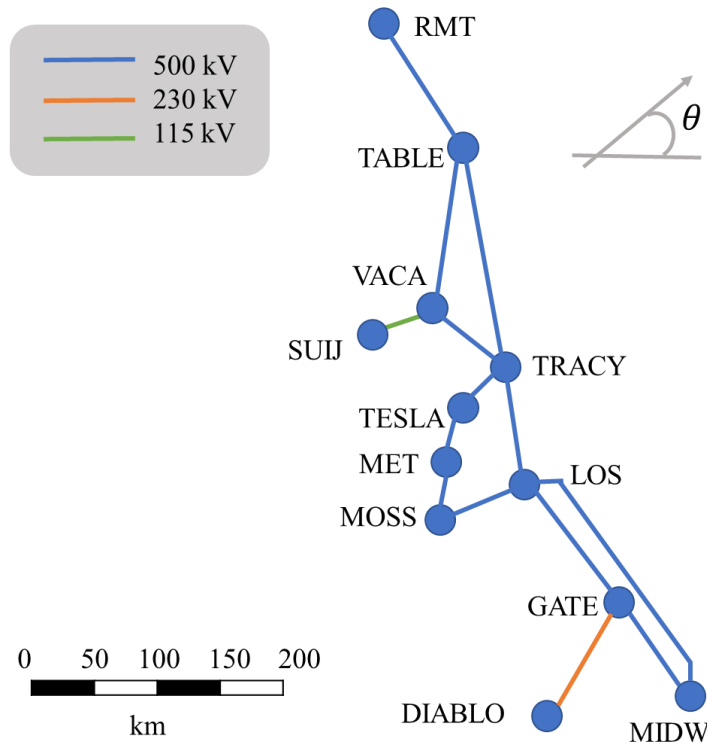


**Figure 6.1 Test System Substations Overview**

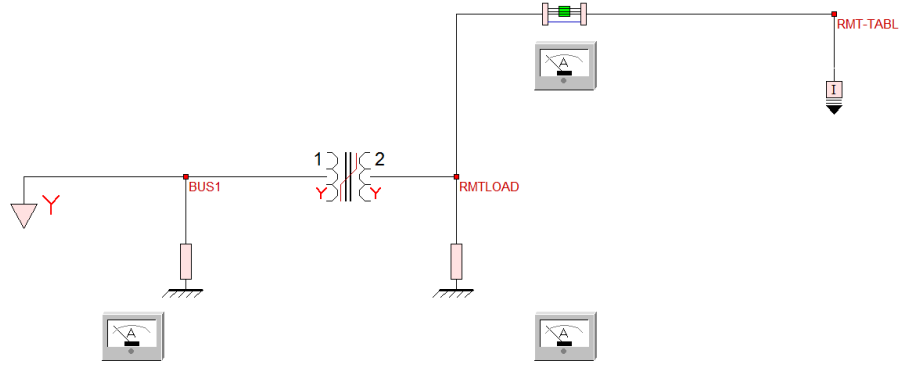


**Figure 6.2 Substation RMT Configuration**

A series of experiments are conducted on this test system. The length of the simulation is 120s with time step  $h = 500\mu s$ . The magnitude of the GMD is 5V/km, the GMD starts at 5s and remains constant until the simulation finished. The direction of the GMD varies from  $0^\circ$  to  $360^\circ$  with a step size of  $15^\circ$ . The direction angle is defined as the difference between GMD direction and the west-east direction, denoted as  $\theta$  in Figure 6.1. The results of a series of experiments will illustrate the directional sensitivity of the system during GMD events. In addition, the transients of the rise of GIC are available in the results.

**Table 6.1 Devices in Test Case Substations**

Substation	Devices
RMT	500kV:230kV Y-Y Transformer 80MW,20MVA <sub>r</sub> Load
TABLE	500kV:230kV Y-Y Transformer 500kV:230kV Y-Y Transformer 3500 MVA Generator 400MW, -100MVA <sub>r</sub> Load 100MVA <sub>r</sub> Inductor Bank
VACA	500kV:230kV Y-Y Transformer 500kV:230kV Y-Y Transformer 230kV:115kV Y-Y Transformer
SUIJ	230kV:115kV Y-Y Transformer 230kV:115kV Y-Y Transformer 80MW,20MVA <sub>r</sub> Load 80MW,20MVA <sub>r</sub> Load
TESLA	500kV:230kV Y-Y Transformer 500kV:230kV Y-Y Transformer 2000 MVA Generator 10000MW +1000MVA <sub>r</sub> Load
TRACY	500kV:230kV Y-Y Transformer 2000 MVA Generator
MET	500kV:230kV Y-Y Transformer 2000 MVA Generator
MOSS	500kV:230kV Y-Y Transformer 2000 MVA Generator
LOS	500kV:230kV Y-Y Transformer 2000 MVA Generator
GATE	500kV:230kV Y-Y Transformer 500kV:230kV Y-Y Transformer 230kV:115kV Y-Y Transformer 2000 MVA Generator 800MW +200MVA <sub>r</sub> Load 350MW -80MVA <sub>r</sub> Load
DIABLO	230kV:115kV Y-Y Transformer 2000 MVA Generator
MIDW	500kV:230kV Y-Y Transformer 300MW, -100MVA <sub>r</sub> Load 100MVA <sub>r</sub> Inductor Bank

### 6.1.2 Numerical Results

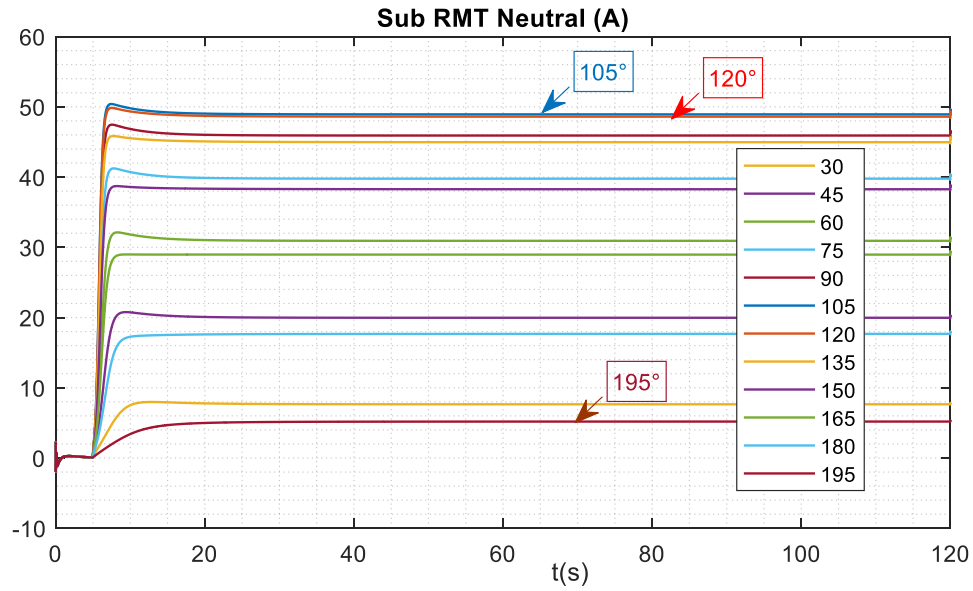


**Figure 6.3 Neutral Currents at Substation RMT**

Once the GMD is introduced to the grid, the DC currents in transmission lines, transformer windings, and neutrals start to rise. Conventional GIC related analyses focus on the steady state value of these DC currents. By contrast, the time domain simulation method can record the dynamics of the DC currents during the onset of GMD. For example, Figure 6.3 depicts the waveform of DC current in substation RMT neutral during different GMD events. In order to make the figure less busy, only a subset of simulation results is shown in the figure. Under all GMD events, the neutral currents will converge to steady state value. It is worth noting that the rise of GIC shows different patterns. Some of them show “overshooting”. This indicates that the neutral may endure a short time higher current threatening the equipment, which is ignored in conventional GIC related study. Meanwhile, the directional sensitivity of the GIC is also apparent in

the figure. When the direction of GMD is between  $105^\circ$  and  $120^\circ$ , the GIC reaches the maximum. When the direction is around  $195^\circ$ , the GIC reaches the minimum.

To further investigate the dynamics of GIC during GMD with different directions, the time domain waveforms are plotted in polar coordinates, which is shown in Figure 6.4 to Figure 6.7. The DC component of neutral current at different time steps is plotted in these figures. For some substations with multiple voltage levels, the neutrals at different voltage levels are monitored separately, such as GATE-500 and GATE-230. For each data point, the angle is the direction of GMD and radius is the magnitude of DC current in neutral. These points are colored according to the time step. Therefore, these graphs present two pieces of valuable information at the same time, the directional sensitivity to the GMD and the dynamic of the GIC. According to the different patterns in these two aspects, the results can be classified into four categories.

- 1) The directional sensitivity does not change significantly in terms of time, and the steady state value of GIC is approximately larger or equal to most points during transients. This case includes Sub RMT, Sub VACA-500, VACA-115, SUIJ MET, MOSS, TRACY, MIDW. In summary, about half of substation neutrals are classified as this group. The dynamics of this group are relatively simple: the GIC gradually increases monotonically (or almost monotonically), and the directional sensitivity remains the same. Therefore, the analysis of the largest possible GIC at these substations is equivalent to the calculation of the steady value of GIC caused by the GMD with direction aligned with the most sensitive direction. In
- 2) The directional sensitivity does not change significantly in terms of time, but the steady state value of GIC is apparently lower than some points during transients.

This case includes TABLE, GATE-500. The dynamics of this group are more complicated: the GIC gradually increases quickly after the introduction of GMD, and decreases gradually after about 1 second; the directional sensitivity remains the same. Therefore, the analysis of the largest possible GIC at these substations is **not** equivalent to the calculation of the steady value of GIC caused by the GMD with direction aligned with the most sensitive direction. Instead, the whole transients of the GIC need to be considered because the steady value is not the largest.

- 3) The directional sensitivity changes significantly in terms of time, and the steady state value of GIC is apparently lower than some points during transients. This case includes TESLA, DIABLO, LOS, GATE-230. The dynamics of this group are the most complicated: the GIC gradually increases quickly after the introduction of GMD, and decreases gradually after about 1 second; the directional sensitivity changes during the meantime. Therefore, the analysis of the largest possible GIC at these substations requires the consideration of the whole transients and all directions of GMD. In other words, if the analysis only considers the steady state value of GIC derived from a specific direction of GMD, the result is a significant underestimate of possible GIC.
- 4) The neutral is not affected by GMD and no substantial GIC is observed: VACA-230. There is no transmission line directly connecting to this bus, so the neutral current will not have the DC component during GMD.



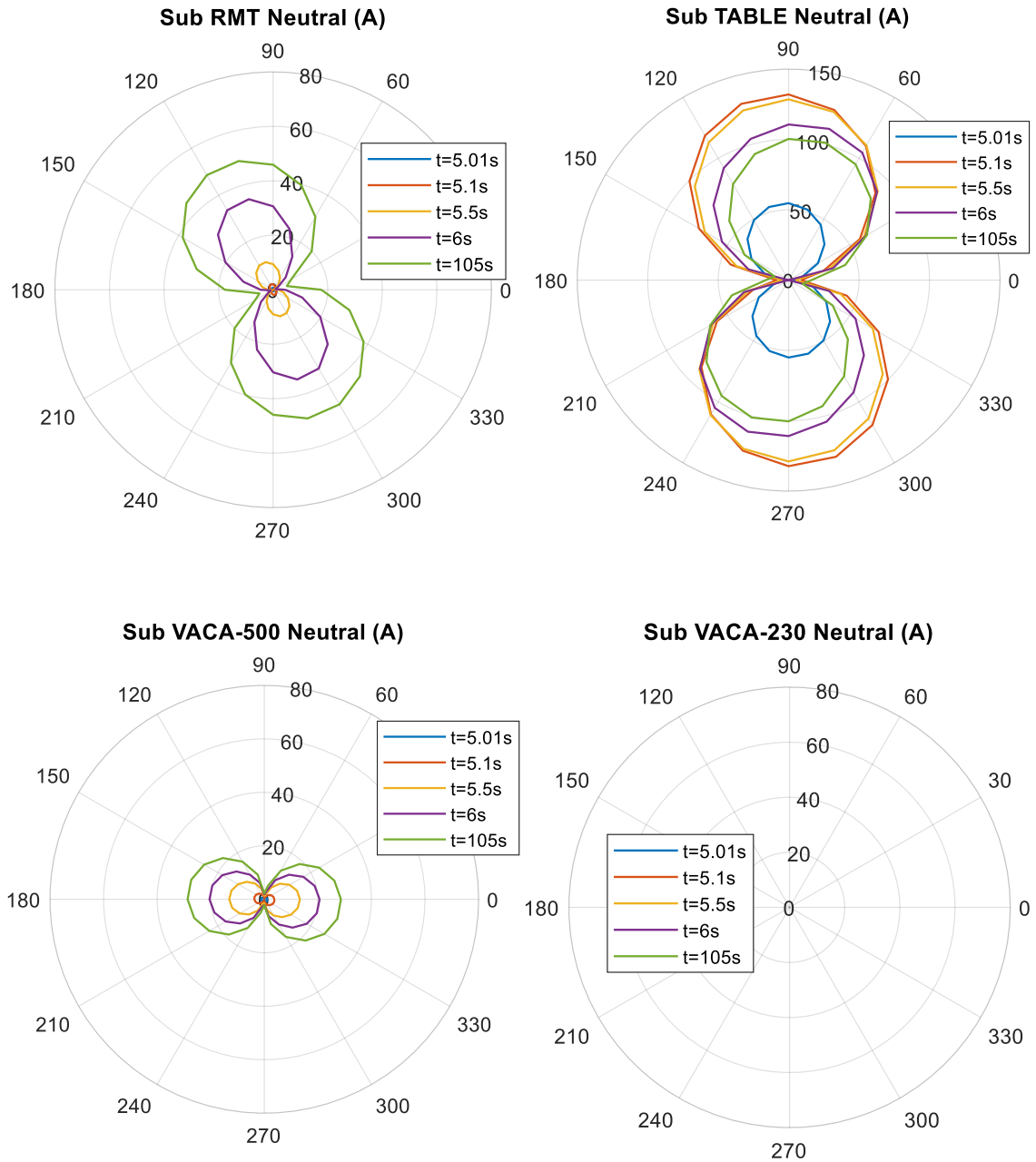


**Figure 6.4 Neutral Current at Substation Groundings during GIC events, Part 1**

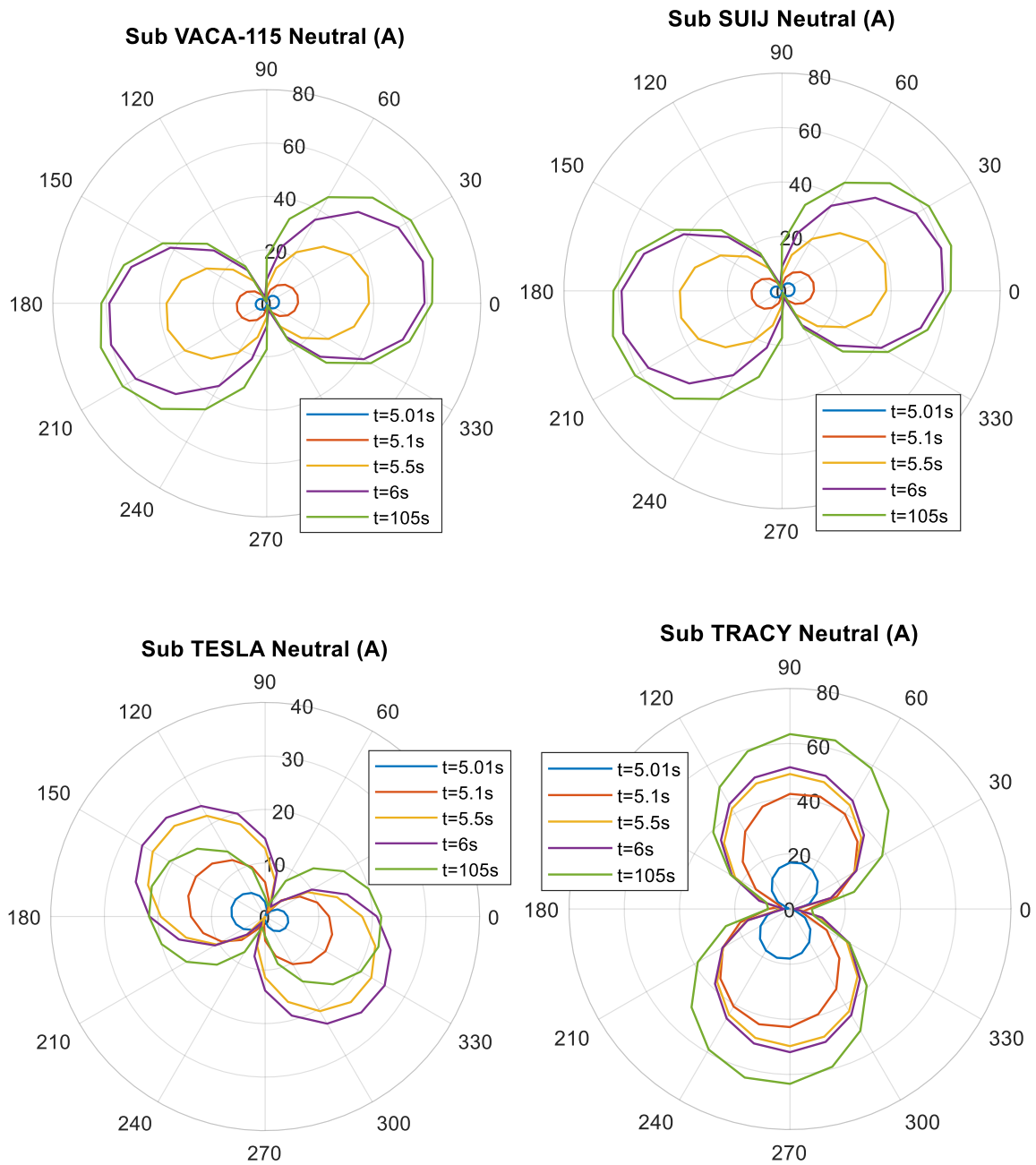


**Figure 6.5 Neutral Current at Substation Groundings during GIC events, Part 2**

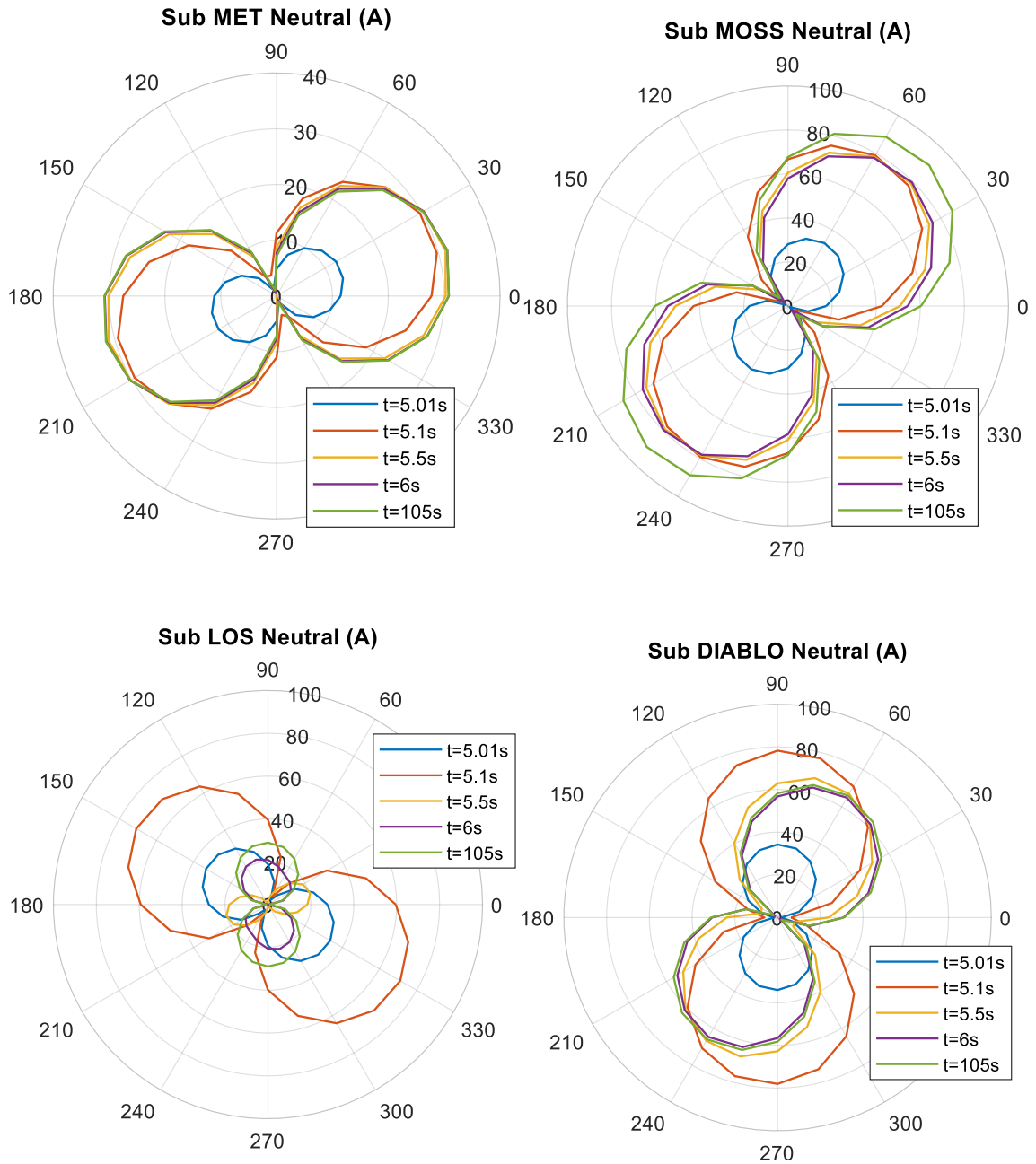


**Figure 6.6 Neutral Current at Substation Groundings during GIC events, Part 3**

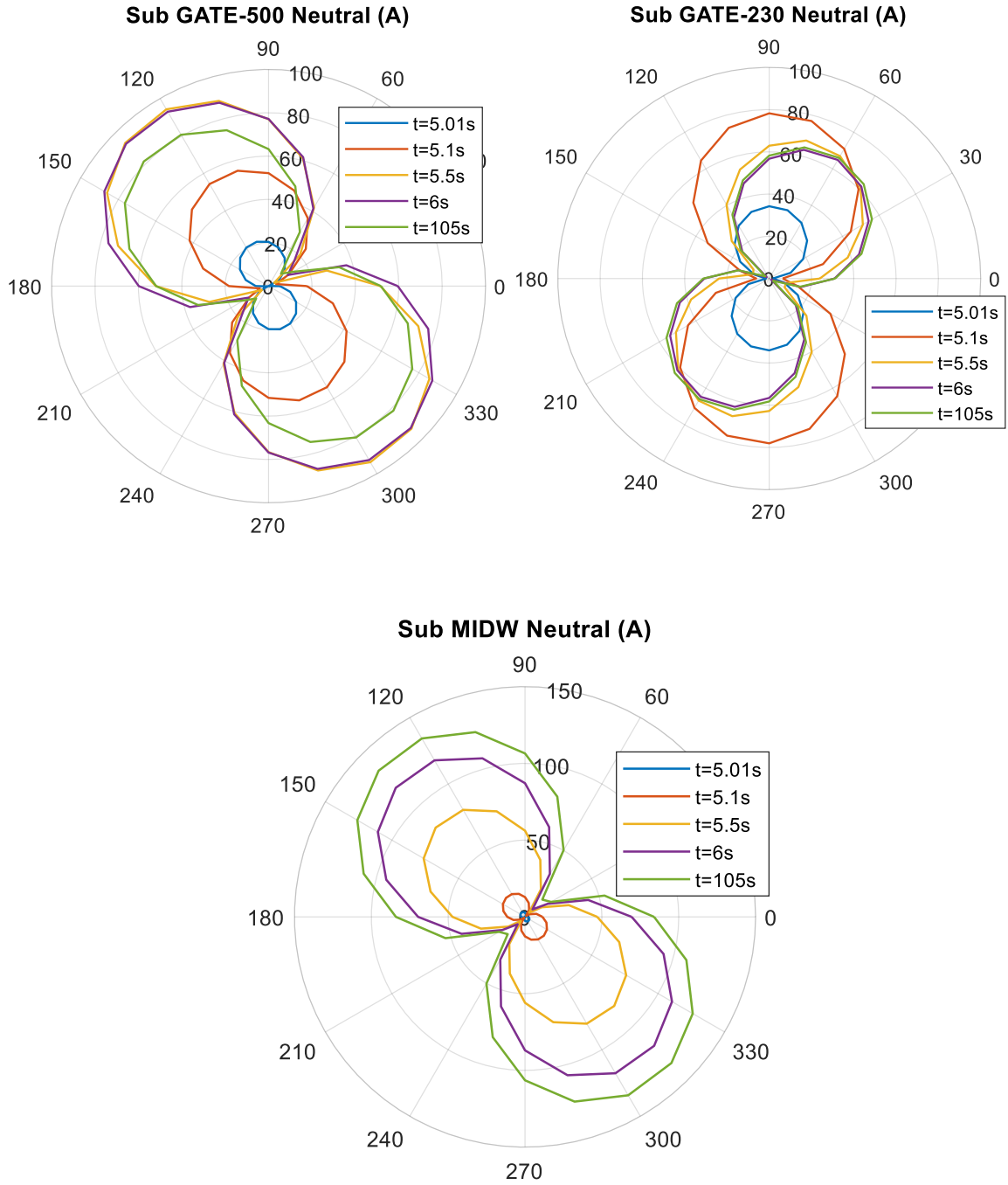


**Figure 6.7 Neutral Current at Substation Groundings during GIC events, Part 4**

## 6.2 GMD Field Estimation

The measurements from a magnetometer network installed near the involved grid enable a direct method to assess the impact of GIC on the power system, which is not available under some circumstances. Therefore, there exist several approaches attempting to quantify GMD [9]–[11] with large-area geomagnetic measurements, such as the  $Kp$  index and  $Ap$  index. These indices are derived from measurements at global geomagnetic observatory sites. These indices indicate worldwide geomagnetic activities and provide information for GIC related studies. However, due to their large sample intervals (usually one or three hours), it is difficult to directly relate them with the magnitude of GIC. In addition, some researchers [11] believe that  $Kp$  and  $Ap$  indices are not appropriate for predicting GIC since the indices become saturated during large storm events. Instead of indices, they use comparisons of storm morphology to achieve a better understanding of GIC. Some other attempts [49] are made to forecast peak GIC depending on suitable local geomagnetic indices. These existing methods are not capable of assessing the local geomagnetic disturbances in real-time. Therefore, a method focusing on the real-time local grid is designed to estimate the geoelectric field during GMD events.

This section proposes an approach to estimate the geoelectric field during GMD events using existing measurements from the power system [63], such as the terminal voltages and currents of the transmission lines. By modeling the induced geoelectric field during GMD as embedded voltage sources in transmission lines, the measurements of the electric quantities in power systems reveal the impact of GMD. Based on measurements from merging units, a time-domain state estimation process is developed to estimate the real-time magnitude of the geoelectric field.

### 6.2.1 Estimation Model Formulation

Based on the transmission line model in chapter 4, we formulate the measurement model for the transmission line. The measurements include:

- a) Actual measurements: three-phase current measurements and three-phase line-to-neutral voltage measurements, at both ends of the line.
- b) Virtual measurements: correspond to KVL laws in (11)
- c) Pseudo measurements: the voltages of neutrals, assumed to be very small values.

A numerical integration method converts the differential equations (17) into algebraic equations with states in two consecutive time steps,  $t_m$  and  $t$ .  $t_m$  is the time step before time  $t$  [64]–[66]. Equation (18) presents an example of actual measurements related to the voltage of phase A to neutral. Equation (19) presents an example of pseudo measurements of voltages at neutral. Equation (20) presents the equation for actual measurements related to current measurements and virtual measurements related to KVL laws.  $h$  is the length of 2 time steps.  $\tilde{\delta}$ , the measurement error in the measurement models, is related to the standard deviation of each measurement. The value of the standard deviation is relatively less for a more reliable measurement. The virtual measurements derived from KVL laws have theoretically zero error. In the unconstrained state estimation problem, the virtual measurements are assigned the least standard deviation (error) among all measurements. Meanwhile, the less reliable measurements, such as pseudo measurements, are assigned a larger standard deviation. For actual measurements, the standard deviation is obtained from the meter specifications. In this chapter, the standard deviation is 0.001 per unit for virtual measurements, 0.01 per unit for actual measurements, and 0.1 per unit for pseudo measurements.

$$\begin{cases} \mathbf{i}(t) = \mathbf{Y}_1 \mathbf{x}(t) + \mathbf{D}_1 \frac{d\mathbf{x}(t)}{dt} + \mathbf{C}_1 \\ 0 = \mathbf{Y}_2 \mathbf{x}(t) + \mathbf{D}_2 \frac{d\mathbf{x}(t)}{dt} + \mathbf{C}_2 \end{cases} \quad (17)$$

$$\begin{cases} z_1 \triangleq V_{AN1}(t) = v_{A1}(t) - v_{N1}(t) + \tilde{\delta}_1 \\ z_2 \triangleq V_{AN1}(t_m) = v_{A1}(t_m) - v_{N1}(t_m) + \tilde{\delta}_2 \end{cases} \quad (18)$$

$$\begin{cases} z_3 \triangleq 0 = v_{N1}(t) + \tilde{\delta}_3 \\ z_4 \triangleq 0 = v_{N1}(t_m) + \tilde{\delta}_4 \end{cases} \quad (19)$$

$$\mathbf{z} \triangleq [\mathbf{i}^T(t) \quad 0 \quad \mathbf{i}^T(t_m) \quad 0]^T = \mathbf{Y}_{eq} \mathbf{x}_{eq}(t) + \mathbf{B}_{eq} + \tilde{\delta} \quad (20)$$

where

$$\begin{aligned} \mathbf{x}_{eq}(t) &= [\mathbf{x}(t) \quad \mathbf{x}(t_m)]^T, \\ \mathbf{B}_{eq} &= \mathbf{N}_{eq} \mathbf{x}(t-h) + \mathbf{M} \mathbf{i}(t-h) + \mathbf{C}_{eq}, \\ \mathbf{Y}_{eq} &= \begin{bmatrix} \frac{4}{h} \mathbf{D}_1 + \mathbf{Y}_1 & -\frac{8}{h} \mathbf{D}_1 \\ \frac{4}{h} \mathbf{D}_2 + \mathbf{Y}_2 & -\frac{8}{h} \mathbf{D}_2 \\ \frac{1}{2h} \mathbf{D}_1 & \frac{2}{h} \mathbf{D}_1 + \mathbf{Y}_1 \\ \frac{1}{2h} \mathbf{D}_2 & \frac{2}{h} \mathbf{D}_2 + \mathbf{Y}_2 \end{bmatrix}, \mathbf{N}_{eq} = \begin{bmatrix} -\mathbf{Y}_1 + \frac{4}{h} \mathbf{D}_2 \\ -\mathbf{Y}_2 + \frac{4}{h} \mathbf{D}_2 \\ \frac{1}{2} \mathbf{Y}_1 - \frac{5}{2h} \mathbf{D}_1 \\ \frac{1}{2} \mathbf{Y}_2 - \frac{5}{2h} \mathbf{D}_2 \end{bmatrix}, \end{aligned}$$

$$\mathbf{M} = [\mathbf{I} \quad \mathbf{0} \quad -1/2 \mathbf{I} \quad \mathbf{0}]^T, \mathbf{C}_{eq} = [\mathbf{0} \quad \mathbf{0} \quad 3/2 \mathbf{C}_1 \quad 3/2 \mathbf{C}_2]^T$$

Based on the measurement data, the time domain state estimation scheme is applied to estimate the states in the model, including the magnitude of the geoelectric field. Following an object-oriented method [65], all measurement models  $z$  are formulated by the following equation:

$$z(t) = h(x(t)) + \tilde{\delta} \quad (21)$$

In equation (21),  $x$  contains the states of the transmission line,  $h(x(t))$  is the ideal model of measurements in terms of states and  $\tilde{\delta}$  is the measurement error vector. When the number of independent measurements exceeds the number of states, the solution for the minimization problem (22) is an appropriate estimation for the states. The solution minimizes the residuals between  $h(x(t))$  and  $z(t)$ , and the weight vector is  $\delta$ .

$$\min_{x(t)} \sum_{j=1}^m \left( \frac{h_j(x(t)) - z_j(t)}{\delta_j} \right)^2 \quad (22)$$

### 6.2.2 Numerical Results

- Test Case 1: Two Perpendicular Transmission Lines

The proposed approach is validated via an illustrative example in this section. A 115kV transmission system including two transmission lines is used to simulate the impact of GMD events, which is presented in Figure 6.8. For each line, the voltages and currents at the terminals are measured and the error of instrumentation channels is not considered. The DC component should be preserved, which can be achieved by instrumentation channel error correction algorithms or instrumentation transformers based on Hall effect or optical sensors. The sampling rate is 4800Hz, which corresponds to 80 samples per cycle for the 60Hz system. Then, the local geoelectric field is estimated using these measurements. The transmission lines span eastward and northward separately, and perpendicular to each other. Therefore, each of the transmission lines only



suffers from GMD in one direction. The transformers in the system are Y-Y connected and are modeled with saturable iron cores. The magnetizing currents of transformers are calculated using non-linear functions in terms of magnetic flux [67]. These non-linear functions describe the magnetic property of iron core as high degree polynomials. During GMD, the DC offset of flux saturates the transformer core, increasing reluctance in the magnetic circuit and the decrease of equivalent magnetizing inductance. Therefore, the magnetizing current is distorted. A simulated GMD event with a stair-step waveform in Figure 6.11 is introduced to the system at time  $t=1s$ , and the field is assumed to be uniform in this area. A portion of the measurements from transmission line 1 and transmission line 2 is depicted in Figure 6.9 and Figure 6.10 correspondingly. Since the load is not heavy in the system, a large proportion of the current comes from the magnetizing current of the transformer. We can observe the distortion of the transformer magnetizing current during GMD events in these figures. In addition, the distortion of current in line 2 is less severe than that in line 1, which is consistent with the fact that the simulated geoelectric field in northward is less than that in eastward at that time.

The estimation results of the geoelectric field using the proposed approach are shown in Figure 6.11. The DC components of the estimated geoelectric field magnitude are compared with the actual GMD event in the simulation. The results show that the proposed approach recovers the magnitude of the geoelectric field in both directions accurately. From  $t=0$  to  $t=1s$ , there are no geomagnetic disturbances in the system, and the estimation results remain zero. After  $t=1$ , the actual geoelectric field varies after every one second, ranging from 1V/km to 4 V/km. The variation of the estimated geoelectric field is highly consistent.

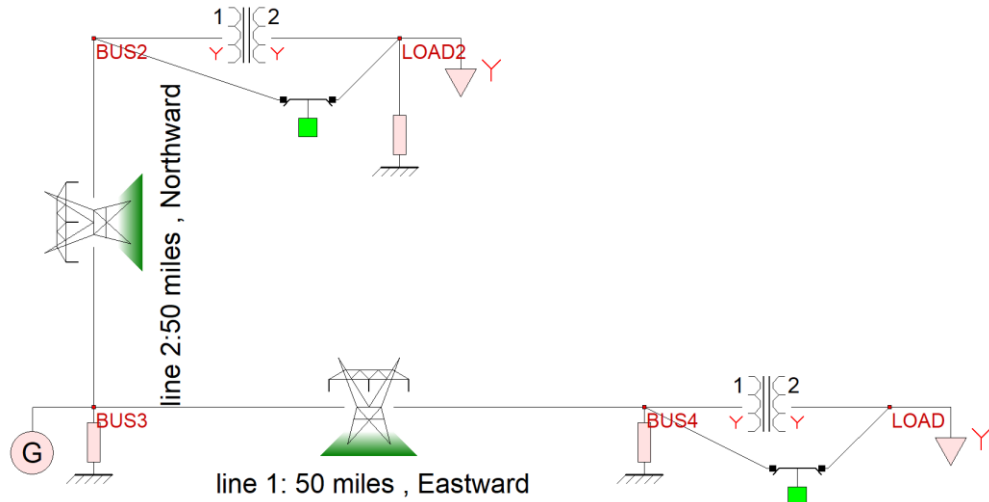


**Figure 6.8 Illustrative case 1: System Overview**

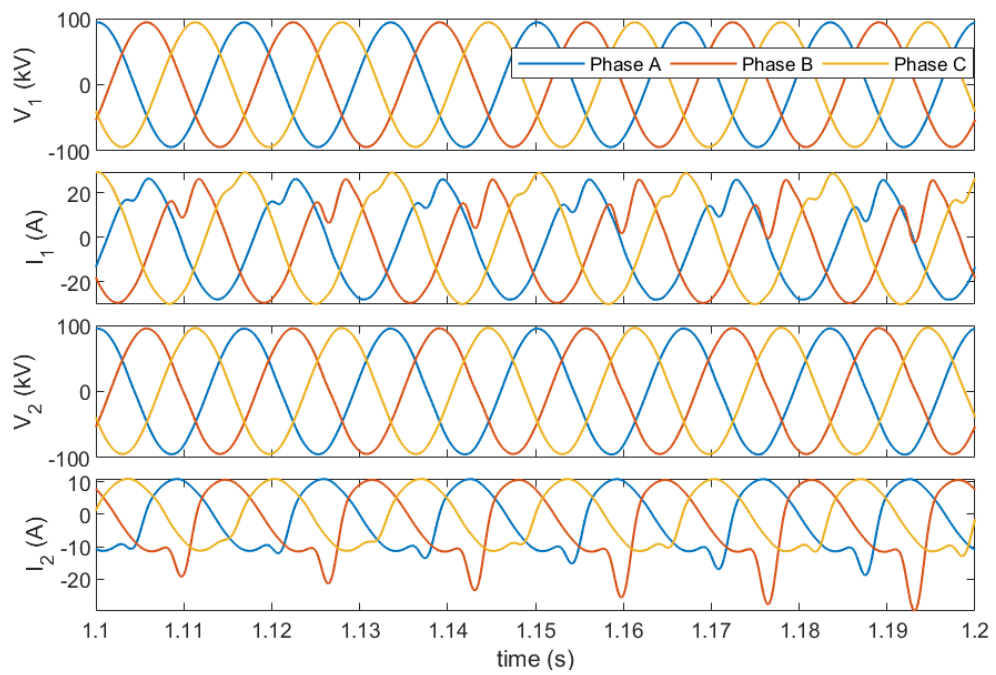


**Figure 6.9 Illustrative case 1: Measurements of Transmission Line 1**

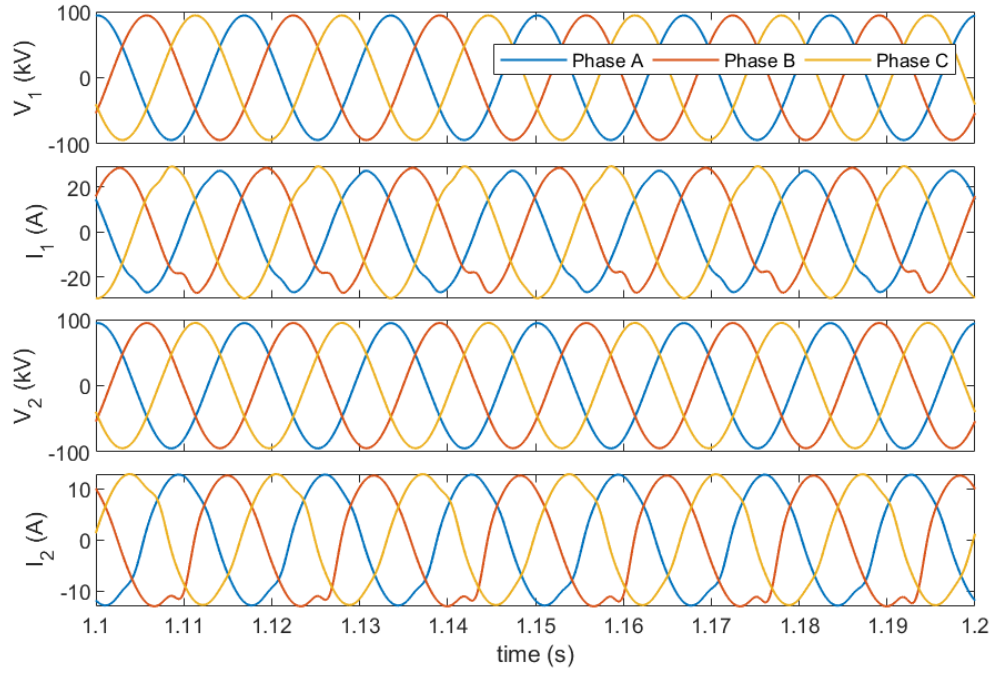


**Figure 6.10 Illustrative case 1: Measurements of Transmission Line 2**

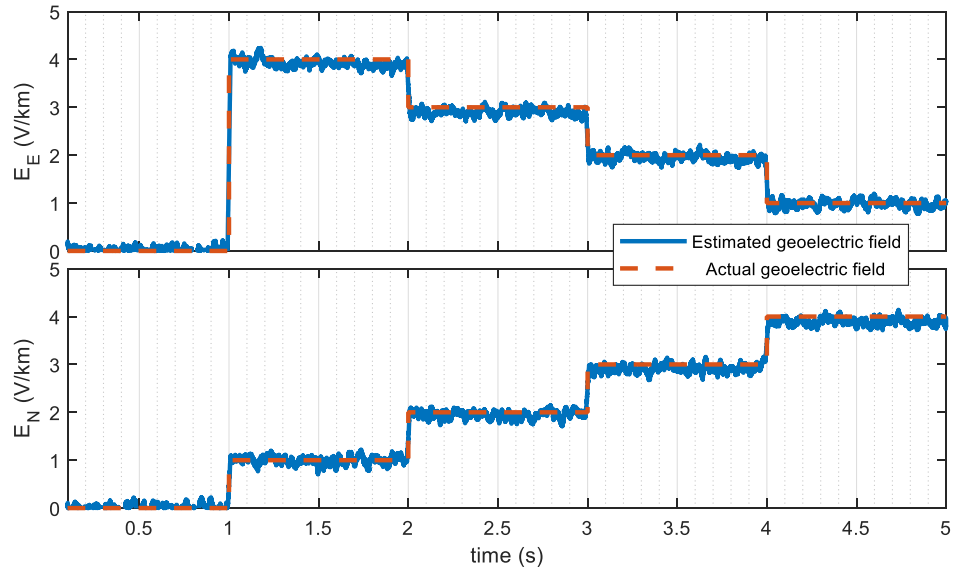


**Figure 6.11 Illustrative case 1: Results of Geoelectric Field Estimation**

- Test Case 2: Transmission Lines in Mesh Network

In test case 2, a more complex system in a meshed network is presented in Figure 6.12, where four buses and five transmission lines are considered. The coordinates of the buses are listed in Table 6.2. The coordinate data do not correspond to real-world locations. The length and direction of the lines are calculated from the coordinates. Other parameters are available in Table 6.3.

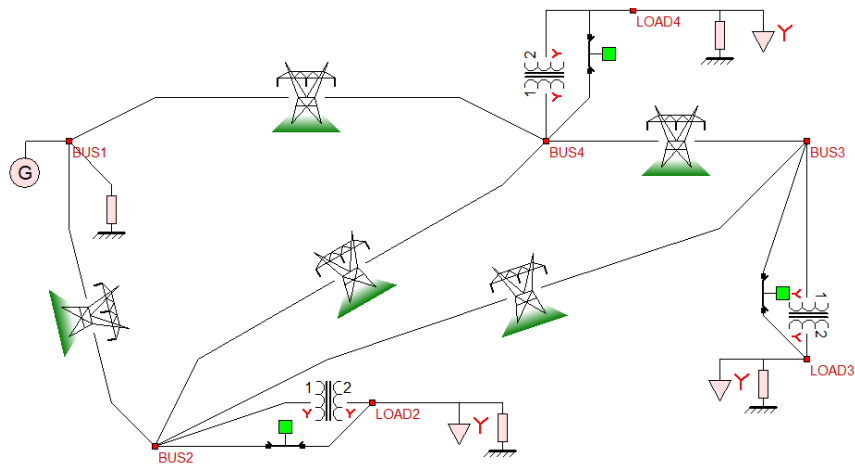


**Figure 6.12 Illustrative case 2: System Overview**

**Table 6.2 Coordinates of Buses**

	Longitude	Latitude
BUS1	60.00°W	60.00°N
BUS2	60.26°W	59.83°N
BUS3	61.88°W	60.00°N
BUS4	61.59°W	60.00°N

**Table 6.3 Parameters for Test Case 2**

Generator	138 kV, 100 MVA
Load 2	21.0 MW, 12.7 MVar
Load 3	30.0 MW, 1.0 MVar
Load 4	7.0 MW, 1.0 MVar
Transformer 2	138kV:25kV, 100 MVA, Y-Y  Magnetizing current: 0.005pu  The exponent of non-linear magnetizing current function :13
Transformer 3	
Transformer 4	

Similar to test case 1, the measurements of terminal voltages and currents for each line are collected. The proposed approach then estimates the geoelectric field assuming a uniform field. Two different GMD events are applied to the system. In the first event, a randomly generated 60s GMD event is introduced to the system. The estimation results are shown in Figure 6.13. In the second event, a GMD event in (23) containing harmonics in 0.01Hz and 0.05Hz is introduced to the system. In addition, measurement noise is considered in this case. Gaussian noise with zero mean and standard deviation of 0.002 (per unit value) is introduced to all measurements. The estimation results are shown in Figure 6.14. The estimated geoelectric field is compared against the actual field, and the results show that in both events the estimation results track the variation of actual values accurately.

$$\begin{aligned}
E_N &= \cos(2\pi \times 0.05t) + 5 \cos(2\pi \times 0.01t), \quad (\text{V/km}) \\
E_E &= \sin(2\pi \times 0.05t) + 5 \sin(2\pi \times 0.01t), \quad (\text{V/km})
\end{aligned} \tag{23}$$

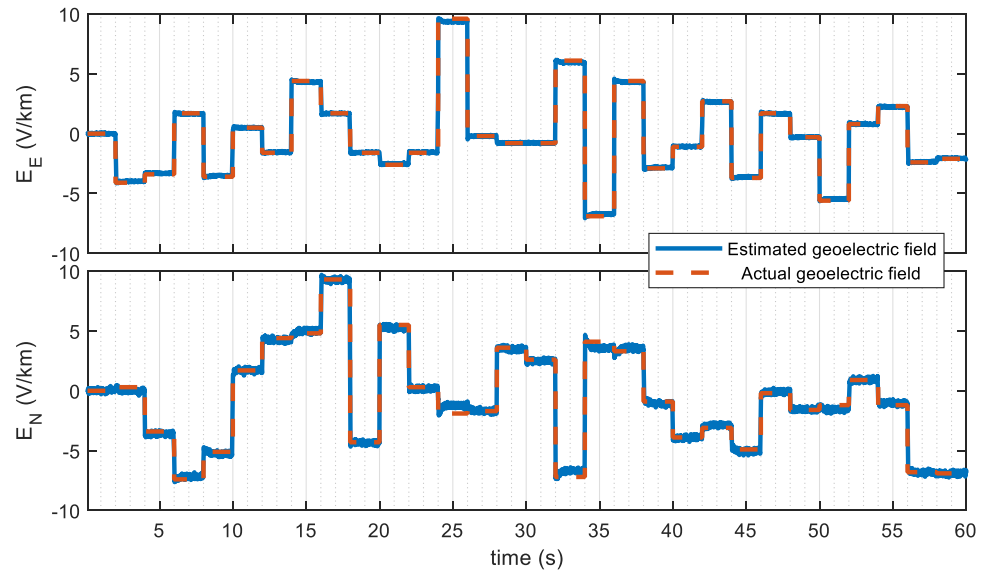


**Figure 6.13 Illustrative case 2: Results of Goelectric Field Estimation, Case 1**

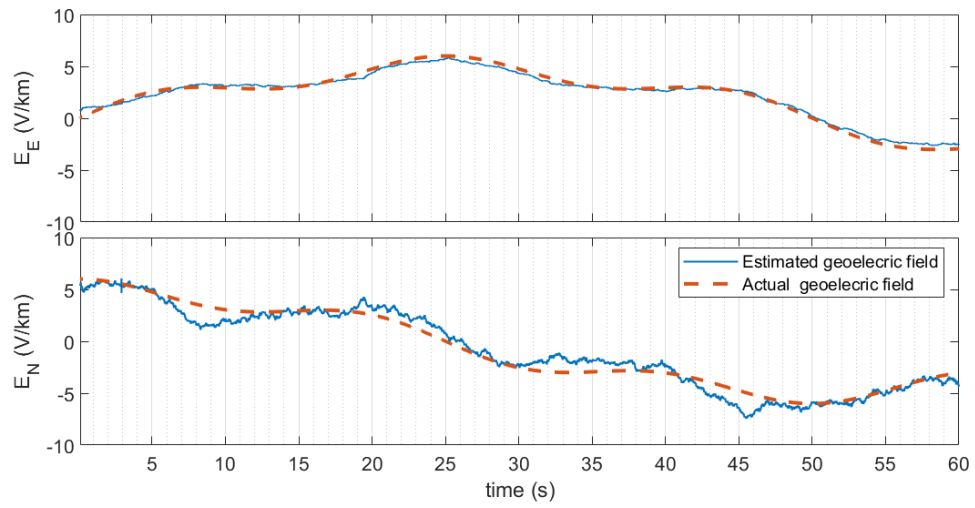


**Figure 6.14 Illustrative case 2: Results of Goelectric Field Estimation, Case 2**

### 6.3 Conclusions

In this chapter, the transients of GIC during the GMD events are investigated with a larger scale power grid modeled in time domain. A series of GMD events with different directions are applied to the grid. The resulting dynamics of GIC vary drastically at different locations. In addition, the results present short-term peaks of GIC, indicating the steady state value of GIC is not a complete indicator of the impact of GIC. There exist many cases displaying GIC with short duration but of high magnitude, which is ignored by simplified DC analysis for GIC. In addition, we propose an approach that estimates the geoelectric field during GMD events using measurements from power system devices, such as the measurements of terminal voltages and currents of the transmission lines. The geoelectric field induced by variation of the magnetic field is modeled as voltage sources embedded in transmission lines, and the measurements of the electric quantities in power systems reveal the impact of GMD. Based on time domain measurements, the unconstrained state estimation process is developed to estimate the real-time magnitude of the geoelectric field. The results show that our proposed method is able to estimate the changing geoelectric field accurately, which can be used to assess the intensity of GMD.

## **CHAPTER 7. HARMONIC ANALYSIS DURING GMD**

During geomagnetic disturbances, the magnetic core of the transformer will experience half-cycle saturation, and magnetizing current will drastically increase which is rich in harmonics. The harmonic levels generated by this process can reach levels that may destroy (melt the windings) the transformer as it has happened at the Salem nuclear plant in NJ during the GMD in March 1989 [1]. Prior research has reported harmonics ranging from second to 20<sup>th</sup> order with a pattern that includes both even and odd harmonics in descending magnitude with the harmonic order [15], [16]. Reference [15] indicates a significant level of even-order harmonics with the second harmonic higher than the third harmonic, the fourth harmonic higher than the fifth harmonic and so on. All harmonics increase in a nonlinear relation to GIC, although the slope is different for each harmonic. Reference [34] claims that harmonic magnitudes are sensitive to the air core reactance of transformers. When transformers are saturated, substantial levels of flux flow through the air and the air path reluctance affects the performance of saturated transformers. Reference [37] claims that transformers with three-limb cores have harmonics concentrating on lower order, while single-phase transformers will have substantial harmonics of higher orders. During these conditions, transformers will consume more reactive power as the magnetizing current is distorted, affecting the voltage stability of the system [16]. Harmonics may also adversely affect protective relaying algorithms leading to mis-operation. There are documented instances of the effects of harmonics on the protection of static VAR compensators on the Hydro-Quebec system during the March 1989 GMD event [13]. In this case, relay mis-operation due to



the GMD led to the Hydro-Quebec blackout. Another case of similar effects occurred in 2003; a power outage occurred in Malmö, Sweden during a geomagnetic storm [5]. The major reason was the loss of a 130kV transmission line, which was tripped by an overcurrent relay. Investigation showed that the relay had higher sensitivity at third-order harmonic than the fundamental frequency current. In this case, the relay characteristic value for third harmonics was much lower than the fundamental frequency. Another concern is related to current transformers which can saturate during GMD with serious effects on the protection scheme [46], [48], [47]. Reference [46] claims that harmonic restrained relays, such as transformer percentage differential relays, may fail to detect faults current during a GIC event. Reference [48] reports the usage of harmonics as an indicator of GIC impact on transformers. Reference [47] concludes based on simulations, that although there exist CT saturation even in small GIC level, modern relays with proper algorithms can discriminate against GIC generated harmonics.

Previous GMD events, as well as GMD studies, clearly show that the effects can be quite damaging to the power system. For this reason, models that accurately represent the effects of GMD on the power system are important for a realistic assessment of the effects of GMDs. While individual components have been extensively studied under GICs, similar comprehensive models for system-wide studies are not as well developed. Many approaches use a DC network model to compute the flow of the dc component into the system and then project the effect of the dc on the system. These approaches do not capture the interaction of dc, fundamental and harmonics on a network-wide basis. This section presents a method that does capture these interactions in GMD impact studies. The proposed modeling approach for the power system network integrates dynamic

models of transformers, power lines, grounding, generators, etc. and captures the nonlinear magnetics as well as the frequency dependence of the various parameters of power lines, grounding systems, etc. This chapter presents the modeling approach and provides results of the levels of harmonics generated by GIC as well as the propagation of the harmonics throughout the system [68]. Comparisons of the proposed model to other methods reported in the literature are provided. These comparisons indicate that the level of harmonics can be miscalculated if simpler models are used.

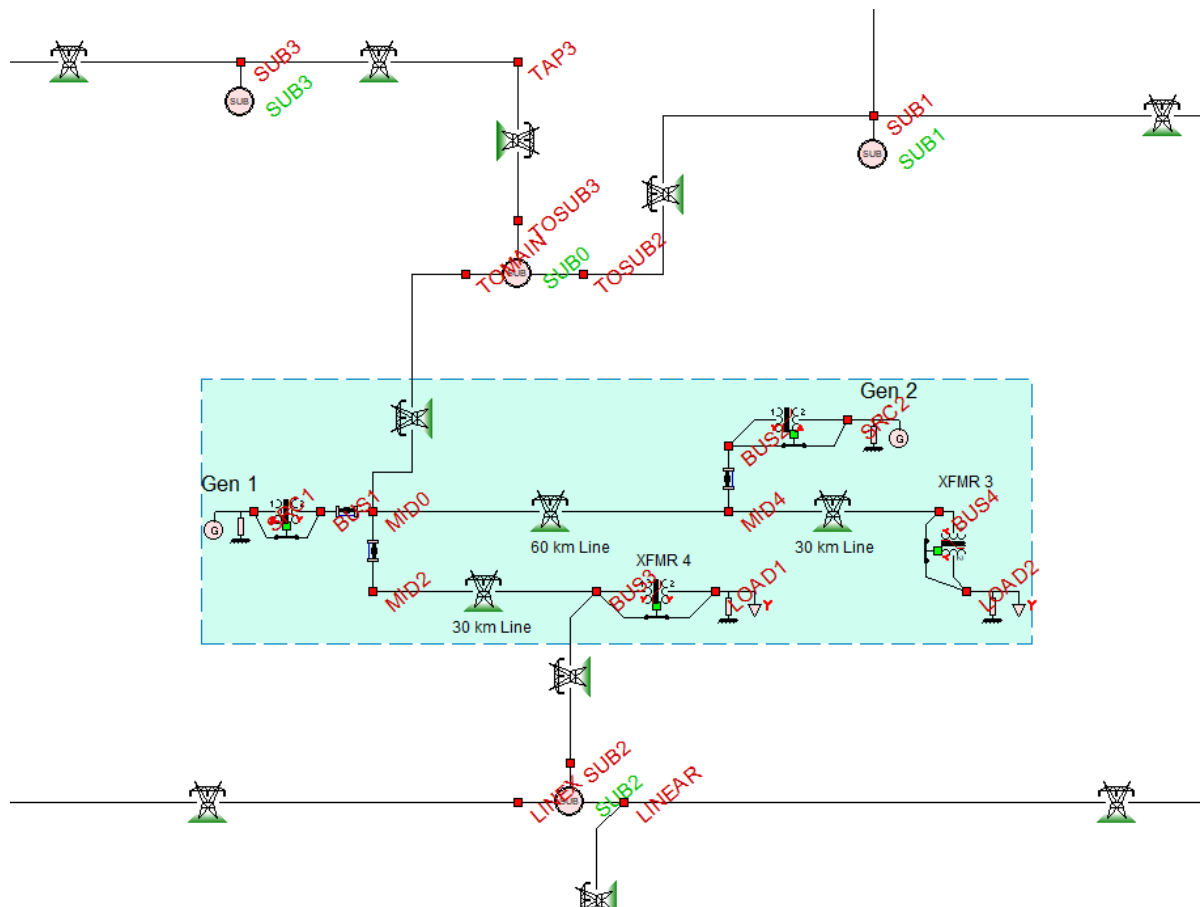


**Figure 7.1 GMD Testing System Overview**

## 7.1 Test Case Overview

The system in Figure 7.1 is used to investigate the generation and propagation of harmonics due to GMD. The area of interest is the shaded area, which is shown in Figure 7.2. There are two generators and two loads. Three 115kV transmission lines transfer power from sources to loads. The parameters of the various devices including the saturable core transformers are provided in Table 7.1.

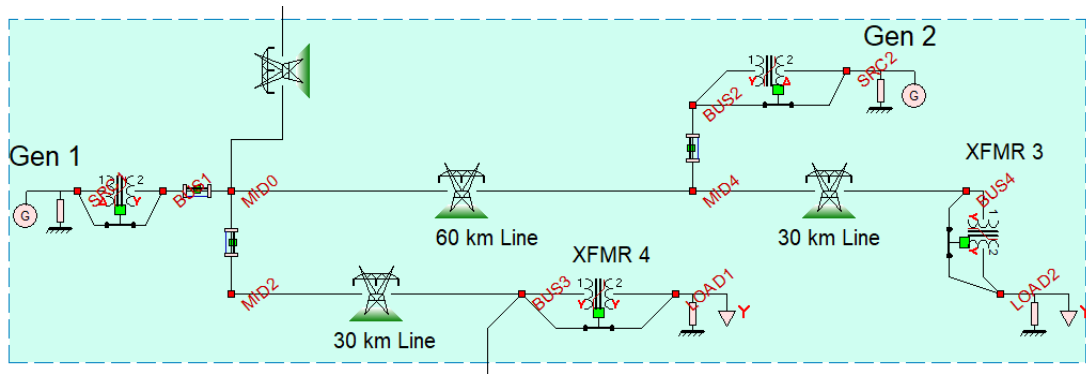


**Figure 7.2 GMD Study Area**

**Table 7.1 Example System Parameters**

<i>Device</i>	<i>Parameters</i>
Generator 1	34.5kV(L-L), balanced three-phase
Generator 2	18.1kV(L-L), balanced three-phase
Overhead transmission lines phase conductor	ACSR DARKE 60km 30km 30km
Overhead transmission lines shield	5/16HS
Transformer1	34.5kV/115 kV $\Delta$ -Y
Transformer2	18kV/115 kV $\Delta$ -Y
Transformer3,Transformer4	115 kV/ 115 kV, 100MVA Y-Y, Three-phase core form, Nominal magnetizing current 0.005 pu nonlinear inductance: exponent n=10
Load1	30 MVA, power factor=0.99 balanced three-phase
Load2	60 MVA, power factor=0.99 balanced three-phase

Simulation time step	50 $\mu$ s
GMD event 1	5V/km, GIC turns on at t=3s
GMD event 2	10V/km, GIC turns on at t=3s
GMD event 3	15V/km, GIC turns on at t=3s
GMD Direction	west-east aligned with transmission line in the study area

## 7.2 Numerical Results

The impact of GMD on the test system is investigated in this section. First, the GIC current flowing through the neutral of transformers is presented in Figure 7.3 for GMD event 1. As we can see, after GMD starts, the GIC gradually increases with a time constant of about 0.4 seconds. In steady-state, the GIC through transformer 4 is 65A, and the GIC through transformer 3 is 40A. In this test case, the direction of the GMD field is aligned with the two transmission lines from BUS1 to BUS4. As a comparison, we have computed the GIC using the DC network of this test system. The GIC through transformer neutral is 86A and 31.2A for transformers 4 and 3 respectively. We can observe that using the DC network model, the ratio of GIC at the two transformers is about 3, which is the ratio of the corresponding line lengths. The linear relationship exhibited with the DC network model is invalid due to the nonlinearities of the system and the different saturation levels of the transformers.

Next, the harmonics in the phases of the transformer are analyzed in Figure 7.4 and Figure 7.5. The harmonic magnitudes are normalized with respect to the fundamental. The DC component increases as the transformer is in half-cycle saturation, and the magnetizing current has a non-zero DC offset. Note the profound generation of even-order harmonics due to the GMD. The figures provide the harmonics for three different levels of GMD: 5 V/km, 10 V/km, and 15 V/km. Even and odd harmonics exist

and the magnitude decreases with the harmonic order. The levels also increase as the GMD increases.

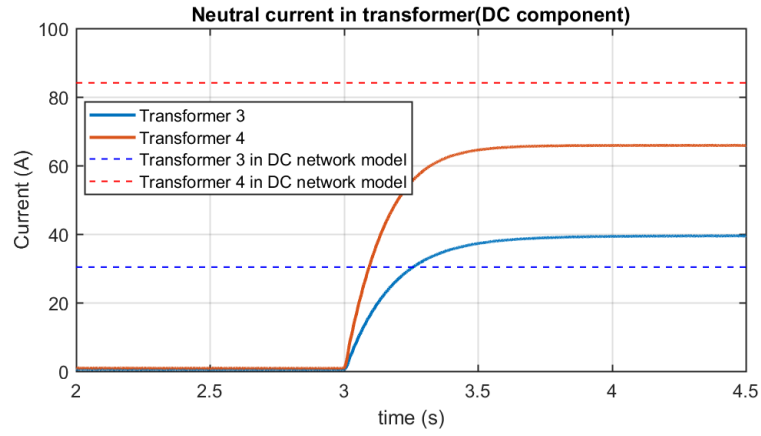


**Figure 7.3 DC Current at Neutral of Transformers**

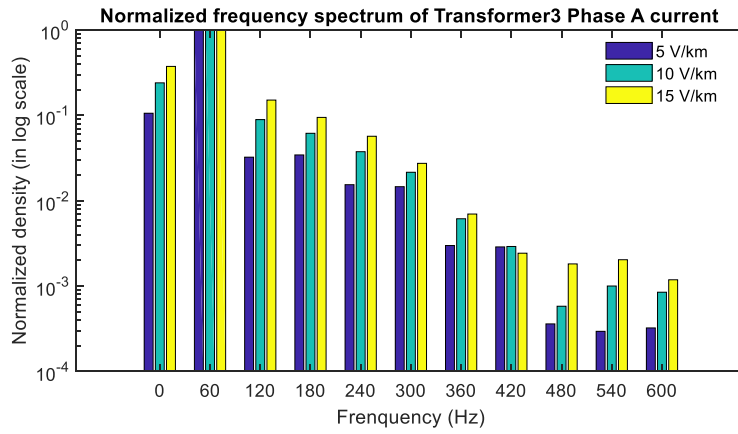


**Figure 7.4 Harmonic Analysis of Transformer 3 Phase Current**

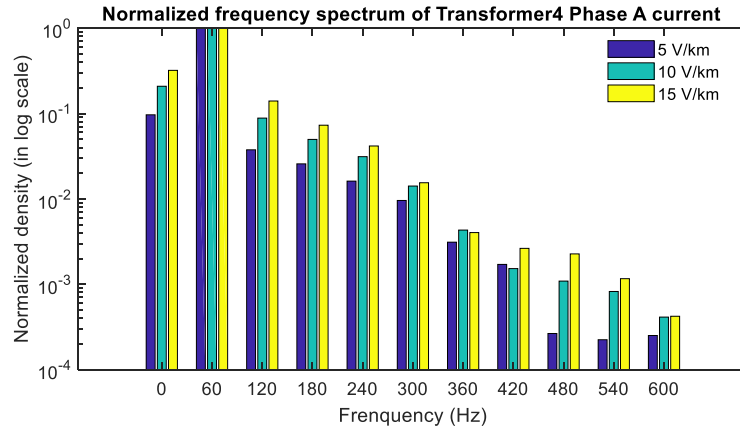


**Figure 7.5 Harmonic Analysis of Transformer 4 Phase Currents**

Figure 7.6 and Figure 7.7 show neutral harmonics for transformers 3 and 4 respectively. The DC component is the largest component. The percentage of second-order and fourth-order harmonics is not large, though there are apparent increases in corresponding components in phase current. The reason is that these harmonics mainly consist of positive and negative sequences, so the sum of three-phase harmonics is small.

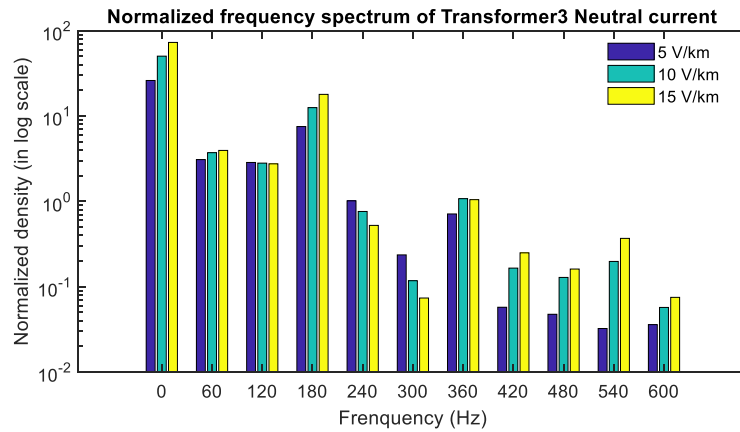


**Figure 7.6 Harmonic Analysis of Transformer 3 Neutral Current**

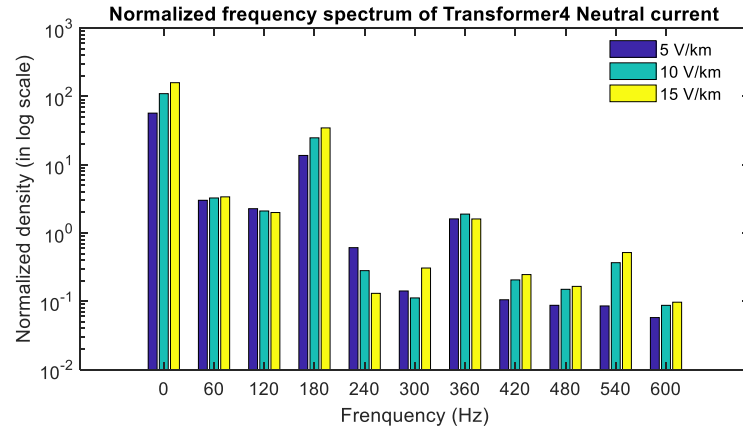


**Figure 7.7 Harmonic Analysis of Transformer 4 Neutral Current**

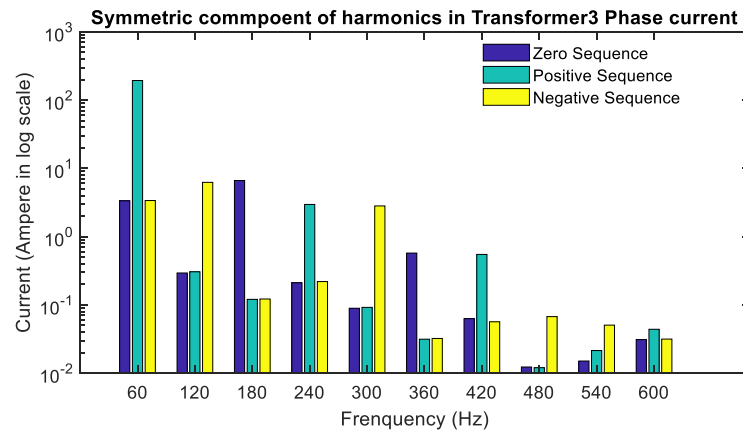


**Figure 7.8 Symmetric Component of Harmonics in Transformer 3**

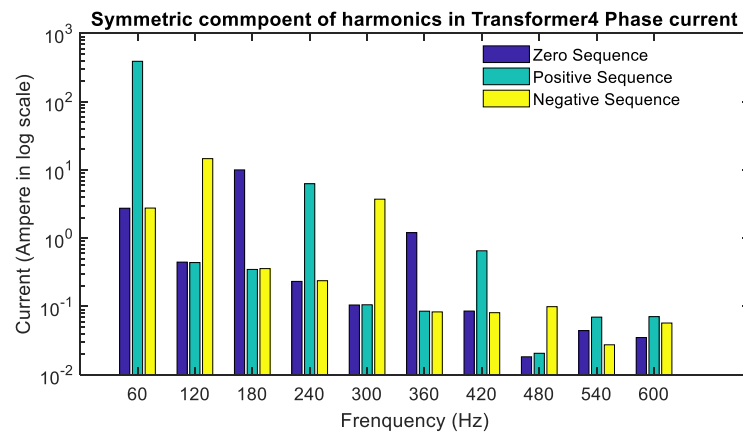


**Figure 7.9 Symmetric Component of Harmonics in Transformer 4**

Third and sixth order harmonics include more zero sequence components, which can be validated in Figure 7.8 and Figure 7.9. This is why the third and sixth harmonics are larger than the other components in the neutral.

Harmonics from GMD may affect the operation of generators. Figure 7.10 and Figure 7.11 show the harmonics at the terminals of generators. Since the step-up transformer is connected in  $\Delta$ -Y, the DC component and the zero sequence components of the harmonics cannot flow through the transformer into generators. The even-order harmonics from saturated transformers do have a large impact on the generators. The second-order and fourth-order harmonics rise drastically.

Another influence of GMD is the increased consumption of reactive power. Figure 7.12 shows the increase of base frequency reactive power production (MVar) in generators. The generator produces more reactive power during GMD activities. Figure 7.13 shows the variation of harmonic reactive power production (kVar) in generators. These decreasing values indicate the generators consume more reactive power at harmonics frequency during GMD activities. In this case, the variations of reactive power at the base frequency and at harmonics are moderate. However, for transmission systems that may exhibit resonances and amplify certain harmonics, the increase may be substantial



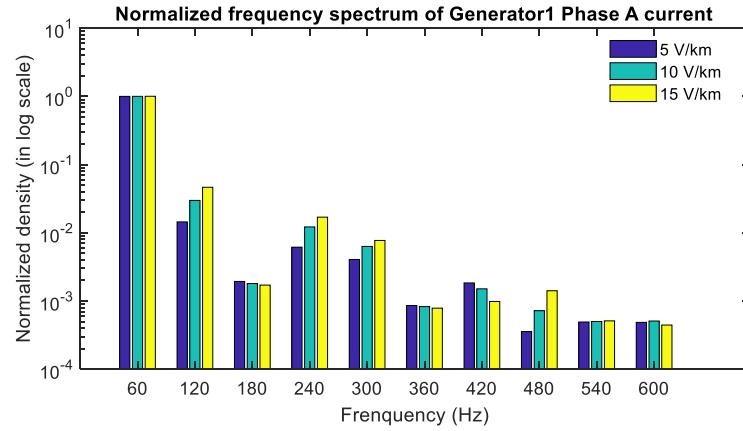


**Figure 7.10 Harmonic Analysis of Generator 1 Phase Current**

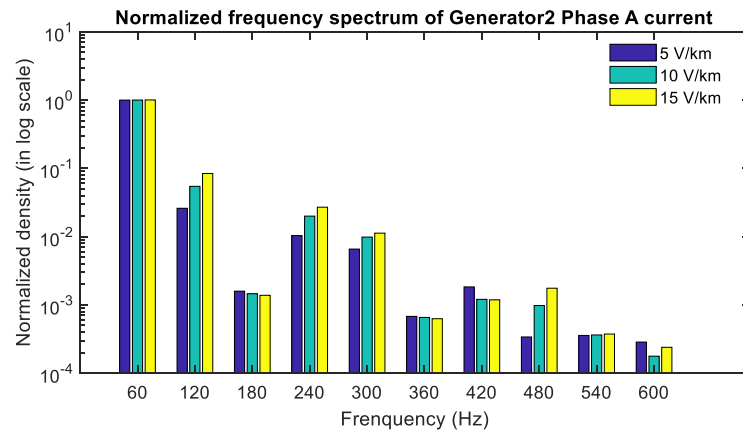


**Figure 7.11 Harmonic Analysis of Generator 2 Phase Current**

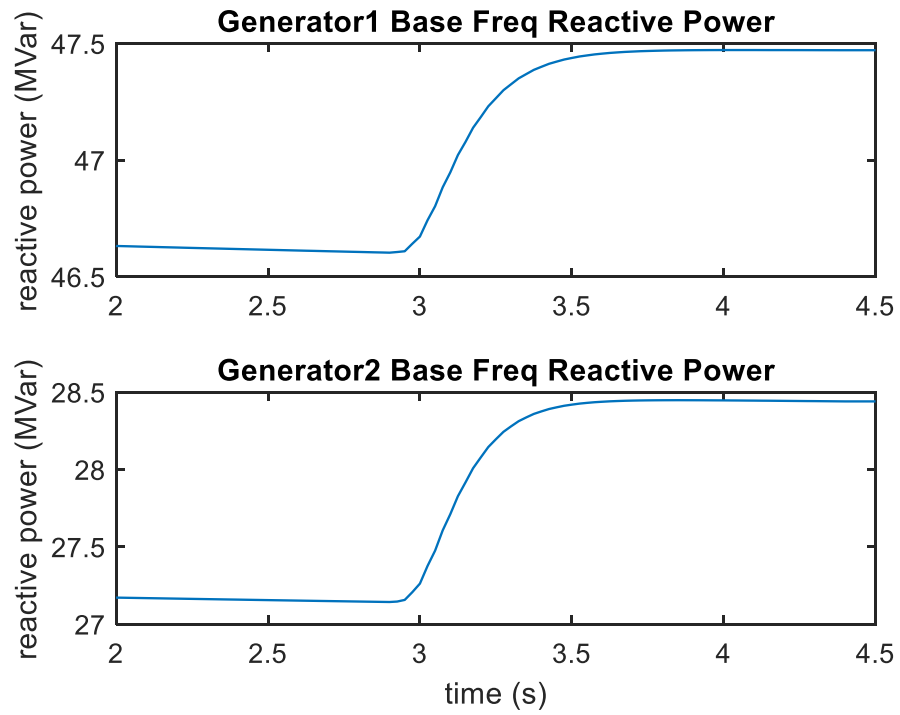


**Figure 7.12 Base Frequency Reactive Power Production of Generators**

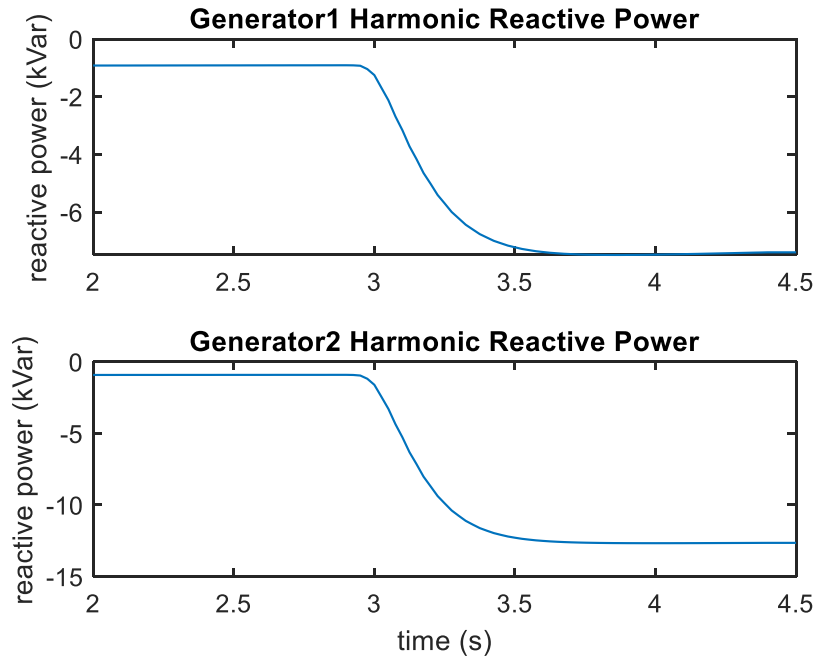


**Figure 7.13 Harmonics Reactive Power Production of Generators**

### **7.3 Conclusions**

We presented a method for accurate simulation of the effects of GMD on power systems using a time domain method. The method relies on high fidelity models of transformers, transmission lines and grounding systems for accurate simulation of DC flow and harmonics. The models provide the level of harmonics at transformers and generators. The even-order harmonics such as second and fourth-order harmonics are the most obvious phenomenon during GMD. These harmonics can challenge the system operation. The half-cycle saturation of transformers is the major source of these harmonics. Increasing demand for reactive power is also observed in the system, which requires the corresponding action to ensure voltage stability.

## **CHAPTER 8. PROTECTION SYSTEM PERFORMANCE DURING GMD**

The frequency of GIC is relatively low (0.0001Hz to 1 Hz), which causes half-cycle saturation of iron core circuits and subsequent distortion of the current and voltage waveforms with harmonics ranging from 2<sup>nd</sup> order to 20<sup>th</sup> order [16]. In addition to overheating transformers and other iron core circuits, increases in reactive power consumption, the waveform distortion may lead to relay mis-operations [48]. Many protective relays are calibrated at the base frequency, so the performance of these relays with distorted measurements is worth investigating. In October 2003 [5], a GIC event led to a large scale blackout in the southern region in Sweden. The major reason was the loss of a 130kV transmission line, which was tripped by an overcurrent relay. Investigation showed that the relay had a higher sensitivity at the third-order harmonic than the fundamental frequency current. In this case, the relay characteristic value for third harmonics was much lower than the fundamental frequency. The involved relay was replaced afterward by a relay that is less sensitive at 150 Hz than at 50 Hz. Meanwhile, GMD may lead to substantial instrumentation channel errors as well. For example, DC current in the primary of CTs causes half-cycle saturation of CTs and subsequent distorted data into the relays. These errors in measurement data further increase the possibility of relay mis-operation.

Dynamic state estimation based protection (EBP) is an emerging protection technique [65], [69], which integrates all available measurements in zone protection to improve the reliability of the protection scheme and withstand hidden failures. EBP

scheme models the entire protection zone using an object-oriented method, which is referred to as quadratized dynamic model (QDM). EBP monitors the consistency between measurements and related physically-based models. For example, the measurements of voltage, current, and temperature from a protection zone should follow Kirchhoff's Current/Voltage Law (KCL/KVL) and thermodynamic laws. Once internal faults occur in the protection zone, the EBP is able to detect a violation of physical laws, and faulted devices can be tripped. Like other relay methods, accurate measurement input is essential to the reliable operation of the EBP. A state estimation based instrumentation channel error correction scheme [70] is applied to eliminate the effect of instrumentation channel transformer saturation. This enables the protection scheme to operate with accurate measurement data without the error introduced by GMD.

In this chapter, the performance of EBP during the GMD is investigated and compared with conventional relays. In addition, an EBP with instrumentation error correction is proposed, which further improves the performance of EBP and is especially applicable when GMDs occur [71]. The overview of the procedure is shown in Figure 8.1. An estimation based error correction scheme removes the error introduced in instrumentation channels. Next, these corrected values are streamed to EBP. A protection model with the dynamics of devices considering different harmonics is provided at the same time. The dynamic state estimation (DSE) algorithm will issue a trip decision based on the consistency between the model and measurements.

This chapter is organized as follows. Section 1 introduces the dynamic state estimation based protection method. Section 2 introduces the instrumentation channel error correction method. Section 3 describes the developed device model for a protection

scheme. Section 4 provides numerical results to demonstrate the effect of the proposed error correction method. Section 5 uses an example with transformers and capacitor banks to demonstrate the reliability of EBP during GMD, which is then compared against conventional protection schemes. And Section 6 summarizes this chapter.

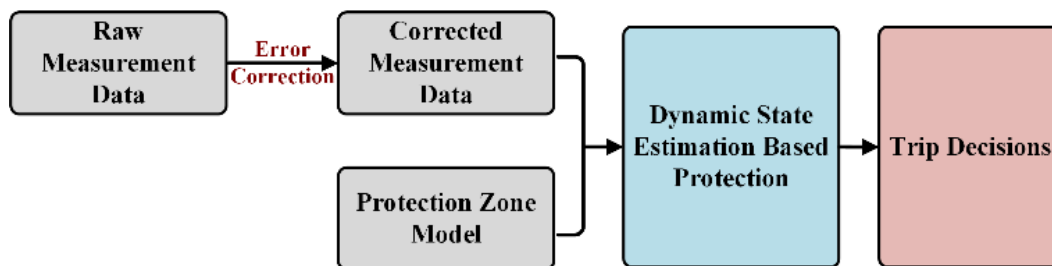


**Figure 8.1 Overview of the Estimation Based Protection**

## **8.1 Dynamic State Estimation-Based Protection**

The EBP scheme is inspired by differential protection, which monitors the sum of currents flowing into the protection zone and ensures the KCL is not violated. In EBP, all existing measurements in the protection zone and related physical laws are integrated into a dynamic state estimation process, any violation of physical law indicates the occurrence of an internal fault. In this section, we introduce the standard modeling syntax for the protection zone, the standard measurement model and the state estimation algorithm in EBP.

### *8.1.1 Quadratized Dynamic Model for Protection Zone*

In general, the devices in the protection zone are described by a set of differential equations derived from physical laws. In EBP, we formulate all device models according to a standard syntax in equation (1), which is referred to as Quadratized Dynamic Model

(QDM). This syntax is compatible with multiple physical laws[72], [73]. QDM includes the internal variables  $x(t)$ , and the through variables  $i(t)$ .  $Y_{eqx}$ ,  $D_{eqx}$  and  $C_{eqc}$  are the coefficients for the linear term, differential term, and constant term respectively. High order polynomials are quadratized to second-order terms by introducing auxiliary variables, and the coefficients are stored in  $F_{eqxx}$ .

$$\begin{aligned}
i(t) &= Y_{eqx1} \mathbf{x}(t) + D_{eqxd1} \frac{d\mathbf{x}(t)}{dt} + C_{eqc1} \\
0 &= Y_{eqx2} \mathbf{x}(t) + D_{eqxd2} \frac{d\mathbf{x}(t)}{dt} + C_{eqc2} \\
0 &= Y_{eqx3} \mathbf{x}(t) + \left\{ \mathbf{x}(t)^T \begin{pmatrix} \vdots \\ F_{eqxx3}^i \\ \vdots \end{pmatrix} \mathbf{x}(t) \right\} + C_{eqc3}
\end{aligned} \tag{24}$$

Based on the QDM model of the protection zone, measurement models in the equation (25) are developed in terms of internal variables  $x(t)$ .  $z(t)$  are measurements from the protection zone. These measurements derived from physical laws are referred to as virtual measurements[65]. In addition, we have three other measurements. Actual measurements represent measurements generated from actual meters and sensors; Derived measurements are quantities that are related to other quantities, for which an actual measurement is available; Pseudo measurements are quantities we have assumptions. For example, neutral voltages should be close to zero.

$$z(t) = Y_x \mathbf{x}(t) + \left\{ \mathbf{x}(t)^T \begin{pmatrix} \vdots \\ F_x^i \\ \vdots \end{pmatrix} \mathbf{x}(t) \right\} + D_x \frac{d\mathbf{x}(t)}{dt} + C \tag{25}$$

Using numerical integration methods[74], the differential terms are replaced with functions in terms of states at consecutive time steps. As a result, the protection zone models and measurement models are transformed into the Algebraic Quadratic Companion Form model (AQCF) in equation (26).

$$z(t, t_m) = Y_{m,x} \mathbf{x}(t, t_m) + \left\{ \mathbf{x}(t, t_m)^T \begin{pmatrix} \vdots \\ F_{m,x}^i \\ \vdots \end{pmatrix} \mathbf{x}(t, t_m) \right\} + C_m \quad (26)$$

### 8.1.2 Unconstraint Optimization Method for Dynamic State estimation

$$\min_{x(t)} \zeta(t) = \sum_{i=1}^n \left( \frac{h_i(x(t)) - z_i(t)}{\delta_i} \right)^2 \quad (27)$$

After the construction of the AQCF model, a weighted least square problem is formulated in EBP. Equation (27) is the general form for the unconstraint optimization method for DSE, where  $n$  is the total number of measurements,  $z_i(t)$  is the measurement value,  $h_i(t)$  is the measurement  $i$  in terms of the states, and  $\delta_i$  is the standard deviation of the corresponding measurement. To solve the problem (27), a Gauss-Newton iterative algorithm is used:

$$x^{v+1} = x^v - (H^T W H)^{-1} H^T W (h(x^v) - z) \quad (28)$$

Where  $x^v$  refers to the estimate of the state vector  $x$  at iteration  $v$ ,  $H$  is the Jacobian matrix of the measurement equations, and  $W$  is the weighting matrix.

$$H = \frac{\partial h(x)}{\partial x}, W = \text{diag}(\dots, \frac{1}{\delta_i^2}, \dots)$$



By solving the problem in (27) , the optimal estimation of the state variables is obtained. The estimated states are substitute into measurement models to get the estimated measurements. Assuming the error in measurements are independent random variables with standard normal, the objective value  $\zeta$  in equation (27) is distributed according to chi-squared distribution  $\chi^2$  . Based on this, a metric named as confidence level is available, which indicates the goodness of estimation[75]. The probability of  $\chi^2 \geq \zeta$  , with  $\nu$  degrees of freedom is named confidence level, which is given by:

$$P = \Pr[\chi^2 \geq \zeta] = 1 - \Pr[\chi^2 \leq \zeta] = 1 - \Pr(\zeta, \nu)$$

A high confidence level suggests the measurement is consistent with physical models, while a low confidence level implies the occurrence of internal faults. The trip decision is released based on a user-defined delay time and a reset time as shown in (29).

$$trip = \begin{cases} 1, & \text{if } \int_{t-t_{reset}}^t (1 - P(\tau)) d\tau > t_{delay} \\ 0, & \text{otherwise} \end{cases} \quad (29)$$

## 8.2 Instrumentation Channel Error Correction

The instrumentation channels interface the electric power system with high voltage/current and protective relays with low voltage/current. A typical instrumentation channel includes potential transformers (PT) or current transformers (CT), instrumentation cables, and merging units. Ideally, the secondary voltage and current of instrumentation channels should be exactly proportional to the primary quantities. However, the DC voltage generated by GMD would introduce DC flux in iron cores of

instrumentation transformers, leading to distorted magnetizing current. The non-sinusoidal magnetizing current will increase significantly as the DC flux increases, leading to gross distortion in measurements from the burden resistor. In addition, other harmonic components would lead to additional error, because the frequency responses of instrumentation channels are different for different harmonics. These distorted measurements risk the operation of protective relays [76]. Many protective relays are calibrated at the base frequency, so the performance of these relays with distorted measurements is worth investigation.

In this chapter, we propose a state estimation based error correction method for instrumentation channels. The proposed method relies on the physically-based instrumentation channel models, the measurements from burden resistors and the dynamic state estimation procedure mentioned in the previous section. The approach to model the instrumentation channels is elaborated in this section.

### 8.2.1 Current Instrumentation Channel Measurement Models

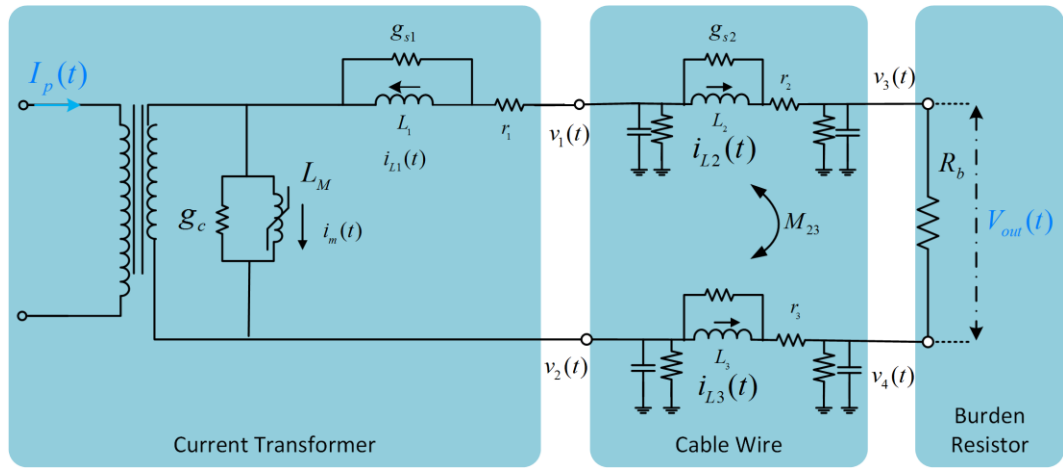


**Figure 8.2 Equivalent Circuit of CT's Primary Current Estimation**

Figure 8.2 shows an equivalent circuit for the CT channel error correction, including the current transformer with a saturable iron core, copper instrumentation cables and burden resistor in merging units. Since the current transformer possesses an iron core, the magnetizing inductance  $L_m$  is modeled by the nonlinear equation in (7). Where  $i_m$  is the magnetizing current transformed to the secondary side,  $\lambda$  is the instantaneous value of flux linkage. Parameters  $i_0, \lambda_0, L_0$  are the nominal values for magnetizing current, flux linkage, and linear inductance respectively. The order  $n$  defines the degree of nonlinearity of the model.

$$0 = i_m(t) - i_0 \left( \frac{\lambda(t)}{\lambda_0} \right)^n - \frac{1}{L_0} \lambda(t) \quad (30)$$

We choose  $n=11$  for the test case in the test case. Following the standard syntax of the QDM model, this equation is quadratized to yield the following quadratized measurement models. Auxiliary variables  $y_1, y_2, y_3, y_4$  are introduced to decrease the maximum order of equations to 2.

$$\begin{aligned} 0 &= y_1(t) - \left( \frac{\lambda(t)}{\lambda_0} \right)^2 \\ 0 &= y_2(t) - (y_1(t))^2 \\ 0 &= y_3(t) - (y_2(t))^2 \\ 0 &= y_4(t) - y_3(t) \cdot y_1(t) \\ 0 &= i_m(t) - i_0 \left( \frac{\lambda(t)}{\lambda_0} \right) y_4(t) - \frac{1}{L_0} \lambda(t) \end{aligned}$$

In addition, other physical laws such as KCL and KVL provide more measurement models for CT channels:

KCL derived from CT:

$$0 = -g_m e(t) - i_m(t) + \frac{1}{n} i_p(t) + i_{L_1}(t) + g_{s1} L_1 \frac{di_{L_1}(t)}{dt}$$

KCL at the boundary between CT and cable:

$$0 = g_m e(t) + i_m(t) - \frac{1}{n} i_p(t) - i_{L_2}(t) - g_{s2} \left( L_2 \frac{di_{L_2}(t)}{dt} - M_{23} \frac{di_{L_3}(t)}{dt} \right)$$

$$0 = -g_m e(t) - i_m(t) + \frac{1}{n} i_p(t) + i_{L_3}(t) + g_{s3} \left( L_3 \frac{di_{L_3}(t)}{dt} - M_{23} \frac{di_{L_2}(t)}{dt} \right)$$

KVL derived from CT:

$$0 = -v_1(t) + v_2(t) + e(t) + L_1 \frac{di_{L_1}(t)}{dt} + r_1 \left( g_m e(t) + i_m(t) - \frac{1}{n} i_p(t) \right)$$

KVL derived from cable:

$$0 = -v_3(t) + v_1(t) + r_2 \left( i_{L_2}(t) + g_{s2} \left( L_2 \frac{di_{L_2}(t)}{dt} - M_{23} \frac{di_{L_3}(t)}{dt} \right) \right) + L_2 \frac{di_{L_2}(t)}{dt} - M_{23} \frac{di_{L_3}(t)}{dt}$$

$$0 = -v_2(t) + v_4(t) + r_3 \left( i_{L_3}(t) + g_{s3} \left( L_3 \frac{di_{L_3}(t)}{dt} - M_{23} \frac{di_{L_2}(t)}{dt} \right) \right) + L_3 \frac{di_{L_3}(t)}{dt} - M_{23} \frac{di_{L_2}(t)}{dt}$$

KCL at the boundary between burden resistor and cable:

$$0 = i_{L_2}(t) + g_{s2} \left( L_2 \frac{di_{L_2}(t)}{dt} - M_{23} \frac{di_{L_3}(t)}{dt} \right) + g_b (v_3(t) - v_4(t))$$

$$0 = -i_{L_3}(t) - g_{s3} \left( L_3 \frac{di_{L_3}(t)}{dt} - M_{23} \frac{di_{L_2}(t)}{dt} \right) + g_b (v_4(t) - v_3(t))$$

Transformer magnetizing leg yields:

$$0 = e(t) - \frac{d\lambda(t)}{dt}$$

The aforementioned 14 measurements derived from physical laws are referred to as virtual measurements. Apart from virtual measurements, we have the following measurements to improve the redundancy of the scheme.

#### **Actual Measurements (1):**

$$v_{out}(t) = v_3(t) - v_4(t)$$

#### **Pseudo Measurements (1):**

node 4 is grounded:  $0^m = v_4(t)$

#### **Derived Measurements (4):**

$$i_b^m(t) = g_m e(t) + i_m(t) - \frac{1}{n} i_p(t)$$

$$i_b^m(t) = i_{L_1}(t) + g_{s1} L_1 \frac{di_{L_1}(t)}{dt}$$

$$i_b^m(t) = i_{L_2}(t) + g_{s2} \left( L_2 \frac{di_{L_2}(t)}{dt} - M_{23} \frac{di_{L_3}(t)}{dt} \right)$$

$$i_b^m(t) = -i_{L_3}(t) - g_{s3} \left( L_3 \frac{di_{L_3}(t)}{dt} - M_{23} \frac{di_{L_2}(t)}{dt} \right)$$

In which,  $i_b^m(t) = -g_b(v_3(t) - v_4(t))$

In summary, the current instrumentation channel model consists of 20 measurements and 15 states. The state variables include:

$$X = [v_1(t) \ v_2(t) \ v_3(t) \ v_4(t) \ e(t) \ \lambda(t) \ y_1(t) \ y_2(t) \ y_3(t) \ y_4(t) \ i_p(t) \ i_m(t) \ i_{L1}(t) \ i_{L2}(t) \ i_{L3}(t)]^T$$

It's worth mentioning that the primary current  $i_p(t)$  is a state variable, so the dynamic state estimation procedure will reveal the optimal estimation of  $i_p(t)$ , which are the corrected measurements for the current instrumentation channel.

### 8.2.2 Voltage Instrumentation Channel Measurement Models

Following a similar process, we can formulate the measurement models for PT. The parasitic capacitors in the primary winding and secondary winding are represented by  $c_1, c_2$  and  $c_3$ .

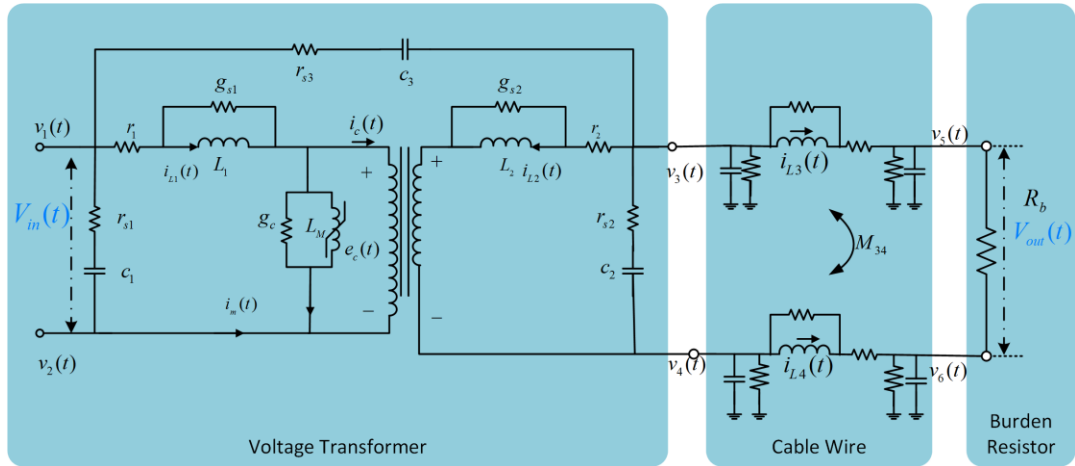


**Figure 8.3 Equivalent Circuit of PT's Primary Voltage Estimation**

In this test case, there are 20 states and 21 measurements. The states of the model include:

$$X = [v_1(t) \ v_2(t) \ v_3(t) \ v_4(t) \ v_5(t) \ v_6(t) \ i_{L_1}(t) \ i_{L_2}(t) \\ v_{c1}(t) \ v_{c2}(t) \ v_{c3}(t) \ e_c(t) \ i_m(t) \ i_c(t) \ \lambda(t) \ y_1(t) \ y_2(t) \ y_3(t) \ i_{L3}(t) \ i_{L4}(t)]^T$$

The voltages at the primary side of PT ( $v_1(t)$  ,  $v_2(t)$ ) are state variables, so the dynamic state estimation procedure will reveal the optimal estimation primary voltage, which is the corrected measurements for voltage instrumentation channel. The equations describing the measurement definitions for PT channel are listed in the following.

#### Actual Measurements (1):

$$V_{out}(t) = v_5(t) - v_6(t)$$

#### Pseudo Measurements (2):

node 2 and node 4 are grounded:

$$0 = v_2(t), 0 = v_4(t)$$

#### Virtual Measurements (18):

KCL at node 1, node 2 and node 4 yields:

$$0 = i_1(t) + i_2(t) + i_4(t) + i_6(t) \text{ , in which:}$$

$$i_1(t) = i_{L1}(t) + g_s L_1 \frac{di_{L1}(t)}{dt} + C_1 \frac{dv_{c1}(t)}{dt} + C_3 \frac{dv_{c3}(t)}{dt}$$

$$i_2(t) = -i_{L1}(t) - g_s L_1 \frac{di_{L1}(t)}{dt} - C_1 \frac{dv_{c1}(t)}{dt}$$

$$i_4(t) = -i_{L2}(t) - g_s L_2 \frac{di_{L2}(t)}{dt} - C_2 \frac{dv_{c2}(t)}{dt}$$

$$i_6(t) = (G_{21} + G_{s21})v_3(t) + (G_{22} + G_{s22})v_4(t) - G_{s21}v_5(t) - G_{s22}v_6(t) + C_{21} \frac{dv_3(t)}{dt} + C_{22} \frac{dv_4(t)}{dt} + i_{L4}(t)$$

KCL at node 3 yields:

$$0 = i_3(t) + i_5(t) \text{ , in which:}$$

$$i_3(t) = i_{L2}(t) + g_s L_2 \frac{di_{L2}(t)}{dt} + C_2 \frac{dv_{c2}(t)}{dt} - C_3 \frac{dv_{c3}(t)}{dt}$$

$$i_5(t) = (G_{11} + G_{s11})v_3(t) + (G_{12} + G_{s12})v_4(t) - G_{s11}v_5(t) - G_{s12}v_6(t) + C_{11} \frac{dv_3(t)}{dt} + C_{12} \frac{dv_4(t)}{dt} + i_{L3}(t)$$

KCL at node 5 yields:

$$0 = i_7(t) + i_9(t) , \text{ in which:}$$

$$i_7(t) = (G_{11} + G_{s11})v_5(t) + (G_{12} + G_{s12})v_6(t) - G_{s11}v_3(t) - G_{s12}v_4(t) + C_{11} \frac{dv_5(t)}{dt} + C_{12} \frac{dv_6(t)}{dt} - i_{L3}(t)$$

$$i_9(t) = v_5(t) / R_b - v_6(t) / R_b$$

KCL at node 6 yields:

$$0 = i_8(t) + i_{10}(t) , \text{ in which:}$$

$$i_8(t) = (G_{21} + G_{s21})v_5(t) + (G_{22} + G_{s22})v_6(t) - G_{s21}v_3(t) - G_{s22}v_4(t) + C_{21} \frac{dv_5(t)}{dt} + C_{22} \frac{dv_6(t)}{dt} - i_{L4}(t)$$

$$i_{10}(t) = -v_5(t) / R_b + v_6(t) / R_b$$

KVL derived from PT:

$$0 = v_1(t) - v_2(t) - e(t) - L_1 \frac{di_{L1}(t)}{dt} - r_1 \left( i_{L1}(t) + g_s L_1 \frac{di_{L1}(t)}{dt} \right)$$

$$0 = v_3(t) - v_4(t) - \frac{1}{N} e(t) - L_2 \frac{di_{L2}(t)}{dt} - r_2 \left( i_{L2}(t) + g_s L_2 \frac{di_{L2}(t)}{dt} \right)$$

$$0 = v_1(t) - v_2(t) - v_{c1}(t) - r_{s1} C_1 \frac{dv_{c1}(t)}{dt}$$

$$0 = v_1(t) - v_3(t) - v_{c3}(t) - r_{s3} C_3 \frac{dv_{c3}(t)}{dt}$$

$$0 = v_2(t) - v_4(t) - v_{c2}(t) - r_{s2} C_2 \frac{dv_{c2}(t)}{dt}$$



$$0 = i_{L1}(t) + g_s L_1 \frac{di_{L1}(t)}{dt} - i_c(t) - i_m(t) - g_c e(t)$$

$$0 = Ni_c(t) + i_{L2}(t) + g_s L_2 \frac{di_{L2}(t)}{dt}$$

KVL derived from cable:

$$0 = -v_3(t) + v_5(t) + R_{11}i_{L3}(t) + R_{12}i_{L4}(t) + L_{11} \frac{di_{L3}(t)}{dt} + M_{34} \frac{di_{L4}(t)}{dt}$$

$$0 = -v_4(t) + v_6(t) + R_{21}i_{L3}(t) + R_{22}i_{L4}(t) + M_{34} \frac{di_{L3}(t)}{dt} + L_{22} \frac{di_{L4}(t)}{dt}$$

Transformer magnetizing leg yields:

$$0 = e(t) - \frac{d\lambda(t)}{dt}$$

$$0 = i_m(t) - i_0 \frac{\lambda(t)}{\lambda_0} y_3(t) - \frac{1}{L_0} \lambda(t)$$

$$0 = y_1(t) - \frac{\lambda(t)^2}{\lambda_0^2}$$

$$0 = y_2(t) - y_1(t)^2$$

$$0 = y_3(t) - y_2(t)^2$$

### 8.3 Protected Device Modeling

In this chapter, we utilize a high-fidelity model for simulating the effects of GIC on power systems. The model is based on a detailed representation of power system frequency-dependent grounding models, low broadband modeling of transmission lines and transformer models with detailed magnetization characteristics [60], [68], [77], which is described in previous sections. Using this model, we present examples of effects

of GMD on the relaying system with geomagnetically induced currents into the power system via the grounds.

The model of a capacitor bank consists of the capacitor blocks inside the bank. A bank with 3 blocks in each phase is shown in Figure 8.4. A 5-block capacitor bank is used in the following result section. The internal faults are introduced as short circuits between one or more blocks in a specific phase.

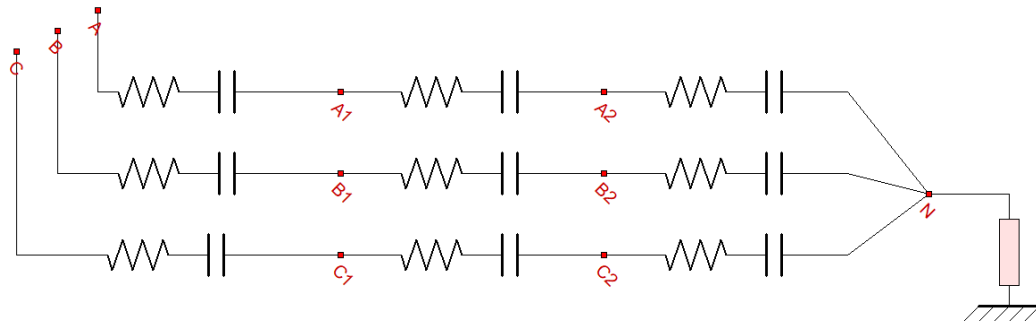


**Figure 8.4 Capacitor Bank Modeling**

#### **8.4 Validation of Error Correction Results**

Example test results are provided here to illustrate the effectiveness of the error correction method for EBP protection of a system during a GMD event. The example test system is depicted in Figure 8.5. CTs and PTs are located at the three-phase buses LEFT, RIGHT and LOAD, measuring the three-phase currents and voltages. The parameters of the instrumentation channels are shown in Table 8.1. The instrumentation cable is #10 copper cable with a length of 100 meters. The burden in CT channels is  $0.1\Omega$  and the burden in PT channels is  $10\text{ k}\Omega$ . To illustrate the effect of error correction on EBP protection, the protection zone including the transformer between busses RIGHT and

LOAD is examined. Several events of geomagnetic disturbance (GMD) and faults are considered. The response of the protection is computed with and without error correction of instrumentation channel errors.

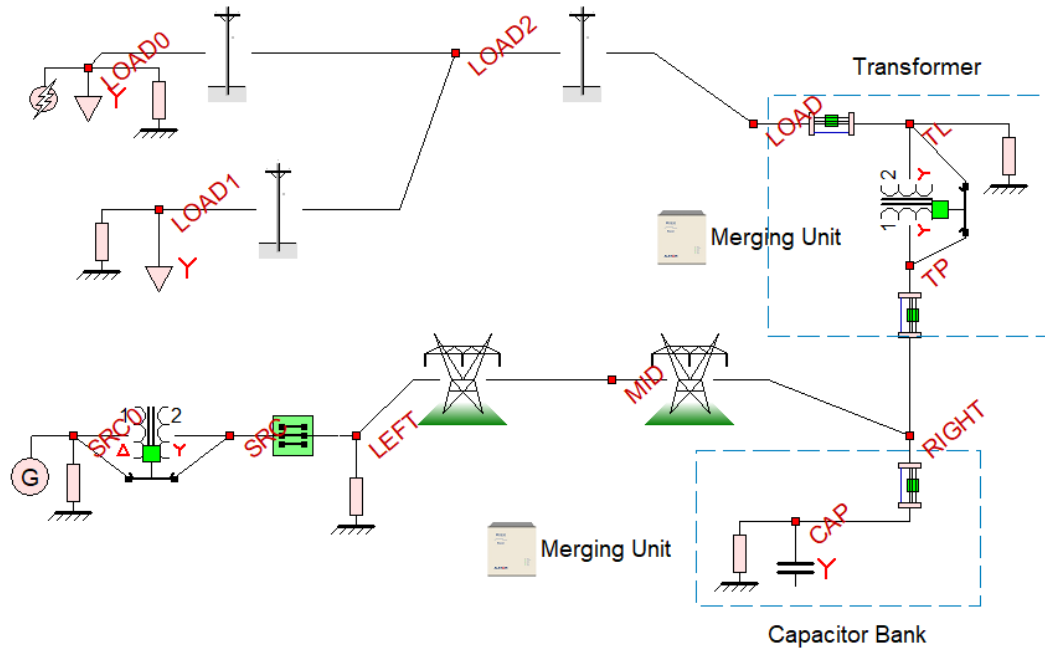


**Figure 8.5 Test System for EBP with Error Correction**

**Table 8.1 Instrumentation Channels Parameters**

Location	CT ratio	PT ratio
Bus RIGHT	2000:5	66,400:115
Bus LOAD	2000:5	14,400:115

The transformer protection zone contains the 115kV/25kV WYE-WYE connected transformer and adjacent breakers. For this protection zone, the following events are considered.

Event A-1: At time  $t=0s$ , the circuit breaker at bus SRC is closed, and the generator and step-up transformer are connected to the grid, which energizes the transmission lines and transformers. Before  $0s$ , there is no current flowing in the protection zones. This event focuses on the inrush current during transformer energization.

Event A-2: At time  $t=8s$ , a GMD event is introduced to the system. The magnitude of the earth's electric field is  $5V/km$  and the direction is aligned with the transmission line. The equivalent GMD DC voltage source locates between the groundings of transmission line from bus LEFT to bus RIGHT. The distance between the buses is  $20km$ , so a  $100V$  DC offset is introduced. The GMD event retreats at time  $t=18s$ .

Event A-3: At time  $t=16s$ , a Phase A to neutral fault occurs at bus MID. The fault resistance is  $0.1\Omega$  and this external fault exists until it is cleared at  $16.2s$ . After  $16.2s$ , the system is recovered, and phase A of the transformer is re-energized. This event focuses on this recovery process. During this event, the GMD event is still affecting the system.

In each event, three different EBP relays operate individually to monitor the protection zone. Three-phase voltage measurements and three-phase current measurements at bus RIGHT and bus LOAD are streamed to the relays.

1) The first EBP works with the direct measurements from the primary side, which is the exact value of the voltages and currents at buses. The behavior of this EBP relay is used as a reference.

2) The second EBP works with raw measurements from instrumentation channels, which are the measurements at burden multiplied by the instrumentation transformer ratios. These measurements are vulnerable to error introduced in instrumentation channels.

3) The third EBP works with corrected measurements, which is the result of the proposed state estimation based error correction method. Compared with raw measurements, the corrected measurements should be more consistent with the exact value on the primary side of the gird.

The three EBP modules use the same tripping decision function in equation (6), in which,  $t_{delay} = 10ms$  and  $t_{reset} = 300ms$ . In the following results, three EBP relays are compared in terms of their performance. Figure 8.6 to Figure 8.8 provide sample waveforms during these events. The first trace is the voltage of phase A to the ground at bus RIGHT. The second trace is the current of phase A on the same bus. The third and fourth traces are the voltage and current of Phase A at bus LOAD.

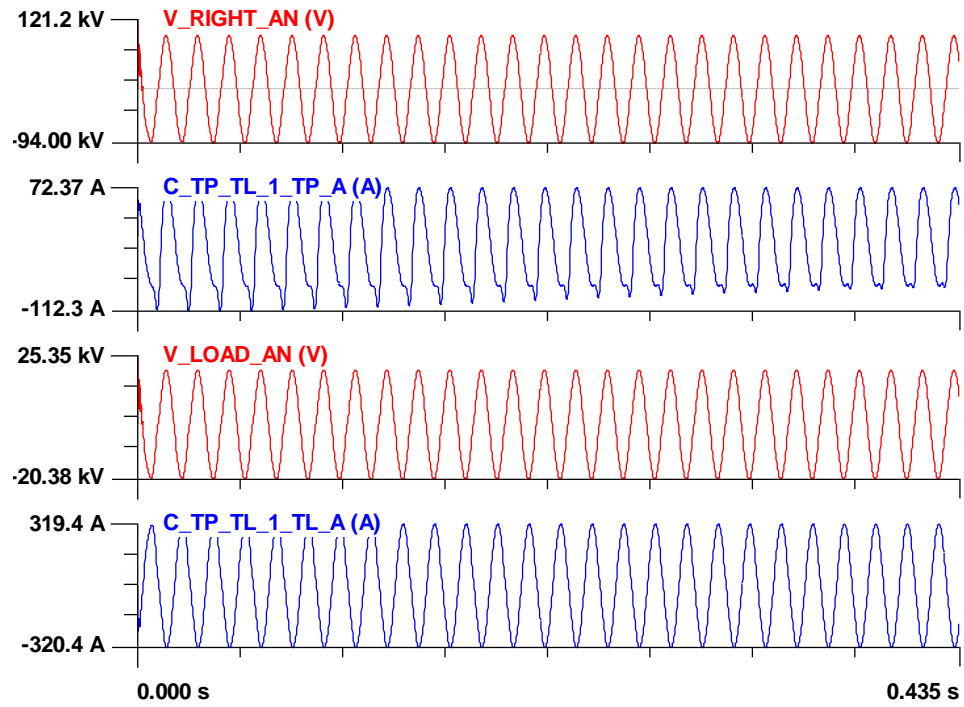


**Figure 8.6 Exact Measurements in Protection Zone 1: Event A-1**

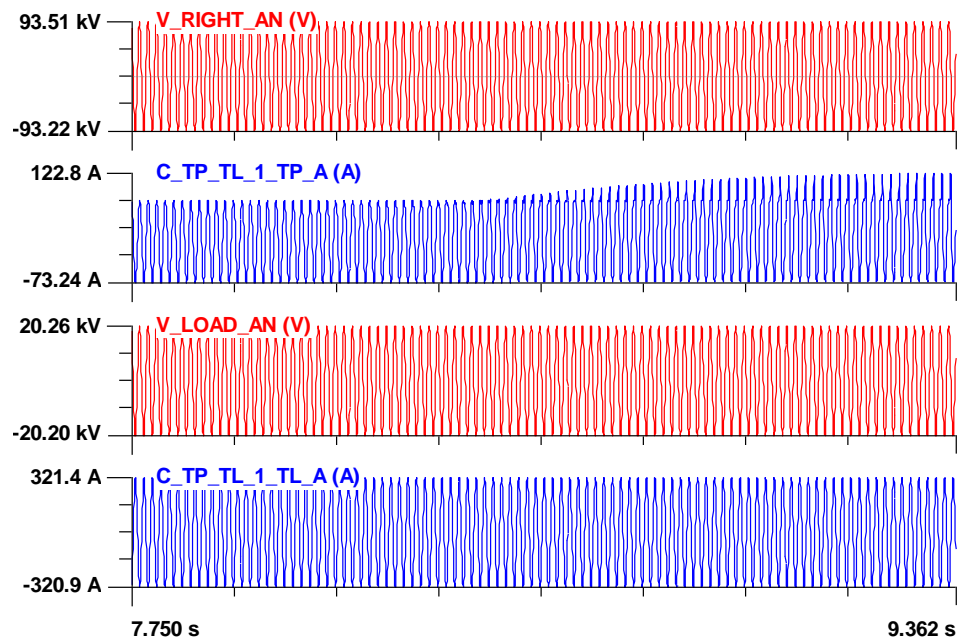


**Figure 8.7 Exact Measurements in Protection Zone 1: Event A-2**

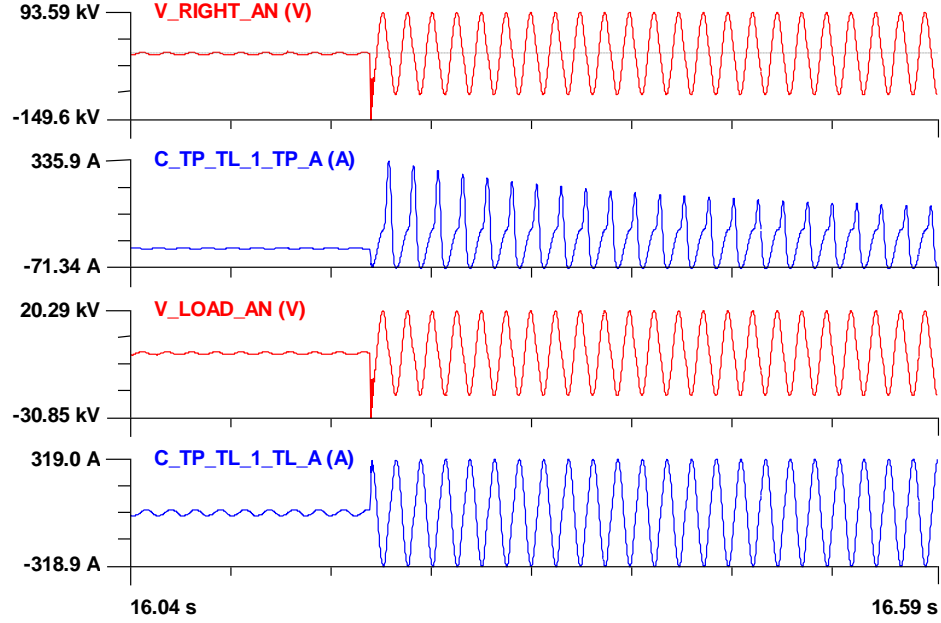


**Figure 8.8 Exact Measurements in Protection Zone 1: Event A-3**

- Event A-1: Energization of the transformer (0~0.4s)

At  $t=0$ s, the closer at bus SRC is closed, and the generator and step-up transformer are connected to the system. Due to the influence of the inrush current of the transformer in the protection zone, the EBP with simple measurements mis-operates during the beginning of the simulation. The status of EBP from 0 to 0.4s is shown in Figure 8.9. The increase of the chi-square value leads to a drop in confidence level. As a result, the EBP mistakenly detects an internal fault. In Figure 8.10 and Figure 8.11, the estimated current and voltages at bus RIGHT are compared with the primary value. Also, the measurements without correction are included in the comparison. It is apparent that the error introduced in the voltage channel leads to the mis-operation of EBP.

Meanwhile, the EBP with corrected measurements does not issue a trip decision as expected.

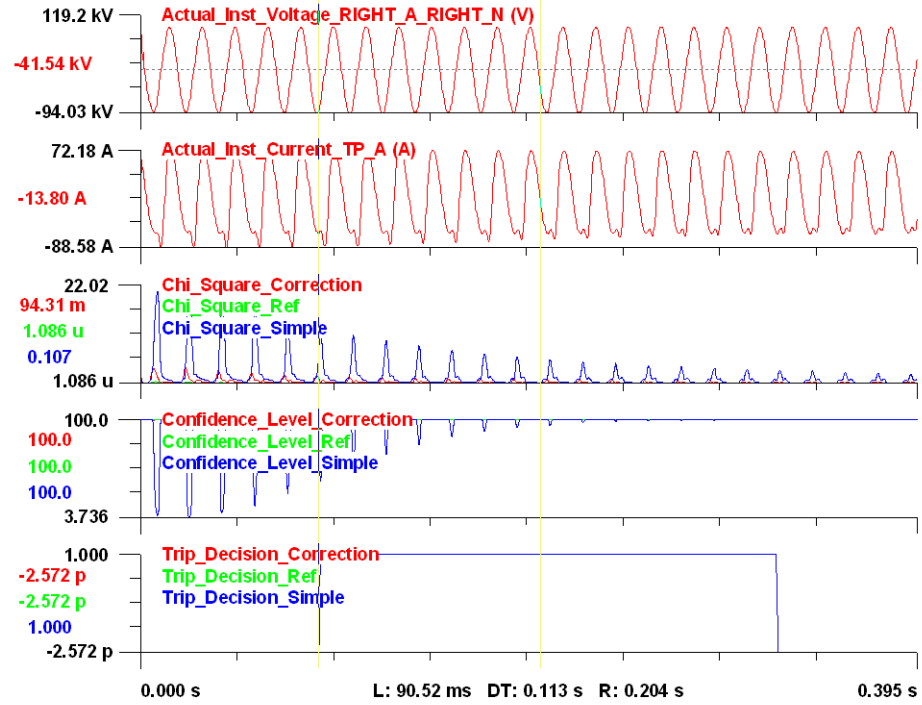


**Figure 8.9 Validation of Error Correction: EBP Results Comparison, Event A-1**

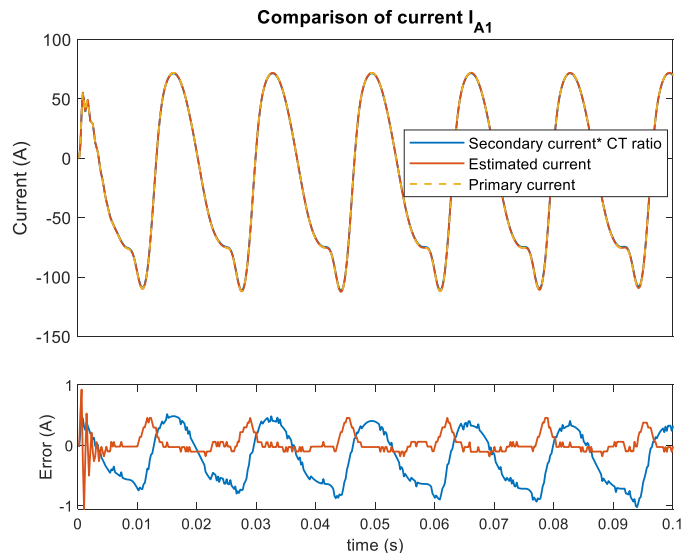


**Figure 8.10 Comparison of Currents in Event A-1**



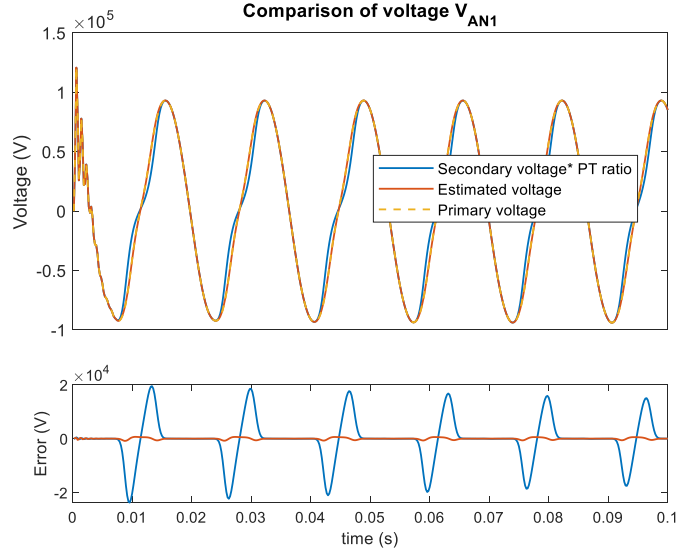


**Figure 8.11 Comparison of Voltages in Event A-1**

- Event A-2: Onset of GMD events (8s~10s)

To demonstrate the influence of GMD events on the instrumentation channel, a GMD event is introduced during the simulation. The GMD event starts at 8s and ends at time  $t=18s$ . The magnitude of the induced electric field is 5V/km, which is modeled as a DC voltage source between grounding at bus LEFT and RIGHT. During the beginning of the GMD events, the EBP with simple measurements generates a high chi-square and a low confidence level, which is shown in Figure 8.12. Though the drop in confidence level does not lead to a trip decision, this behavior decreases the reliability of EBP relay. In Figure 8.13 and Figure 8.14, the estimated current and voltages at bus RIGHT are compared with the primary value. In this case, the error in the voltage channel is the reason for the compromised performance.

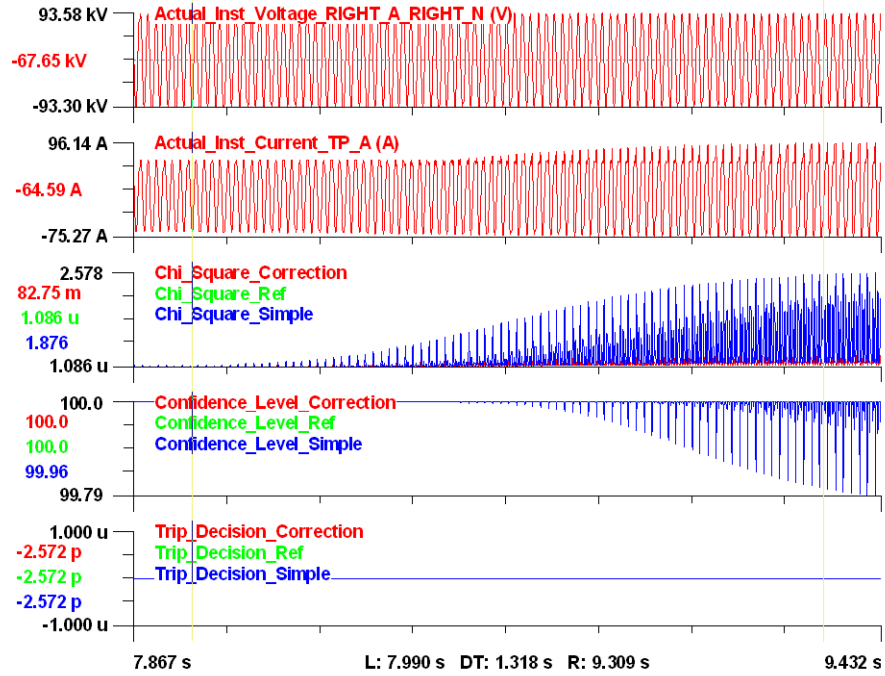


**Figure 8.12 Validation of Error Correction: EBP Results Comparison, Event A-2**

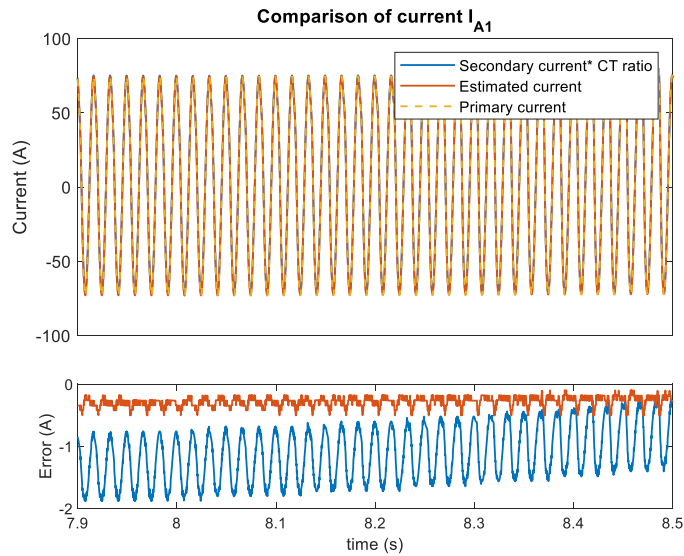


**Figure 8.13 Comparison of Currents in Event A-2**

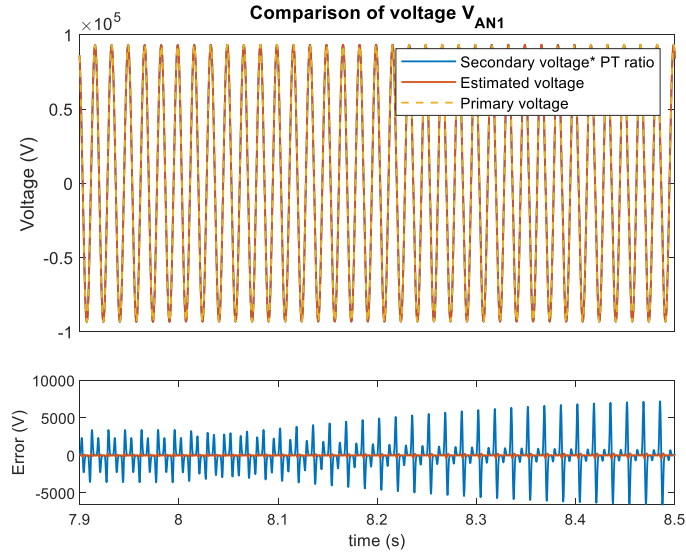


**Figure 8.14 Comparison of Voltages in Event A-2**

- Event A-3: Re-energization of the transformer after fault clearing (16.2s ~16.5s)

At 16s, an external fault at bus MID is introduced, and the fault is cleared at 16.2s. After the external fault was cleared, the EBP with simple measurements mis-operates, which is shown in Figure 8.15. This mis-operation is similar to the one occurs at the beginning of the simulation. In both cases, the transformer in protection is energized from offline. In Figure 8.16 and Figure 8.17, the estimated current and voltages at bus RIGHT are compared with the primary value. The distorted voltage measurements lead to the mis-operation of EBP.

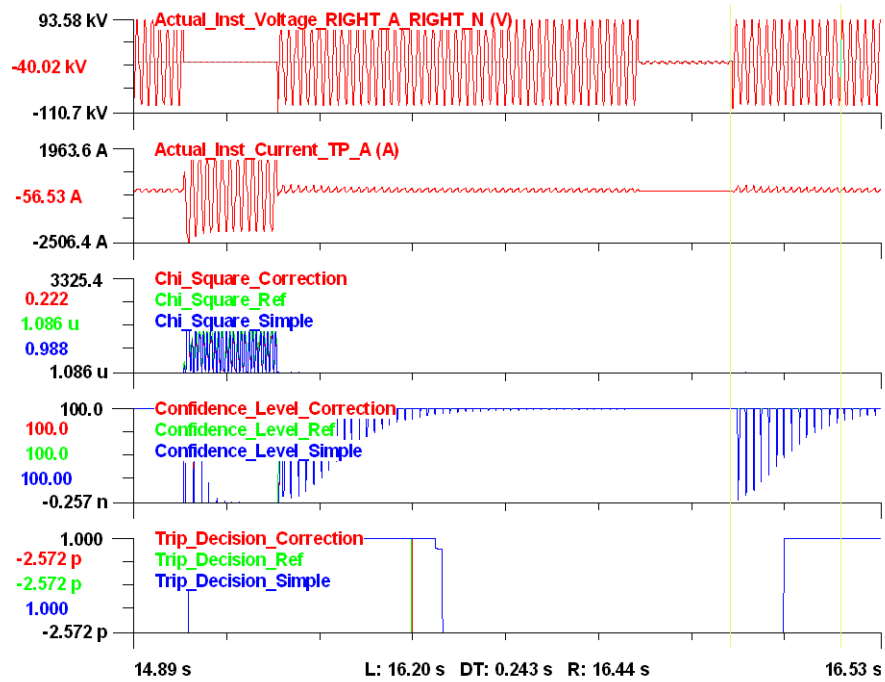


**Figure 8.15 Validation of Error Correction: EBP Results Comparison, Event A-3**

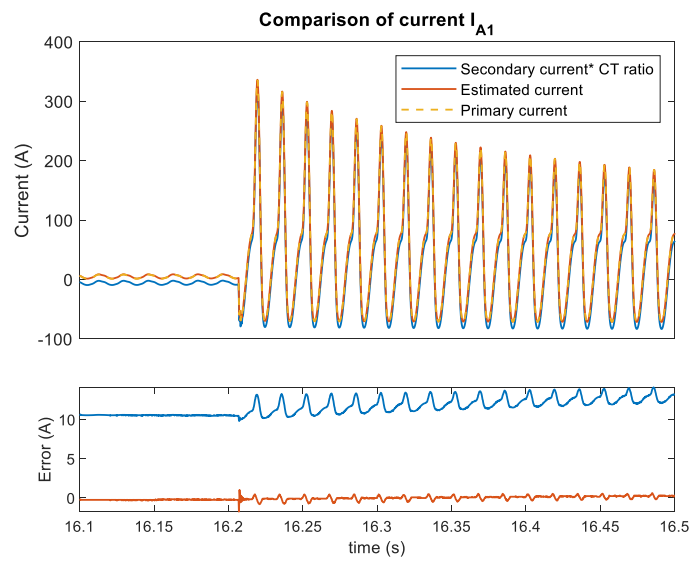


**Figure 8.16 Comparison of Currents in Event A-3**

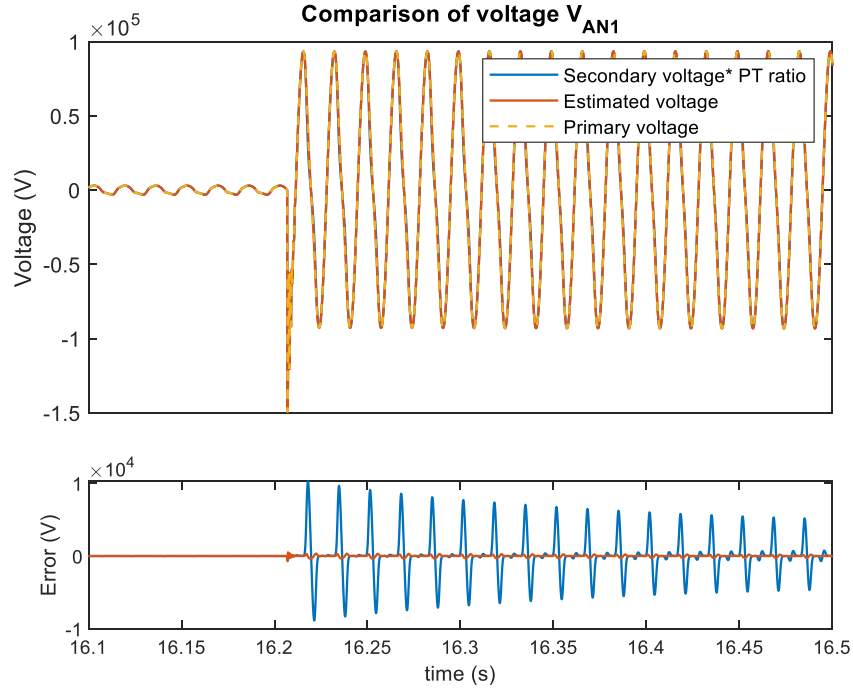


**Figure 8.17 Comparison of Voltages in Event A-3**

This section analyzes the instrumentation channel errors during GMD events and the performance of the relays considering these errors. We also present an instrumentation channel error correction method that works seamlessly with EBP. The dynamic state estimation based error correction procedure utilizes the physically-based model of and measurement data to estimate the states in the instrumentation channel, and the corrected primary quantities are available. The simulation tests show that the measurement error introduced in the current instrumentation channel and voltage instrumentation channel is eliminated. The corrected measurements facilitate the reliable operation of EBP and avoid the mis-operation of EBP during GMD events.

## 8.5 Comparison against Conventional Protection

After the performance of the error correction module is validated, the EBP approach for reliable protection during a GMD event is compared with conventional protection schemes in the numerical results provided in this section. The example test system is depicted in Figure 8.5. We focus on two protection zones: (a) The transformer between buses RIGHT and LOAD, and (b) the shunt capacitor bank connected to bus CAP. For this test system, the following events are considered. At time  $t=0s$ , the circuit breaker at bus SRC is closed, and the generator and step-up transformer are connected to the grid, which energizes the transmission lines and transformers. Before  $0s$ , there is no current flowing in the protection zones. This event focuses on the inrush current during the transformer energization. At time  $t=5s$ , a GMD event is introduced to the system. The magnitude of the geoelectric field is  $5V/km$  and the direction is aligned with the transmission line. The equivalent GMD DC voltage source locates between the groundings of the transmission line from bus LEFT to bus RIGHT. The distance between the buses is  $20km$ , so a  $100V$  DC offset is introduced. The GMD event retreats at  $10s$ .

The response of the protection schemes is computed with measurements processed by instrumentation channel error correction. In Figure 8.18, the instrumentation channel error correction result for PT channel at the transformer primary voltage  $V_{AN1}$  at bus TP is presented. The proposed error correction method is compared against the ratio-based method, and the accurate primary value is used as a reference. After the GMD starts at  $5s$ , the errors of results from the ratio-based method increase substantially. Meanwhile, the proposed state estimation based method still generates results with high accuracy. The relay performance for transformer protection and capacitor bank protection are presented as follows.

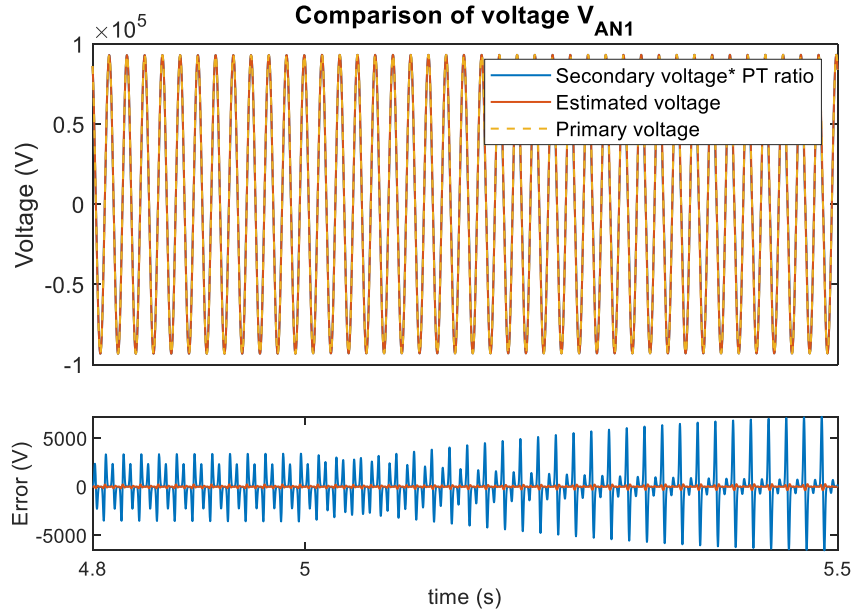


**Figure 8.18 PT Channel Error Correction Result**

### 8.5.1 Transformer Protection

Protection zone 1 contains the 115kV/25kV WYE-WYE connected transformer and adjacent breakers. 6 CTs and 6 PTs are installed to collect the three-phase currents and voltages at the transformer terminals. In the simulation experiment, the faults listed in Table 8.2 are introduced to the system (in addition to the GMD described earlier) to compare the performance of the proposed EBP and the conventional differential protection. The EBP operates on the transformer model with the DSE algorithm described in previous sections. The differential protection is equipped with 2<sup>nd</sup> order harmonic restraining to prevent mis-operation during transformer energization and GMD.

**Table 8.2 Test Faults for Transformer**

Fault Time	Fault Type
------------	------------

2.0~2.2s, 7.0~7.2s	Short Circuit Fault at LOAD0, Phase A to Neutral, $r_f = 0.01\Omega$
3.0~3.2s, 8.0~8.2s	Short Circuit Fault in Transformer Phase A 20% winding, $r_f = 10\Omega$
4.0~4.2s, 9.0~9.2s	Short Circuit Fault in Transformer Phase A 20% winding, $r_f = 100\Omega$

In Figure 8.19, the performance of the differential protection method is presented. When the ratio between operating current  $I_d$  and restraining current  $I_s$  exceeds 0.2 (20% restraint), the relay will issue a trip decision. If the 2<sup>nd</sup> order harmonic restraining module is not active, the transformer will be disconnected from the grid. At  $t=0s$ ,  $I_d$  increases due to the inrush current during transformer energization. The harmonic restraining module successfully blocks the trip; therefore, no mis-operation occurs. The relay also successfully handles the external fault at  $t=2s$  and the internal faults at  $t=3s$  and  $t=4s$ . However, during the GMD event, the operation of this relay is not consistent with the design. Due to the harmonics generated by the transformer half-cycle saturation, the restraining module is active throughout the GMD event. As a result, the internal faults at  $t=8s$  and  $t=9s$  are not detected. These mis-operations cannot be avoided by tuning the parameters in the relay. If the harmonic restraining module is set with a higher threshold, then the relay may mistakenly disconnect the transformer when the GMD event starts. To avoid this, the characteristic value  $I_d / I_{ST}$  is required to increase. However, the relay will lose the capability to detect larger impedance internal faults in the transformer, such as the one at  $t=4s$ .



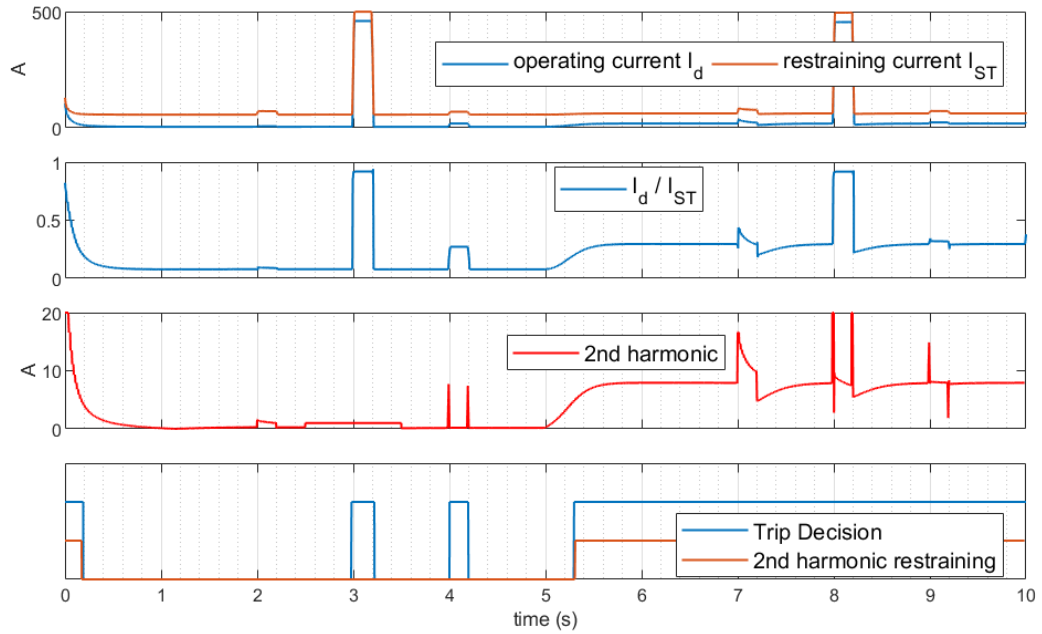


**Figure 8.19 Differential Protection Performance for the Transformer**

The performance of proposed dynamic state estimation based protection is shown in Figure 8.20. The figure depicts the phase A primary side current measurement  $I_A$ , the computed  $\chi^2$ , confidence level in percentage, and the trip decision. The EBP method successfully trips the internal faults and discriminates between internal faults and external faults, regardless of the presence of GMD. The transformer magnetic circuit model described in the previous section enables the DSE module to track the saturation of the transformer during GMD. Therefore, the  $\chi^2$  remains the same after GMD starts when there is no internal fault, indicating the consistency between measurements and the device model.

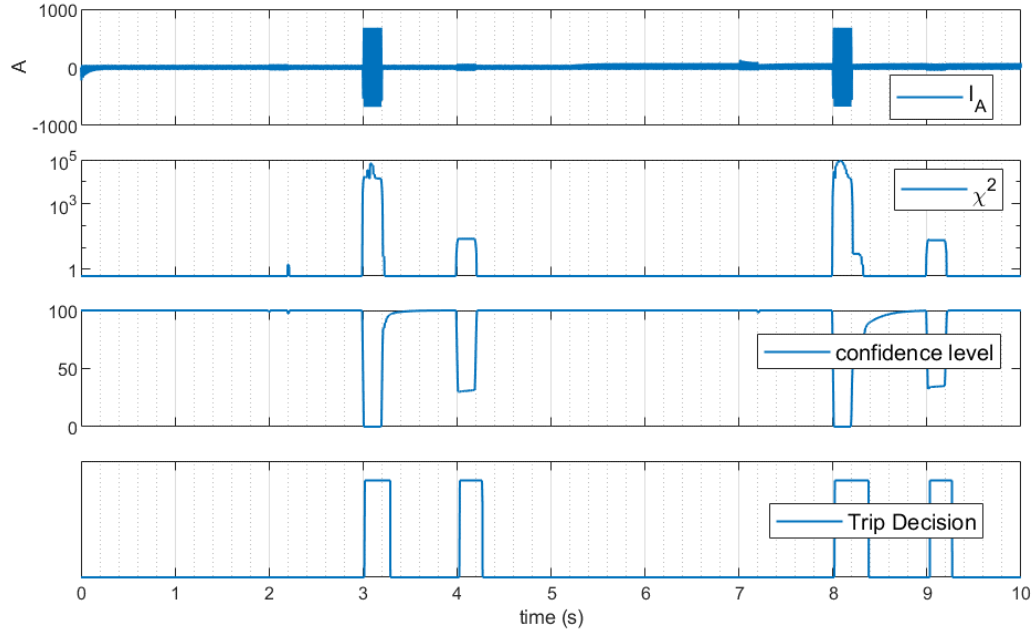


**Figure 8.20 EBP Performance for Transformer Protection**

### 8.5.2 Capacitor Bank Protection

Protection Zone 2 contains a 529 kVAr, WYE grounded capacitor bank and adjacent breakers. 3 CTs and 3 PTs are installed to collect three-phase currents and voltages at the capacitor bank terminals, and one CT is installed at neutral to measure the neutral current. The faults listed in Table 8.3 are introduced to the system (in addition to the GMD described earlier) to examine the performance of the proposed EBP and the neutral current differential protection. The relay should issue trip decisions during these internal faults.

**Table 8.3 Test Faults for Capacitor Bank**

Fault Time	Fault Type
3.0~3.2s,	Short Circuit Fault in the capacitor bank
8.0~8.2s	Phase A 20% capacitor blocks, $r_f = 0\Omega$

4.0~4.2s,	Short Circuit Fault in the capacitor bank
9.0~9.2s	Phase A 40% capacitor blocks, $r_f = 0\Omega$

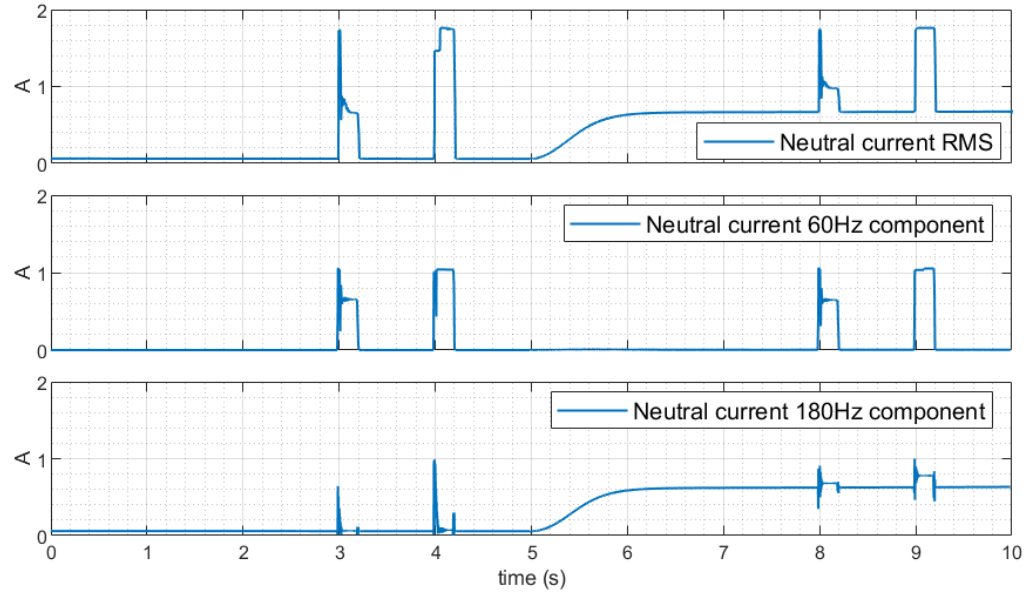


**Figure 8.21 Neutral Current Relay Performance for Capacitor Bank**

The performance of the neutral current protection method is presented in Figure 8.21. When the terminal voltage of the capacitor bank is balanced, the increase in the neutral current  $I_N$  indicates unbalanced currents in the capacitor branches. There are different criteria for a trip decision. The RMS value of  $I_N$ , for example, is a simple choice. However, the GMD event will generate 3<sup>rd</sup> order harmonic currents, which appear as the zero-sequence component flowing into the ground through the neutral. The neutral current will rise despite the status of the capacitor bank, leading to a mis-operation of the relay, which is shown in the first trace in Figure 8.21. Therefore, the base frequency component in neutral is a more reliable metric to monitor the capacitor bank during GMD. The relay should be tuned to be only sensitive to the 60 Hz component, as the

second trace shows. By contrast, the performance of EBP is not affected by GMD events, which is shown in Figure 8.22. It is apparent that the  $\chi^2$  value increases when the internal fault occurs and remains the same after the GMD starts. As a result, there is no mis-operation due to the onset of GMD, and the faults during GMD are successfully detected without extra tuning.

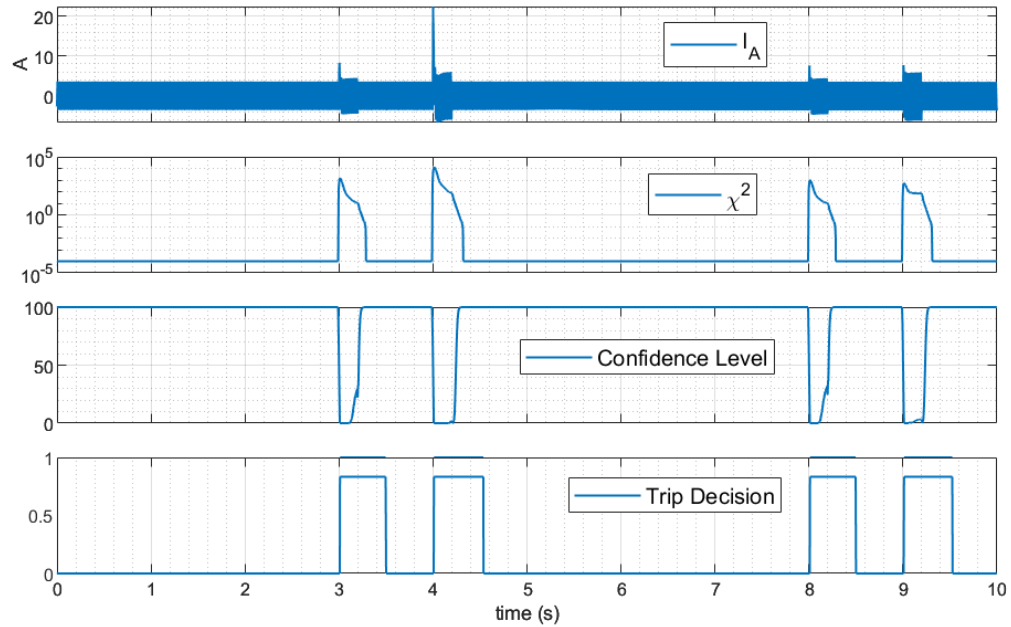


**Figure 8.22 EBP Performance for Capacitor Bank Protection**

## 8.6 Conclusions

This chapter analyzes the performance of the dynamic state estimation based protection relay during GMD events. We also present an instrumentation channel error correction method that works seamlessly with EBP. The simulation tests show that the measurement errors introduced in the current and voltage instrumentation channels are

eliminated. The corrected measurements facilitate the reliable operation of EBP and avoid the mis-operation of EBP during GMD events. Several conventional relays are examined during GMD activities. Mis-operations are observed in differential protection for transformers and in neutral current protection for capacitor banks. Compared with conventional relays, EBP remains reliable without extra tuning during GMD events.

## **CHAPTER 9. CONCLUSIONS AND FUTURE WORK**

### **9.1 Conclusions**

The contributions of this dissertation are as follows: 1) a time domain simulation method for high fidelity GIC analysis; 2) a set of time domain device models with accurate frequency characteristics over the frequency range of harmonics created by GIC; a low frequency (0.0001Hz to 1200Hz) broadband transmission line model has been developed and validated; two-winding/three-winding transformer models with detailed magnetic circuit has been developed and validated; 3) GIC transient analysis for large scale systems; 4) accurate harmonics analysis of power systems during GMD events; 5) protective relay performance analysis during GMD events, and 6) incorporation of instrumentation channels error correction into protective relaying systems.

The frequency characteristics of the low-frequency broadband transmission line are compared with the analytical solution and good consistency is observed within the frequency range related to GIC. Transformer models with different configurations are compared in time domain simulation. The results show that there exists a large difference between these transformers during GMD events. A mitigation method to reduce saturation and harmonics is proposed and its effectiveness was quantified.

The proposed time domain simulation method has been tested with a large scale test case and the dynamics of GIC are studied at different locations, revealing the transients which are not available in the conventional simplified DC analysis approach. The resulting dynamics of GIC are drastically different at different locations. In addition,

the results present short-term peaks of GIC, indicating the steady state value of GIC is not a complete indicator of the impact of GIC.

The performance of protective relays during GIC events has been examined and the effect of instrumentation channel error is studied. A state estimation based protection (EBP) with instrumentation channel error correction is developed. Results show that the error correction module substantially increases the reliability of EBP. Several conventional protection schemes are also implemented for comparison purposes. The comparative results display the advantage of the EBP scheme during GMD. The performance of EBP is not affected by the harmonics and DC component generated by GIC, while conventional protection schemes could produce mis-operation.

## **9.2 Future Work**

This dissertation focuses on the analysis of GIC in time domain, and it can be extended to the following related problems.

- 1) The response of the system to GMD over a longer period, such as hours even days. Realistic GMD measurements can be applied to the system and analysis could follow a similar process presented in previous chapters.
- 2) The response of power electronics devices to GIC, such as FACTS. On one hand, the power electronics devices generate high-order harmonics due to high frequency switching on/off, which may complicate the harmonics during GIC [78], [79]. On the other hand, the DC components and low order harmonics generate by GMD may threaten the operation of power electronic devices, including the valves, the control circuits and most importantly the

protection system. The analysis of this problem is quite complex and it will require a substantial research effort to investigate[80]. We believe that EBP relays could provide a robust solution.

- 3) In the modern power grid, the existence of distributed energy resources such as solar panels and batteries is common. The interaction of these devices with GIC is of great interest and concern. An investigation of the issues associated with the distribution system with high penetration of DERs [81]–[86] is a natural extension of the work in this thesis.



## REFERENCES

- [1] J. G. Kappenman and V. D. Albertson, "Bracing for the geomagnetic storms," *IEEE Spectr.*, vol. 27, no. 3, pp. 27–33, 1990.
- [2] L. Bolduc, "GIC observations and studies in the Hydro-Québec power system," *J. Atmospheric Sol.-Terr. Phys.*, vol. 64, no. 16, pp. 1793–1802, 2002.
- [3] A. Pulkkinen *et al.*, "Geomagnetically induced currents: Science, engineering, and applications readiness," *Space Weather*, vol. 15, no. 7, pp. 828–856, Jul. 2017, doi: 10.1002/2016SW001501.
- [4] T. S. Molinski, W. E. Feero, and B. L. Damsky, "Shielding grids from solar storms [power system protection]," *Ieee Spectr.*, vol. 37, no. 11, pp. 55–60, 2000.
- [5] A. Pulkkinen, S. Lindahl, A. Viljanen, and R. Pirjola, "Geomagnetic storm of 29-31 October 2003: Geomagnetically induced currents and their relation to problems in the Swedish high-voltage power transmission system," *Space Weather*, vol. 3, no. 8, Aug. 2005, doi: 10.1029/2004SW000123.
- [6] L. Trichtchenko and D. H. Boteler, "Response of power systems to the temporal characteristics of geomagnetic storms," in *Electrical and Computer Engineering, 2006. CCECE'06. Canadian Conference on*, 2006, pp. 390–393.
- [7] V. D. Albertson, J. M. Thorson, R. E. Clayton, and S. C. Tripathy, "Solar-induced-currents in power systems: Cause and effects," *IEEE Trans. Power Appar. Syst.*, no. 2, pp. 471–477, 1973.
- [8] R. J. Pirjola and A. T. Viljanen, "Geomagnetic Induction in the Finnish 400 KV Power System," in *Environmental and Space Electromagnetics*, H. Kikuchi, Ed. Tokyo: Springer Japan, 1991, pp. 276–287.
- [9] K. F. Forbes and O. C. St. Cyr, "Space weather and the electricity market: An initial assessment," *Space Weather*, vol. 2, no. 10, Oct. 2004, doi: 10.1029/2003SW000005.
- [10] T. S. Molinski, "Why utilities respect geomagnetically induced currents," *Space Weather Eff. Technol. Syst.*, vol. 64, no. 16, pp. 1765–1778, 2002, doi: 10.1016/S1364-6826(02)00126-8.
- [11] J. G. Kappenman, "An overview of the impulsive geomagnetic field disturbances and power grid impacts associated with the violent Sun-Earth connection events of 29-31 October 2003 and a comparative evaluation with other contemporary storms," *Space Weather*, vol. 3, no. 8, Aug. 2005, doi: 10.1029/2004SW000128.

- [12] “Application Guide for Computing GIC in the Bulk Power System,” North American Electric Reliability Corporation (NERC), Dec. 2013.
- [13] D. H. Boteler, R. J. Pirjola, and H. Nevanlinna, “The effects of geomagnetic disturbances on electrical systems at the Earth’s surface,” *Adv. Space Res.*, vol. 22, no. 1, pp. 17–27, 1998.
- [14] J. Kappenman, *Geomagnetic storms and their impacts on the US power grid*. Metatech, 2010.
- [15] X. Dong, Y. Liu, and J. G. Kappenman, “Comparative analysis of exciting current harmonics and reactive power consumption from GIC saturated transformers,” in *Power Engineering Society Winter Meeting, 2001. IEEE*, 2001, vol. 1, pp. 318–322.
- [16] M. Lahtinen and J. Elovaara, “GIC occurrences and GIC test for 400 kV system transformer,” *IEEE Trans. Power Deliv.*, vol. 17, no. 2, pp. 555–561, 2002.
- [17] S. Lu, Y. Liu, and J. De La Ree, “Harmonics generated from a DC biased transformer,” *IEEE Trans. Power Deliv.*, vol. 8, no. 2, pp. 725–731, 1993.
- [18] A. Morched, B. Gustavsen, and M. Tartibi, “A universal model for accurate calculation of electromagnetic transients on overhead lines and underground cables,” *IEEE Trans. Power Deliv.*, vol. 14, no. 3, pp. 1032–1038, 1999.
- [19] A. Budner, “Introduction of frequency-dependent line parameters into an electromagnetic transients program,” *IEEE Trans. Power Appar. Syst.*, no. 1, pp. 88–97, 1970.
- [20] G. J. Cokkinides and A. S. Meliopoulos, “Transmission line modeling with explicit grounding representation,” *Electr. Power Syst. Res.*, vol. 14, no. 2, pp. 109–119, 1988.
- [21] C.-S. Yen, Z. Fazarinc, and R. L. Wheeler, “Time-domain skin-effect model for transient analysis of lossy transmission lines,” *Proc. IEEE*, vol. 70, no. 7, pp. 750–757, 1982.
- [22] S. Kim and D. P. Neikirk, “Compact equivalent circuit model for the skin effect,” in *Microwave Symposium Digest, 1996., IEEE MTT-S International*, 1996, vol. 3, pp. 1815–1818.
- [23] B. K. Sen and R. L. Wheeler, “Skin effects models for transmission line structures using generic SPICE circuit simulators,” in *Electrical Performance of Electronic Packaging, 1998. IEEE 7th Topical Meeting on*, 1998, pp. 128–131.
- [24] J. Acero and C. R. Sullivan, “A dynamic equivalent network model of the skin effect,” in *Applied Power Electronics Conference and Exposition (APEC), 2013 Twenty-Eighth Annual IEEE*, 2013, pp. 2392–2397.

- [25] P. Holmberg, M. Leijon, and T. Wass, "A wideband lumped circuit model of eddy current losses in a coil with a coaxial insulation system and a stranded conductor," *IEEE Trans. Power Deliv.*, vol. 18, no. 1, pp. 50–60, Jan. 2003, doi: 10.1109/TPWRD.2002.803753.
- [26] W. T. Weeks, L.-H. Wu, M. F. McAllister, and A. Singh, "Resistive and inductive skin effect in rectangular conductors," *IBM J. Res. Dev.*, vol. 23, no. 6, pp. 652–660, 1979.
- [27] Shizhong Mei and Y. I. Ismail, "Modeling skin and proximity effects with reduced realizable RL circuits," *IEEE Trans. Very Large Scale Integr. VLSI Syst.*, vol. 12, no. 4, pp. 437–447, Apr. 2004, doi: 10.1109/TVLSI.2004.825863.
- [28] J. H. Krah, "Optimum discretization of a physical Cauer circuit," *IEEE Trans. Magn.*, vol. 41, no. 5, pp. 1444–1447, May 2005, doi: 10.1109/TMAG.2005.844548.
- [29] M. Sarto, A. Scarlatti, and C. Holloway, "On the use of fitting models for the time-domain analysis of problems with frequency-dependent parameters," in *Electromagnetic Compatibility, 2001. EMC. 2001 IEEE International Symposium on*, 2001, vol. 1, pp. 588–593.
- [30] S. Jazebi, F. de Leon, and B. Vahidi, "Duality-Synthesized Circuit for Eddy Current Effects in Transformer Windings," *IEEE Trans. Power Deliv.*, vol. 28, no. 2, pp. 1063–1072, Apr. 2013, doi: 10.1109/TPWRD.2013.2238257.
- [31] A. Semlyen and A. Deri, "Time domain modeling of frequency dependent three-phase transmission line impedance," *IEEE Power Eng. Rev.*, no. 6, pp. 64–65, 1985.
- [32] A. Viljanen and R. Pirjola, "Geomagnetically induced currents in the Finnish high-voltage power system," *Surv. Geophys.*, vol. 15, no. 4, pp. 383–408, 1994.
- [33] A. Rezaei-Zare, "Reactive Power Loss Versus GIC Characteristic of Single-Phase Transformers," *IEEE Trans. Power Deliv.*, vol. 30, no. 3, pp. 1639–1640, Jun. 2015, doi: 10.1109/TPWRD.2015.2394311.
- [34] R. A. Walling and A. N. Khan, "Characteristics of transformer exciting-current during geomagnetic disturbances," *IEEE Trans. Power Deliv.*, vol. 6, no. 4, pp. 1707–1714, 1991.
- [35] P. Picher, L. Bolduc, A. Dutil, and V. Q. Pham, "Study of the acceptable DC current limit in core-form power transformers," *IEEE Trans. Power Deliv.*, vol. 12, no. 1, pp. 257–265, 1997.
- [36] L. Marti, A. Rezaei-Zare, and A. Narang, "Simulation of Transformer Hotspot Heating due to Geomagnetically Induced Currents," *IEEE Trans. Power Deliv.*, vol. 28, no. 1, pp. 320–327, Jan. 2013, doi: 10.1109/TPWRD.2012.2224674.

- [37] R. Girgis and K. Vedante, “Effects of GIC on power transformers and power systems,” in *Transmission and Distribution Conference and Exposition (T&D), 2012 IEEE PES*, 2012, pp. 1–8.
- [38] C. T. Gaunt and G. Coetzee, “Transformer failures in regions incorrectly considered to have low GIC-risk,” in *Power Tech, 2007 IEEE Lausanne*, 2007, pp. 807–812.
- [39] J. G. Kappenman, “Geomagnetic storms and their impact on power systems,” *IEEE Power Eng. Rev.*, vol. 16, no. 5, p. 5, 1996.
- [40] I. P. Zois, “Solar activity and transformer failures in the Greek national electric grid,” *J. Space Weather Space Clim.*, vol. 3, p. A32, 2013, doi: 10.1051/swsc/2013055.
- [41] J. Ramírez-Niño, C. Haro-Hernández, J. H. Rodríguez-Rodríguez, and R. Mijarez, “Core saturation effects of geomagnetic induced currents in power transformers,” *J. Appl. Res. Technol.*, vol. 14, no. 2, pp. 87–92, Apr. 2016, doi: 10.1016/j.jart.2016.04.003.
- [42] N. Takasu, T. Oshi, F. Miyawaki, S. Saito, and Y. Fujiwara, “An experimental analysis of DC excitation of transformers by geomagnetically induced currents,” *IEEE Trans. Power Deliv.*, vol. 9, no. 2, pp. 1173–1182, 1994.
- [43] T. Ngnegueu *et al.*, “Behavior of transformers under DC/GIC excitation: Phenomenon, Impact on design/design evaluation process and modelling aspects in support of design,” *Proc. CIGRE*, 2012.
- [44] S. Lu and Y. Liu, “FEM analysis of DC saturation to assess transformer susceptibility to geomagnetically induced currents,” *IEEE Trans. Power Deliv.*, vol. 8, no. 3, pp. 1367–1376, 1993.
- [45] N. Chieas, A. Lotfi, H. Høidalen, B. Mork, Ø. Rui, and T. Ohnstad, “Five-leg transformer model for GIC studies,” in *International Conference on Power Systems Transients (IPST2013) in Vancouver, Canada*, 2013.
- [46] J. G. Kappenman, V. D. Albertson, and N. Mohan, “Current transformer and relay performance in the presence of geomagnetically-induced currents,” *IEEE Trans. Power Appar. Syst.*, no. 3, pp. 1078–1088, 1981.
- [47] B. Kasztenny, N. Fischer, D. Taylor, T. Prakash, and J. Jalli, “Do CTs like DC? Performance of current transformers with geomagnetically induced currents,” in *2016 69th Annual Conference for Protective Relay Engineers (CPRE)*, Apr. 2016, pp. 1–17, doi: 10.1109/CPRE.2016.7914885.
- [48] B. Bozoki *et al.*, “The effects of GIC on protective relaying,” *IEEE Trans. Power Deliv.*, vol. 11, no. 2, pp. 725–739, 1996.

- [49] D. H. Boteler and R. J. Pirjola, "Modelling geomagnetically induced currents produced by realistic and uniform electric fields," *IEEE Trans. Power Deliv.*, vol. 13, no. 4, pp. 1303–1308, 1998.
- [50] T. J. Overbye, T. R. Hutchins, K. Shetye, J. Weber, and S. Dahman, "Integration of geomagnetic disturbance modeling into the power flow: A methodology for large-scale system studies," in *North American Power Symposium (NAPS), 2012*, 2012, pp. 1–7.
- [51] D. H. Boteler and R. J. Pirjola, "Modeling geomagnetically induced currents," *Space Weather*, vol. 15, no. 1, pp. 258–276, Jan. 2017, doi: 10.1002/2016SW001499.
- [52] M. D. Butala *et al.*, "Modeling Geomagnetically Induced Currents From Magnetometer Measurements: Spatial Scale Assessed With Reference Measurements," *Space Weather*, vol. 15, no. 10, pp. 1357–1372, Oct. 2017, doi: 10.1002/2017SW001602.
- [53] K. Zheng *et al.*, "Effects of System Characteristics on Geomagnetically Induced Currents," *IEEE Trans. Power Deliv.*, vol. 29, no. 2, pp. 890–898, Apr. 2014, doi: 10.1109/TPWRD.2013.2281191.
- [54] A. Pulkkinen, E. Bernabeu, J. Eichner, C. Beggan, and A. W. P. Thomson, "Generation of 100-year geomagnetically induced current scenarios," *Space Weather*, vol. 10, no. 4, Apr. 2012, doi: 10.1029/2011SW000750.
- [55] A. S. Meliopoulos, *Power system grounding and transients: an introduction*, vol. 50. CRC Press, 1988.
- [56] J. R. Carson, "Wave propagation in overhead wires with ground return," *Bell Syst. Tech. J.*, vol. 5, no. 4, pp. 539–554, 1926, doi: 10.1002/j.1538-7305.1926.tb00122.x.
- [57] Y. Liu, A. P. Sakis Meliopoulos, Z. Tan, L. Sun, and R. Fan, "Dynamic state estimation-based fault locating on transmission lines," *IET Gener. Transm. Distrib.*, vol. 11, no. 17, pp. 4184–4192, Nov. 2017, doi: 10.1049/iet-gtd.2017.0371.
- [58] J. Xie, A. S. Meliopoulos, and B. Xie, "Transmission Line Fault Classification Based on Dynamic State Estimation and Support Vector Machine," in *2018 North American Power Symposium (NAPS)*, 2018, pp. 1–5.
- [59] Y. Liu, Z. Tan, and J. Xie, "Phasor domain transmission line fault locating with three phase distributed parameter modeling," presented at the 2018 IEEE Power & Energy Society General Meeting (PESGM), 2018, pp. 1–5.
- [60] J. Xie, A.P. Meliopoulos, and Y. Liu, "Low Broadband Transmission Line Model for Geomagnetically Induced Current Analysis," in *2018 IEEE Power & Energy Society General Meeting*, 2018.

- [61] H.-C. Tay and G. W. Swift, "On the problem of transformer overheating due to geomagnetically induced currents," *IEEE Trans. Power Appar. Syst.*, no. 1, pp. 212–219, 1985.
- [62] G. K. Stefopoulos, G. J. Cokkinides, and A. S. Meliopoulos, "Quadratized model of nonlinear saturable-core inductor for time-domain simulation," in *Power & Energy Society General Meeting, 2009. PES'09. IEEE*, 2009, pp. 1–8.
- [63] J. Xie, A. P. Meliopoulos, Xie, Boqi, C. Zhong, and K. Liu, "Goelectric Field Estimation during Geomagnetic Disturbances," in *2019 IEEE Power & Energy Society General Meeting*, 2019.
- [64] A. P. S. Meliopoulos, G. J. Cokkinides, Z. Tan, S. Choi, Y. Lee, and P. Myrda, "Setting-Less Protection: Feasibility Study," in *2013 46th Hawaii International Conference on System Sciences*, Jan. 2013, pp. 2345–2353, doi: 10.1109/HICSS.2013.628.
- [65] A. P. S. Meliopoulos *et al.*, "Dynamic State Estimation-Based Protection: Status and Promise," *IEEE Trans. Power Deliv.*, vol. 32, no.1, pp. 320–330, Feb. 2017, doi: 10.1109/TPWRD.2016.2613411.
- [66] B. Xie, A. P. S. Meliopoulos, Y. Liu, and L. Sun, "Distributed quasi-dynamic state estimation with both GPS-synchronized and non-synchronized data," in *2017 North American Power Symposium (NAPS)*, Morgantown, WV, Sep. 2017, pp. 1–6, doi: 10.1109/NAPS.2017.8107173.
- [67] S. Meliopoulos, J. Xie, and G. Cokkinides, "Power system harmonic analysis under geomagnetic disturbances," in *2018 18th International Conference on Harmonics and Quality of Power (ICHQP)*, May 2018, pp. 1–6, doi: 10.1109/ICHQP.2018.8378913.
- [68] A. P. S. Meliopoulos, J. Xie, and G. Cokkinides, "Power system harmonic analysis under geomagnetic disturbances," in *2018 18th International Conference on Harmonics and Quality of Power (ICHQP)*, 2018.
- [69] Xie, Boqi *et al.*, "Dynamic State Estimation Based Unit Protection," in *2019 IEEE Power & Energy Society General Meeting*, 2019.
- [70] A. P. S. Meliopoulos, G. Cokkinides, J. Xie, and Y. Kong, "Instrumentation Error Correction within Merging Units," in *Proceedings of the 2018 Georgia Tech Fault and Disturbance Analysis Conference*, Apr. 2018.
- [71] B. Xie *et al.*, "A Performance Comparison Study of Quasi-Dynamic State Estimation and Static State Estimation," in *2020 IEEE Power & Energy Society General Meeting (PESGM)*, Montreal, 2020, pp. 1–5.
- [72] C. Zhong, A. S. Meliopoulos, B. Xie, J. Xie, K. Liu, and H. Shao, "Detailed Multiphysics Modeling of Air-Conditioned House," presented at the 2019 IEEE

- Power & Energy Society Innovative Smart Grid Technologies Conference (ISGT), 2019, pp. 1–5.
- [73] C. Zhong, A. P. S. Meliopoulos, J. Xie, Al Owaifeer, Maad M, and Ilunga, Gad Monga, “Object-oriented security constrained quadratic optimal power flow,” in *2020 IEEE Power & Energy Society General Meeting (PESGM)*, Montreal, 2020, pp. 1–5.
  - [74] G. K. Stefopoulos, G. J. Cokkinides, and A. P. Meliopoulos, “Quadratic integration method for transient simulation and harmonic analysis,” in *Harmonics and Quality of Power, 2008. ICHQP 2008. 13th International Conference on*, 2008, pp. 1–6.
  - [75] J. Xie and A. P. S. Meliopoulos, “Sensitive Detection of GPS Spoofing Attack in Phasor Measurement Units via Quasi-Dynamic State Estimation,” *Computer*, vol. 53, no. 5, 2020, doi: 10.1109/MC.2020.2976943.
  - [76] J. Pan, K. Vu, and Y. Hu, “An Efficient Compensation Algorithm for Current Transformer Saturation Effects,” *IEEE Trans. Power Deliv.*, vol. 19, no. 4, pp. 1623–1628, Oct. 2004, doi: 10.1109/TPWRD.2004.835273.
  - [77] J. Xie, A. P. S. Meliopoulos, B. Xie, C. Zhong, and K. Liu, “A Reliable Dynamic State Estimation Based Protection during Geomagnetic Disturbances,” in *2020 IEEE Power & Energy Society General Meeting (PESGM)*, Montreal, 2020, pp. 1–5.
  - [78] C. Zhong and J. L. Mathieu, “Relation between overheating of distribution transformers and switching frequency of electric loads used for demand response,” in *2015 North American Power Symposium (NAPS)*, 2015, pp. 1–6.
  - [79] K. Liu, A. S. Meliopoulos, B. Xie, C. Zhong, and J. Xie, “Quasi-dynamic domain modeling of line-commutated converters with the analytical approach,” in *2019 North American Power Symposium (NAPS)*, 2019, pp. 1–6.
  - [80] C. Zhong, A. S. Meliopoulos, J. Sun, M. Saeedifard, and B. Xie, “Modeling of converter losses with high fidelity in a physically based object-oriented way,” presented at the 2018 IEEE Power & Energy Society General Meeting (PESGM), 2018, pp. 1–5.
  - [81] C. Zhong, J. Sun, J. Xie, S. Grijalva, and A. S. Meliopoulos, “Real-time human activity-based energy management system using model predictive control,” presented at the 2018 IEEE International Conference on Consumer Electronics (ICCE), 2018, pp. 1–6.
  - [82] C. Zhong, A. P. S. Meliopoulos, G. J. Cokkinides, and B. Xie, “Object-Oriented Voltage Control for AC-DC Hybrid Distribution Systems,” in *2018 9th IEEE International Symposium on Power Electronics for Distributed Generation Systems (PEDG)*, 2018, pp. 1–4.

- [83] B. Xie, A. P. S. Meliopoulos, C. Zhong, Y. Liu, L. Sun, and J. Xie, “Distributed Quasi-Dynamic State Estimation Incorporating Distributed Energy Resources,” in *2018 North American Power Symposium (NAPS)*, Fargo, ND, Sep. 2018, pp. 1–6, doi: 10.1109/NAPS.2018.8600662.
- [84] S. Meliopoulos *et al.*, “Autonomous multi-stage flexible OPF for active distribution systems with DERs,” presented at the Proceedings of the 52nd Hawaii International Conference on System Sciences, 2019.
- [85] C. Zhong, B. Xie, and A. P. S. Meliopoulos, “Distribution Network Voltage Profile Optimization via Multi-Stage Flexible Optimal Power Flow,” in *2019 North American Power Symposium (NAPS)*, 2019, pp. 1–6.
- [86] K. Liu, A. P. S. Meliopoulos, B. Xie, C. Zhong, and J. Xie, “Dynamic State Estimation-Based Protection of Distribution Systems with High Penetration of DERs,” in *2020 IEEE Power & Energy Society General Meeting (PESGM)*, Montreal, 2020, pp. 1–5.



## **VITA**

Jiahao Xie received his Bachelor's degree in Electrical Engineering from Southeast University, China, in 2015. He received a Master's degree in Electrical and Computer Engineering at Georgia Institute of Technology in 2016. He became a Ph.D. candidate at Georgia Institute of Technology in 2017. His main areas of research interest are geomagnetically induced current and dynamic state estimation.